ADJOINT-BASED DESIGN OPTIMIZATION OF A HYPERSONIC INLET

A THESIS SUBMITTED TO
THE GRADUATE SCHOOL OF NATURAL AND APPLIED SCIENCES
OF
MIDDLE EAST TECHNICAL UNIVERSITY

BY

MEHMET BAŞARAN

IN PARTIAL FULFILLMENT OF THE REQUIREMENTS
FOR
THE DEGREE OF MASTER OF SCIENCE
IN
AEROSPACE ENGINEERING

SEPTEMBER 2019

Approval of the thesis:

ADJOINT-BASED DESIGN OPTIMIZATION OF A HYPERSONIC INLET

submitted by **MEHMET BAŞARAN** in partial fulfillment of the requirements for the degree of **Master of Science in Aerospace Engineering Department, Middle East Technical University** by,

Prof. Dr. Halil Kalıpçılar
Dean, Graduate School of **Natural and Applied Sciences** _____

Prof. Dr. İsmail Hakkı Tuncer
Head of Department, **Aerospace Engineering** _____

Prof. Dr. İsmail Hakkı Tuncer
Supervisor, **Aerospace Engineering, METU** _____

Examining Committee Members:

Prof. Dr. Yusuf Özyörük
Aerospace Engineering Department, METU _____

Prof. Dr. İsmail Hakkı Tuncer
Aerospace Engineering, METU _____

Prof. Dr. Hüseyin Nafiz Alemdaroğlu
School of Civil Aviation, Atılım University _____

Assoc. Prof. Dr. Sinan Eyi
Aerospace Engineering Department, METU _____

Assoc. Prof. Dr. Utku Kânoğlu
Aerospace Engineering Department, METU _____

Date: 10.09.2019

I hereby declare that all information in this document has been obtained and presented in accordance with academic rules and ethical conduct. I also declare that, as required by these rules and conduct, I have fully cited and referenced all material and results that are not original to this work.

Name, Surname: Mehmet Başaran

Signature:

ABSTRACT

ADJOINT-BASED DESIGN OPTIMIZATION OF A HYPERSONIC INLET

Başaran, Mehmet
Master of Science, Aerospace Engineering
Supervisor: Prof. Dr. İsmail Hakkı Tuncer

September 2019, 119 pages

The inlet is one of the most essential parts of a scramjet engine. Its performance heavily affects the overall performance of the engine. The conventional scramjet inlet designs consist of a combination of multiple flat ramps. As the number of ramps increases, the total pressure recovery increases. However, the length and the weight of the engine also increase. In this study, the total pressure recovery of a single-ramp scramjet inlet is improved by aerodynamic shape optimization. In addition, the mass flow rate of the inlet is also maximized to increase the thrust. While performing the multi-objective optimization, the static pressure at the exit of the inlet is constrained to provide robust combustion. SU2 software with its discrete adjoint-based optimization tool is employed. It is observed that the optimum inlet design obtained satisfies both the shock-on-lip and the shock-on-shoulder conditions.

Keywords: CFD, Adjoint Method, Design Optimization, Scramjet Inlet, Hypersonic Flow, SU2

ÖZ

ADJOİNT TABANLI HİPERSONİK HAVA ALIĞI TASARIM OPTİMİZASYONU

Başaran, Mehmet
Yüksek Lisans, Havacılık ve Uzay Mühendisliği
Tez Danışmanı: Prof. Dr. İsmail Hakkı Tuncer

Eylül 2019, 119 sayfa

Hava alığı, scramjet motorunun en önemli parçalarından biridir. Hava alığının performansı, motorun genel performansı üzerinde oldukça etkilidir. Geleneksel scramjet hava alığı tasarımları düz rampalardan oluşmaktadır. Rampa sayısı arttıkça toplam basınç geri kazanımı artar. Bununla birlikte, motorun uzunluğu ve ağırlığı da artar. Bu çalışmada, tek rampalı bir scramjet hava alığının toplam basınç geri kazanımı aerodinamik şekil optimizasyonu ile geliştirilmiştir. Ek olarak, motorun itkisini arttırmak için hava alığının kütle debisi arttırılmıştır. Bu çok amaçlı optimizasyon gerçekleştirilirken, hava alığının çıkışındaki statik basıncın yanmayı olumsuz etkileyebilecek kadar düşmemesi için buradaki static basınç sınırlandırılmıştır. Bu çalışmada SU2 yazılımının ayrık eklenik bazlı optimizasyon (İng. discrete adjoint-based optimization) aracı kullanılmıştır. Elde edilen optimum hava alığı tasarımının hem dudakta şok hem de omuzda şok koşullarını sağladığı görülmüştür.

Anahtar Kelimeler: HAD, Adjoint Yöntemi, Tasarım Optimizasyonu, Scramjet Hava Alığı, Hipersonik Akış, SU2

To my lovely grandmother...

ACKNOWLEDGEMENTS

TABLE OF CONTENTS

LIST OF TABLES

LIST OF FIGURES

FIGURES

xiv

LIST OF ABBREVIATIONS

ABBREVIATIONS

AUSM	Advection Upstream Splitting Method
BD1	Baseline Design 1
BD2	Baseline Design 2
BD3	Baseline Design 3
BD4	Baseline Design 4
CFD	Computational Fluid Dynamics
CUSP	Convective-Upwind-Split-Pressure
DES	Detached Eddy Simulation
EST	Enumerative Search Techniques
FFD	Free Form Deformation
FVM	Finite Volume Method
HLLC	Harten-Lax-van Leer-Contact
JST	Jameson–Schmidt–Turkel
LES	Large Eddy Simulation
PDE	Partial Differential Equation
RANS	Reynolds-Averaged Navier-Stokes
RST	Random Search Techniques
SA	Spalart Allmaras
SA_E	Spalart-Allmaras with Edwards Correction
SST	Shear Stress Transport

LIST OF SYMBOLS

SYMBOLS

a	Acceleration
A	Area
c	Speed of Sound
C	Constraint
C_{pc}	Specific Heat of the Air at Constant Pressure
E	Total Energy
F	Thrust
F_{net}	Net Force
f	Mass Flow Fraction of Fuel to Air
f_b	Body Forces
h	Enthalpy
H_t	Total Enthalpy
J	Objective Function
k	The Coefficient of Thermal Conductivity
M	Mach Number
P	Static Pressure
P_{tot}	Total Pressure
$P_{tot,exit}$	Total Pressure at the Exit of Scramjet Inlet
$P_{tot,freestream}$	Total Pressure at Freestream
R	Governing Equation

Re	Reynolds Number
s	Entropy
T	Temperature
U	Flow Variables
u	Velocity
Q	Net Heat Transfer
W	Net Work
x	Design Variable
γ	Specific Heat Ratio
δ	Boundary Layer Thickness
δ_{ij}	Kronecker Delta
η_C	Compression Efficiency
$\eta_{C(ad)}$	Adiabatic Compression Efficiency
η_{KE}	Kinetic Energy Efficiency
$\eta_{KE(ad)}$	Adiabatic Kinetic Energy Efficiency
λ	Adjoint Variable
μ	Dynamic Viscosity
π_c	Total Pressure Recovery
ρ	Density
σ_{ij}	Stress Tensors
ΔU	Internal Energy
$\dot{m}$	Mass Flow Rate
$\dot{q}$	Heat Transfer

CHAPTER 1

INTRODUCTION

The desire to fly is an ongoing passion since ancient times. However, the birth of modern aviation may be considered the flight of the first powered and controlled airplane achieved by the Wright brothers in 1903. This adventure continued with Robert H. Goddard's first liquid-fueled rocket launch in 1926. Aircraft and rocket designers have worked hard to make their vehicles faster, go farther, higher and more easily controllable from those days to today. Deepening space research over the last 60 years has led to the development of even faster vehicles. Due to this rapid progress in aircraft and guided missile systems make the hypersonic flow one of the most interesting subjects for the last years' aerospace industry.

1.1. Hypersonic Vehicles

Hypersonic implies a flight above Mach 5 speeds [1]. For the hypersonic flight system, three distinct kinds of vehicles can be classified in view of their different design and technology features. These are winged re-entry vehicles (WRVs), non-winged re-entry vehicles (NWRVs), and airbreathing cruise and acceleration vehicles (CAVs) [2]. WRVs are usually initiated via rocket boosters and operate in the range of 30-0 Mach. They have blunt configuration. Their flight time generally is shorter compared to other types. During operating times, they are subjected to high angles of attack. US Space Shuttle, Russian Buran and European HERMES are typical examples of WRVs. NWRVs are designed to transport payloads into space and bring them back from space to the earth. Typically, they are started with rockets [3]. During ascent and re-entry, the vehicle encounters serious mechanical and thermal loads. In order to handle these loads, NWRVs have a simple and compact design. They do not have an aerodynamic control surface. Capsules and entry probes are intrinsic to this class. APOLLO,

SOYUZ capsules and BEAGLE2 probe are some examples of NWRVs. Like the other two types, CAVs also require rocket boosters or mother aircraft to be started. Air-breathing propulsion system serves in the cruise phase after separation is complete. They have got an aircraft-like design. In contrast to WRVs, they are operating at low angles of attack. Flight Mach numbers would be as high as 12 [4]. This kind of vehicle is one of the most promising technology to decrease long-haul civil flights. Examples of CAV's include vehicles X-51 A [5] and X-43 A. The focus of this study is on scramjet engines used by this type vehicles.

1.2. Scramjet Engines

Scramjet is an air-breathing engine. It is the key technology needed to make sustained hypersonic flight possible in the atmosphere [1]. It is a variation of the ramjet engine. While scramjet decelerates the freestream hypersonic air to supersonic speeds before combustion, burning occurs at subsonic speeds in a ramjet. If the incoming air in the scramjet had been attempted to reduce it to subsonic speeds, as in the ramjet, the losses due to shocks would be very significant and the temperature in the combustor would be very high. High temperature not only causes structural and material problems but can also cause air dissociation. It means energy loss in the engine.

The concept to add heat to a supersonic flow was firstly researched in 1946 by Roy [2]. The idea was nevertheless only seriously discussed by Weber and McKay. They investigate this subject in 1958 at NASA's Lewis Research Center [3]. This research showed that the scramjet performs superior at higher hypersonic flight speeds than ramjet [4]. Scramjet not only has superior characteristics than ramjet, but it also has superior characteristics than rockets for a wide flight regime. In order to compare efficiencies of different engine types, the specific impulse can be used. High specific impulse implies high efficiency. Comparing two engines which have distinct specific impulses, the engine with greater specific impulse would generate higher thrust with the same quantity of fuel [5]. Figure 1.1 shows the specific impulse levels for different propulsion systems. The specific impulse of scramjets is higher than the specific

impulse of rockets up to 20 Mach. They will be equalized after that speed. Figure 1.1 also demonstrates that the use of ramjet at 6-7 Mach levels is more effective than scramjet. However, Anderson et al. [6] state that a ramjet operating at higher speeds than 5 Mach would achieve very high static pressure in the combustion chamber. Therefore, in high flight Mach numbers, scramjets are preferred.
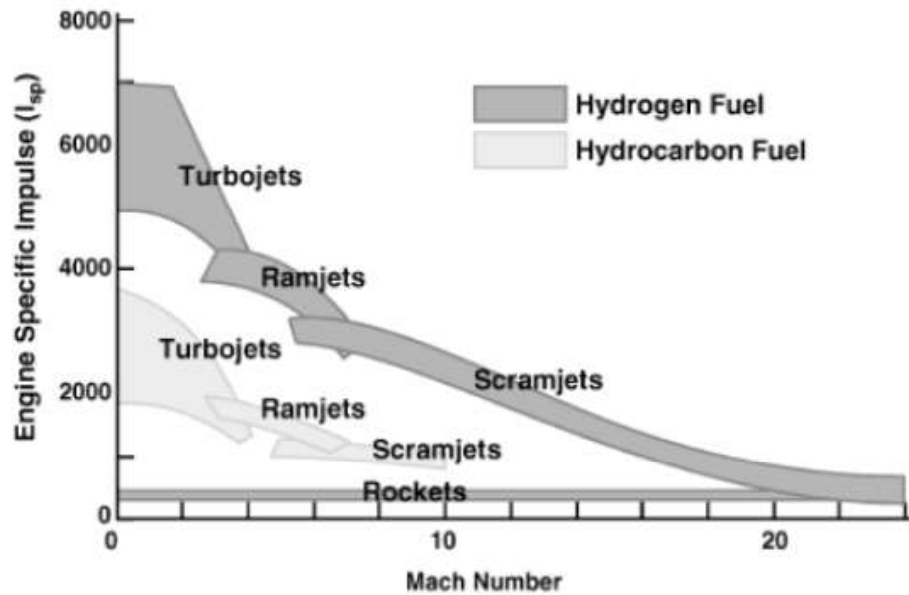
Figure 1.1. Specific impulse levels for different propulsion systems [7]
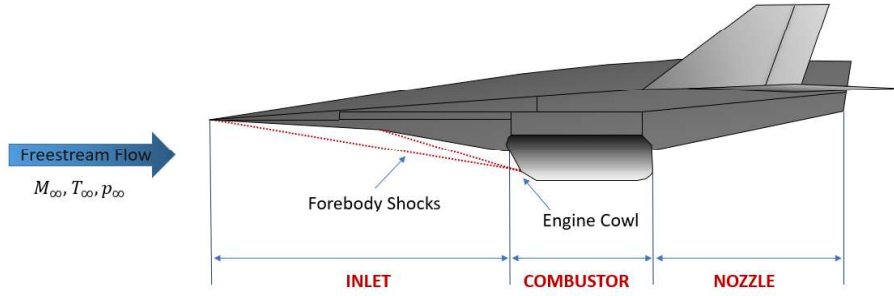
Figure 1.2. Generic diagram of a scramjet engine

Scramjet engines have vehicle integrated designs. They consist of three main components; inlet, combustor, and nozzle. A diagram of a scramjet is seen in Figure 1.2.

Incoming air is first compressed in the inlet. The working principles of ramjet and scramjets in compressing air are the same. They do not use rotating mechanical components in the inlet section, as opposed to other engine forms. In such engines, air is compressed through aerodynamic shocks. The compressed air is delivered to the combustor via the isolator, and the fuel is injected in this section. Then the burned air is expanded at the nozzle. Thus, the thrust is produced.

Fry divided the development of scramjets into four generations in chronological order: Beginning (1960-1973), Airframe Integration (1973-1986), NASP (1986-1994) and Resurgence (1995-today) [8]. The most large-scale scramjet development program in the first generation is the Hypersonic Research Engine (HRE). The program aims to develop a hydrogen-fueled and hydrogen-cooled scramjet engine. In this generation, experiments have been carried out at low hypersonic speeds (up to 7 Mach) [9]. These experiments also showed that the external drag of a pod type scramjet engine is extremely high [3]. Therefore, the focus of technology development in the second generation has moved to the integration of hydrogen-fueled scramjet engines onto a hypersonic vehicle. The third generation began with National Aerospace Plane (NASP) program launched by the United States. The program aims to create an aircraft-like vehicle, with scramjet cycle, that can achieve the orbit in a single stage.

The program also had the objective of accomplishing 25 Mach with this vehicle. However, a maximum of 7 Mach in the experiments was reached with the technology in 1984. The fourth generation covers scramjet studies from 1995 to the present. In this time frame, there are many flight-tested scramjet investigations. HyShot II, developed by the University of Queensland in Australia (2002), is considered to be the first successful scramjet flight test [9]. Figure 1.3 shows the simple and robust design of the HyShot II payload. The achievement of the HyShot II has resulted in considerable interest in low-cost scramjet flight tests using rocket boosters [3].

Figure 1.3. HyShot II Payload [3]

Figure 1.4. X-43A Hypersonic vehicle [10]

NASA is another institution that is investigating this topic. In 2004, they conducted the Hyper-X program with two successful flights. The vehicle in this program is called as X-43A. On the first flight, it achieved 6.4 Mach and on the second one 9.6 Mach. The image of X-43A is given in Figure 1.4.

An additional hypersonic cruise vehicle with a scramjet engine is the X-51A [11]. There are four flight tests known to date. The first and final of these flights have been successful, while the second and third have failed. The last flight test of X-51A performed in 2013 is the hypersonic flight with the longest scramjet engine ever performed. The image of X-51A is given in Figure 1.5.
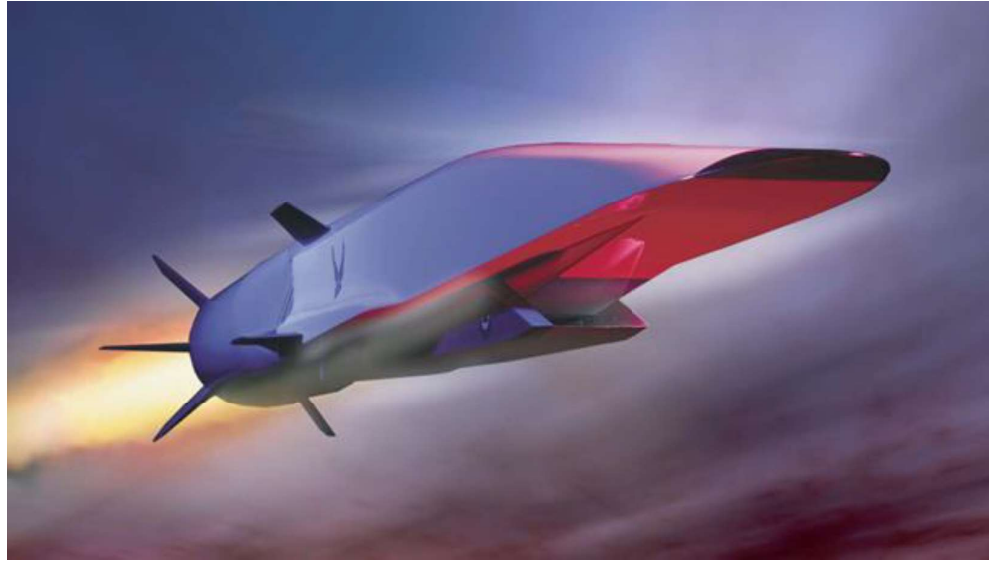
Figure 1.5. X-51A Waverider hypersonic vehicle [10]

In addition to the aforementioned vehicles, there have been many attempts to develop a hypersonic vehicle with a scramjet engine. The main ones are HyFly [12], Falcon HTV-3X [13], HSTDV [14], 14X [15] and LEA [16].

The current study is mainly related to the inlet component of scramjet engines. Scramjet inlets are discussed in detail in the following section.

1.3. Scramjet Inlets

Inlet is the component where the air enters the engine. The purpose of the inlet in any airbreathing engine is to capture the air at maximum flow rate possible in order to provide maximum thrust and to compress it [6]. The vehicles designed for the flow regime under Mach 3 need rotating mechanical components in the inlet part to compress the air while inlets of ramjet and scramjet which operate at higher speeds can provide the sufficient compression level without rotating parts. The working principles of ramjet and scramjet inlets are based on aerodynamic shocks. Compression in ramjet is carried out in a combination of oblique and normal shocks. However, scramjet uses only oblique shocks for compression. Therefore, flow speed never drops subsonic before combustion in scramjet.

1.3.1. Scramjet Inlet Types

There are three different inlet types depending on where compression occurs. These are internal compression, mixed compression, and external compression. All compression for internal type takes place inside the motor. These inlets are shorter than mixed type inlets, and it is an advantage to get a lighter engine. However integration of these inlets to the vehicle is not as easy as other kinds. Internal inlets always require a changeable geometric design to start. Axisymmetric versions of these inlets are referred to as Busemann inlet [17]. Figure 1.6 illustrates a diagram of an internal compression inlet.
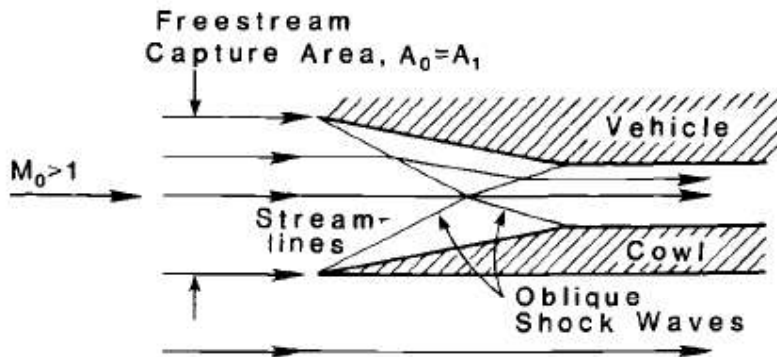
Figure 1.6. Internal compression inlet [17]

Aerodynamic shocks to be used for the compression process in mixed compression inlets are located both inside and outside the engine. These inlets are longer than other types. However, the cowl and the freestream flow can be adjusted parallel to each other when designing these inlets. This results in less drag than the external compression type. A movable design may be required to start. Schematic representation of mixed compression inlet is given in Figure 1.7.
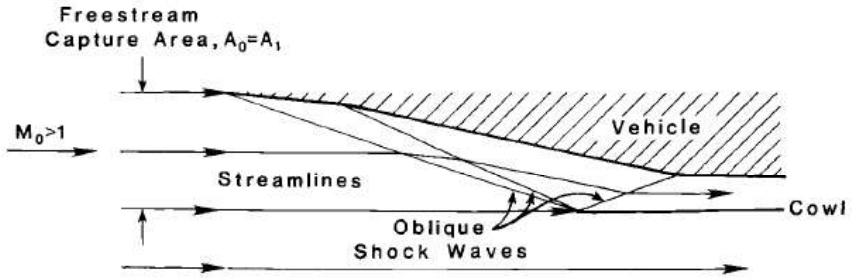
Figure 1.7. Mixed compression inlet [17]
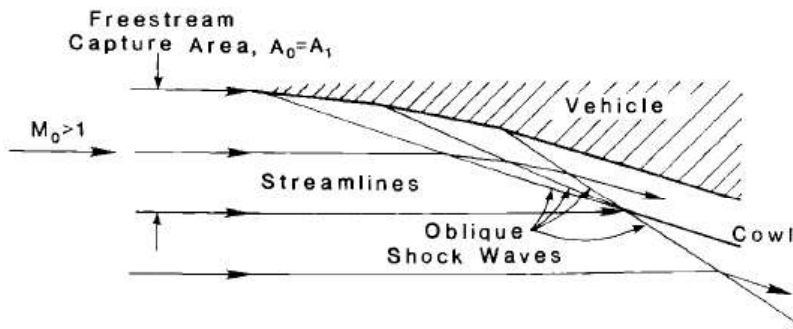
Figure 1.8. External compression inlet [17]

For external compression type inlets, the entire compression process is completed before the air enters the engine. Various oblique shock waves produced by the external compression ramps are intersected at the lip of the cowl at design condition. The flow inside of the engine is uniform and parallel to the surfaces. Usually these inlets have higher drag than others, but they are self-starting. A generic diagram of these type inlets is presented in Figure 1.8.

Most of the scramjet engines designed to date have used a mixed compression type inlet. The inlet type assessed in the current study is a mixed compression type.

1.3.2. Inlet Aerodynamics

The flow behavior on scramjet inlets is very complicated. There are several aerothermodynamic characteristics to be considered. These aerothermodynamic

9

characteristics include high-temperature effects, blunt leading-edge effects, hypersonic viscous interactions, and boundary layer separation.

High-temperature effects are one of the primary concerns of scramjet inlets. The hypersonic flow contains a considerable amount of kinetic energy. A part of the kinetic energy of this flow is converted to thermal energy because of its deceleration with oblique shocks and viscous effects. Thus, the temperature in the inlet increases. High temperature may result in dissociation of air molecules. It causes performance loses for the inlet.

Another design issue is the shape of leading edges of cowl lip and the forebody. These leading edges should be designed as blunt in order to avoid excessive heating levels in hypersonic flights. However, the bluntness causes decrease in performance of the inlet. Curved bow shocks and large entropy layers occur at the leading edges due to bluntness. They affect the inviscid flowfield and air capturing characteristics [6].

The boundary layer thickness (δ) depends on the Reynolds number (Re) and the Mach number (M). Equation 1.1 provides the relationship between M, Re, and δ [18].

$$\delta \propto \frac{M^2}{\sqrt{Re}}$$ *Equation 1.1*

Since M is high in hypersonic vehicles and the density at the altitudes at which these vehicles serve is low, therefore Re is low, a thick boundary layer forms on the vehicle surface. The thick boundary layer in the hypersonic flow causes a large displacement on the inviscid flow outside the boundary layer. This causes the vehicle body to behave larger than it is. The very large boundary layer also affects the inviscid flow outside the boundary layer and causes the boundary layer to grow further. This interaction between the boundary layer and the inviscid flow outside the boundary layer is called viscous interaction. It creates curved shock waves from the leading edge as illustrated in Figure 1.9. Also, it affects the pressure distribution on the surface, and increases drag and heat transfer [18]. For such reasons, viscous interaction in scramjet inlet designs should be assessed carefully.
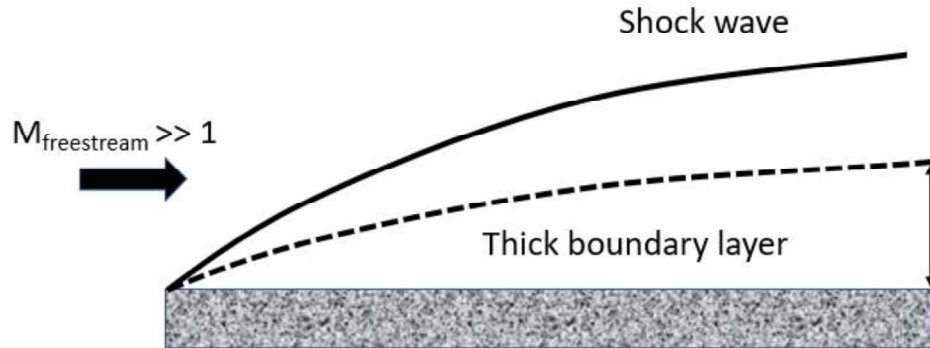
Figure 1.9. Effect of viscous interaction to shock wave

Another important issue for scramjet inlets is the separation of the boundary layer. Since the mission of a scramjet inlet is to compress incoming air before it goes to the combustion chamber, high adverse pressure gradients may occur on the inlet boundary layer. This can cause separation. Also, the shock wave/boundary layer interaction can cause separation. It is an undesirable phenomenon and is often attempted to avoid it in inlet designs. However, boundary layer separations are usually observed in the compression corners, shock reflection, and shock cancellation regions. Figure 1.10 illustrates these cases.
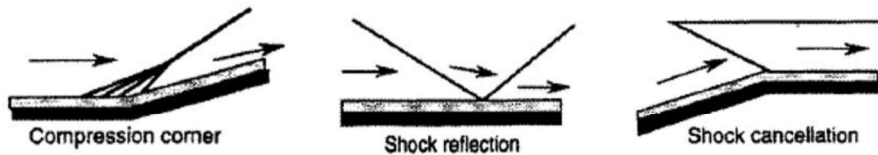
Figure 1.10. Boundary layer separations in compression corners, shock reflection and cancellation regions [6]

Boundary layer separation is undesirable because they can have many negative consequences. For example, they create new, undesirable shocks on the inlet. They cause excessive pressure rise and loss of valuable flow properties such as total pressure. It also leads to high heat transfer regions during the reattachment phase. The occurrence of acoustic loads due to unsteady waves on the inlet is another negative

11

result of boundary layer separation. Furthermore, it may even cause the inlet to unstart [6]. All these drawbacks show that designers should prevent the formation of boundary layer separation at their inlets as much as possible.

1.3.3. Inlet Design Issues

As described in "Inlet Aerodynamics" section, there is a complex flow over the scramjet inlets. Therefore, the scramjet inlet design process must be carried out very carefully. This section describes the main issues that should be considered during the design phase. One of the major problems of scramjet inlets is to unstart. If an inlet contracts too much towards to the throat as it makes the flow choke or the back pressure level is too high, the inlet may be in an unstarted mode. In such a case, the scramjet inlet cannot perform its task properly. Although, scramjet inlet starting issue researched widely in recent years, it is not yet well understood. Nevertheless, the findings of these researches indicated that both the internal contraction ratio and the contraction ratio of the inlet affect starting properties of it [19]. Internal contraction ratio is the ratio between the cowl lip area and throat area. Contraction ratio is the ratio between the captured flow area at the leading edge of the forebody and the throat area. A preliminary estimation for an internal contraction ratio where the inlet can start itself can be made from the Kantrowitz limit [20]. For a perfect gas, it is calculated according to Equation 1.2.

$$\left(\frac{A_2}{A_4}\right)_{\text{KANTROWITZ}} = \frac{1}{M_2}\left[\frac{(\gamma+1)M_2^2}{(\gamma-1)M_2^2+2}\right]^{\frac{\gamma}{\gamma-1}}$$
$$\left[\frac{\gamma+1}{2\gamma M_2^2-(\gamma-1)}\right]^{\frac{1}{\gamma-1}}\left[\frac{1+\frac{\gamma-1}{2}M_2^2}{\frac{\gamma+1}{2}}\right]^{\frac{\gamma+1}{2(\gamma-1)}} \qquad \textit{Equation 1.2}$$

where, A_2 is the cowl lip area, A_4 is the throat area, M_2 is the Mach number at the cowl lip and γ is the specific heat ratio. Kantrowitz limit is considered as starting limit and its variation along the Mach number is given in Figure 1.11. Kantrowitz limit states that for a self-started inlet, the ratio between the cowl lip area and throat area

should be above the Kantrowitz limit line presented in Figure 1.11. However, it shows that there are several inlets in started mode, although they are beyond the Kantrowitz limit. This is because the Kantrowitz limit has a conservative approach.
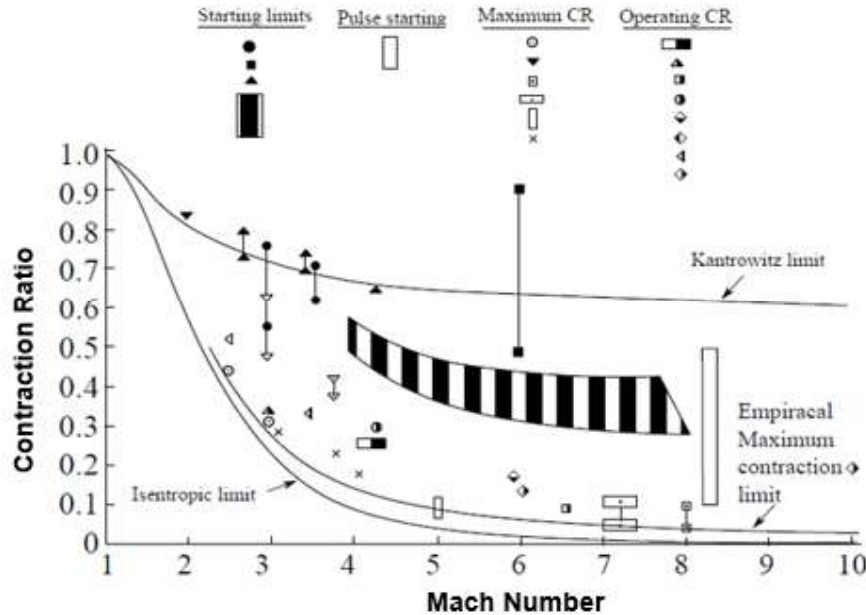
Figure 1.11. Variance of maximum contraction and starting limits for different Mach number [6]

Figure 1.11 also shows isentropic limit for scramjet inlets. This limitation is used to determine the maximum contraction ratio. The isentropic contraction limit can be estimated by using Equation 1.3:

$$\left(\frac{A_4}{A_0}\right)_{\text{ISENTROPIC}} = M_0 \left[\frac{\gamma+1}{2}\right]^{\frac{\gamma+1}{2(\gamma-1)}} \left[1 + \frac{\gamma-1}{2}M_0^2\right]^{\frac{\gamma+1}{2(\gamma-1)}} \qquad \textit{Equation 1.3}$$

where, A_0 is the captured flow area at the leading edge of forebody, and M_0 is the freestream Mach number.

Also, an empirical approach is available for the isentropic limit. This approach is given in Equation 1.4.

13

$$\left(\frac{A_4}{A_0}\right)_{\text{EMPIRIC}} = 0.05 - \frac{0.52}{M_0} + \frac{3.65}{M_0{}^2} \qquad (2.5 < M_0 < 10)$$

<div align="right">Equation 1.4</div>

There is no scramjet inlet in a started mode having a contraction ratio greater than the contraction ratio allowed by the isentropic limit.

An inlet must capture the air at a maximum mass flow rate to produce maximum thrust. In order to achieve this, the shocks coming from the forebody and ramps should intersect at the cowl lip on design point. This situation is called shock-on-lip condition. If the freestream Mach number is higher than the design Mach number, shocks will enter the inside of the engine and that would cause to shock/boundary-layer interaction. When this is the case, the flow may separate and high heat loads may occur on the engine. It may even cause an unstart problem. If freestream Mach number is less than the design Mach number, shocks will intersect each other far away from the cowl lip and that will cause loss of compressed air and increase in spillage drag. Another design issue is the shock-on-shoulder condition. This means that the shock reflected from the cowl hits the shoulder of the inlet. If this condition is satisfied, the cowl shock will be canceled and there will be a uniform and parallel flow to the surface inside the isolator. However, it is necessary to have a very high contraction ratio to meet this condition [21]. Therefore, some designs may not meet this condition.
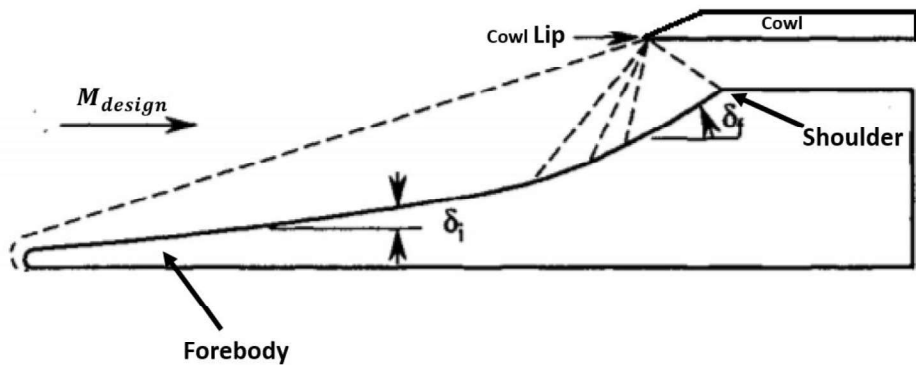
Figure 1.12. Shock-on-lip and shock-on-shoulder conditions [21]

1.3.4. Inlet Performance

Scramjet inlet performance is examined under two headings. These are capability and efficiency. While capability is related to the compression level, efficiency is associated with the amount of loss [22]. Both should be taken into account in a successful inlet design.

The compression level is one of the most critical parameters for an inlet. Previously, Smart researched the required compression level for scramjet inlets [23]. The study shows that overall scramjet cycle efficiency increases with decreasing Mach number. Also, it states that for overall cycle efficiency, pressure compression ratio is optimum when it is between 50 and 100. The pressure ratio higher than 100 does not affect the overall efficiency positively. The variation of overall efficiency with pressure ratio is given in Figure 1.13.
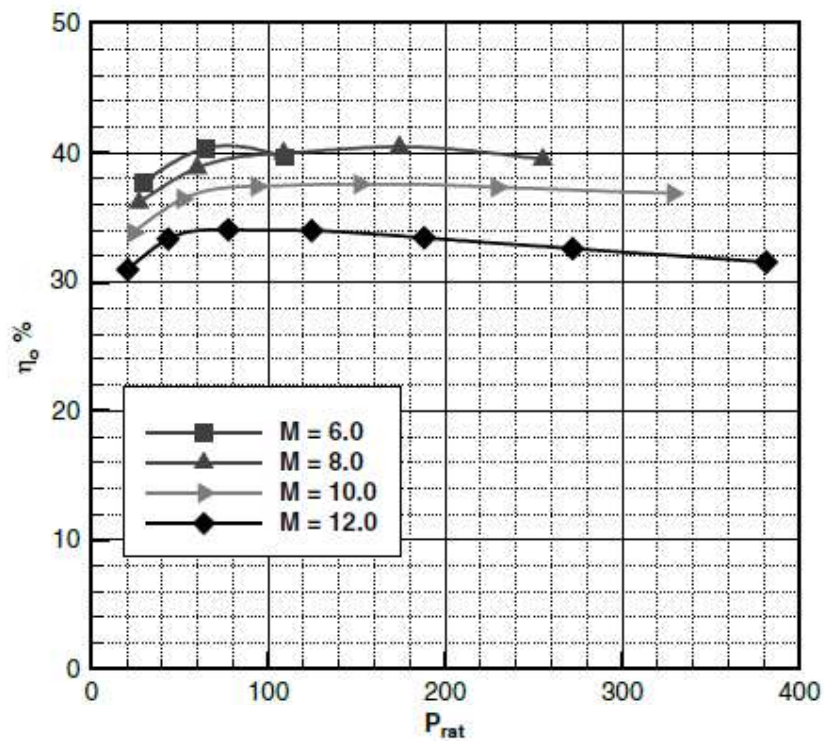
Figure 1.13. Overall scramjet cycle efficiency variation with pressure compression ratio [23]

Smart also achieved similar results for the relation of pressure compression ratio and specific impulse. It is also increasing with decreasing Mach number and it is optimum when the pressure compression ratio is between 50 and 100. The variation of specific impulse with pressure compression ratio is given in Figure 1.14.
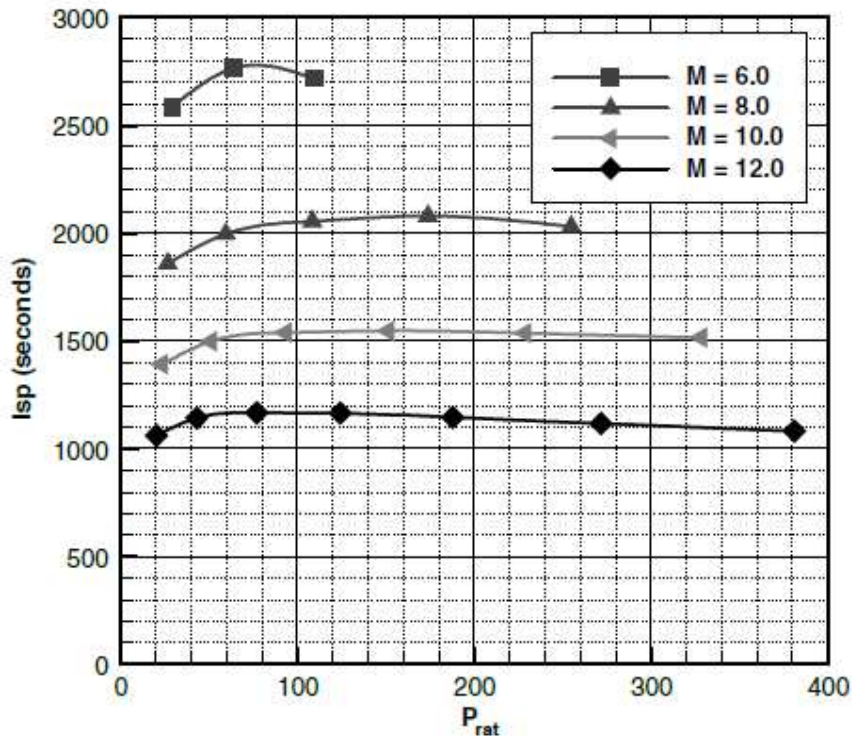
Figure 1.14. Specific impulse variation with pressure compression ratio [23]

However, there are several limitations to the pressure compression ratio for safe operation. The restrictions for the maximum pressure compression rate are non-equilibrium flow impacts in the nozzle and robustness limitations relevant to inlet start and boundary layer separation. The restriction for the minimal level compression rate is robust combustion requirement of the pressure compression ratio [23]. The minimum pressure level required to achieve successful combustion is independent of the Mach number but depends on the length of the combustor. For example, if the burner length is 0.1 m, the inlet should provide airflow at approximately 80 kPa. If the burner length is 0.3 m, as with most wind tunnel models, the inlet must provide airflow

at a pressure of approximately 50 kPa. If this length extends up to 1.0 m as in larger-scale flight vehicles, air at a pressure of 20 kPa is sufficient for combustion [23]. However, the pressure at the entrance of the combustor is generally expected to be greater than 50 kPa at a well-designed inlet [24].

Most common used efficiency parameters for scramjet inlets are total pressure recovery, kinetic energy efficiency, adiabatic kinetic energy efficiency, adiabatic compression efficiency, and dimensionless entropy increase.

The total pressure recovery, π_c, corresponds to the total pressure ratio between the exit of inlet and the freestream. It can be calculated by using Equation 1.5.

$$\pi_c = \frac{P_{tot,exit}}{P_{tot,freestream}}$$

<div align="right">Equation 1.5</div>

where $P_{tot,exit}$ is the total pressure at the exit of inlet and $P_{tot,freestream}$ is the total pressure of freestream.

π_c shows the total pressure loss during compression. π_c for scramjet inlets is lower than that of ramjets and turbojets [21].

Another efficiency parameter is kinetic energy efficiency, η_{KE}. It is a ratio of the kinetic energy of the compressed air if it is expanded to freestream pressure isentropically to the freestream kinetic energy. The calculation of it can be performed by using Equation 1.6.

$$\eta_{KE} = \frac{0.5 \, u_2'^2}{0.5 \, u_0^2} = \frac{H_{t2} - h'_2}{H_{t0} - h_0}$$

<div align="right">Equation 1.6</div>

where u is the velocity, H_t is the total enthalpy and h is the enthalpy. The subscript 0 represents freestream values and 2 represent inlet exit values. This parameter can be defined on the Mollier diagram as in Figure 1.15.
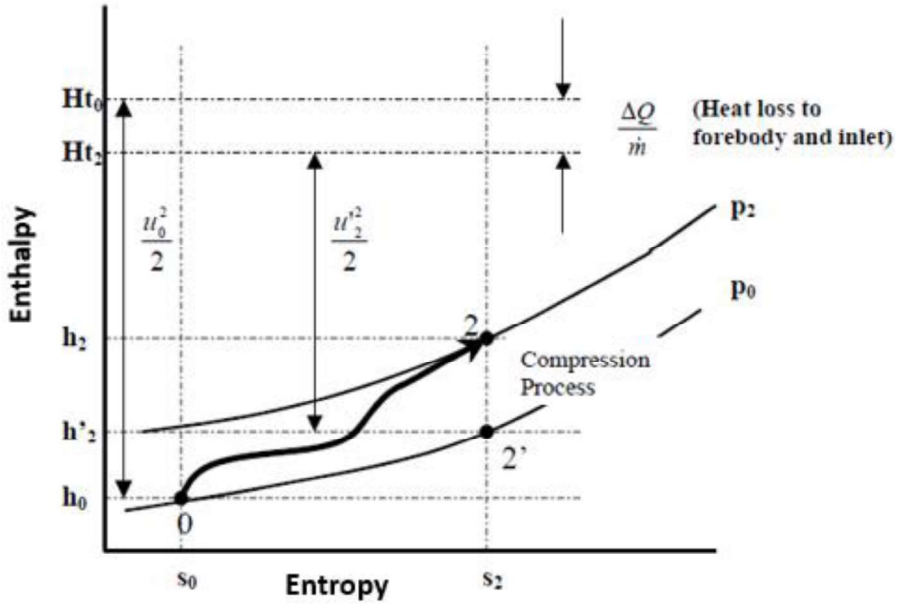
Figure 1.15. Mollier diagram for the scramjet inlet compression [22]

The adiabatic kinetic energy efficiency parameter, $\eta_{KE(ad)}$, is a modified version of η_{KE}. Heat loss is ignored in this parameter.

$$\eta_{KE(ad)} = \frac{H_{t0} - h'_2}{H_{t0} - h_0} \qquad \textit{Equation 1.7}$$

The final specific impulse and overall engine efficiency largely depend on the overall adiabatic compression efficiency, $\eta_{C(ad)}$. This value indicates how much energy is consumed during the compression process. It can be calculated as the ratio of the energy in the freestream flow to the total energy at the combustion chamber inlet, and this value is linearly related to $\eta_{KE(ad)}$.

$$\eta_{C(ad)} = 1 - \frac{(\gamma - 1)M_0^2}{2}\left(\frac{1 - \eta_{KE(ad)}}{T_2/T_0 - 1}\right) \qquad \textit{Equation 1.8}$$

where γ is the specific heat ratio, M is the Mach number, and T is the temperature. The subscript 0 represents freestream values and 2 represent inlet exit values.

18

Entropy increases during the compression process. The increase in entropy is divided by the specific heat of the air at constant pressure to obtain unitless version. It's a thermodynamic property and it is assessed as an efficiency parameter. It can be calculated with Equation 1.9.

$$\frac{s_2 - s_0}{C_{pc}} = \ln\left\{ {}^{T_2}\!/_{T_0} (1 - \eta_C) + \eta_C \right\} \qquad\qquad \textit{Equation 1.9}$$

where s is the entropy, η_C is the compression efficiency, and C_{pc} is the specific heat of the air at constant pressure. The subscript 0 represents freestream values and 2 represent inlet exit values.

In addition to capability and efficiency parameters, the mass flow rate can be assessed as a performance indicator of a scramjet inlet since it is directly related to the thrust of the engine. Thrust formula for scramjets is given Equation 1.10.

$$F = \dot{m}_0 c_0 M_0 \left((1 + f)\frac{M_{10}}{M_0}\sqrt{\frac{T_{10}}{T_0}} - 1 \right) + \frac{A_{10}}{A_0}\left(\frac{P_{10}}{P_0} - 1\right) \qquad\qquad \textit{Equation 1.10}$$

where F is thrust, $\dot{m}$ is mass flow rate, M is Mach number, P is static pressure, T is temperature, f is the mass flow fraction of fuel to air, and c is the speed of sound. In the above equation, subscript 0 represents freestream values and 10 represent nozzle exit values. Equation 1.10 demonstrates that a greater mass flow rate is required to achieve a greater thrust.

1.4. Optimization Techniques

Optimization is the method to achieve the best if what is 'good' or 'bad' can be measured and changed [25]. The search techniques used to discover the best are classified under three main headings. These are random, enumerative and gradient-based search techniques (Figure 1.16).
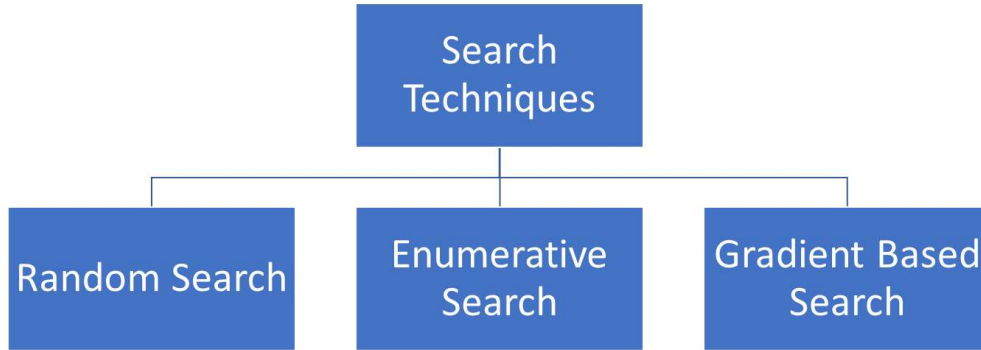
Figure 1.16. Search techniques for optimization

The determination of the starting points in random search techniques (RST) is performed by applying random sampling procedures. RST are very simple and they provide global maximum or minimum points rather than local ones. However, it is not possible to predict the convergence of RST, which progress very slowly and sometimes never converge. Another disadvantage of these methods is that they are very dependent on user choices [26].

The objective function is calculated for all combinations of design variables until the global maximum/minimum is achieved in the enumerative search techniques (EST). Although they are useful in small scale optimization problems, they are inefficient in large scale problems. This makes EST useless for most optimization problems of today.

Gradient-based techniques uses gradient information to achieve the best solution. In these techniques, the derivative of the objective function helps to reach the optimum. Unlike other techniques, having additional information (the gradient information) in this technique greatly improves the convergence of the search algorithm. Since all combinations in the design variable domain have not been tried, they are also suitable for large scale problems. They allow the solution of general sensitivity analysis problems governed by fluid dynamics models ranging from the full potential equation to the full compressible Reynolds-Averaged Navier-Stokes (RANS) equations.

Gradients can be computed with two different methods. These are finite difference and adjoint methods. The focus of this study is on adjoint methods. There are two types of adjoint methods: continuous adjoint approach and discrete adjoint approach (Figure 1.17). In the continuous adjoint approach, the adjoint equations are derived from the governing partial differential equation (PDE) and then subsequently discretized. The adjoint system has a unique form independent of the scheme used to solve the flow field system. However, in the discretized adjoint approach, the adjoint equations are directly derived from the discretized governing equations. This method gives gradients which are closer in value to exact finite-difference gradients.
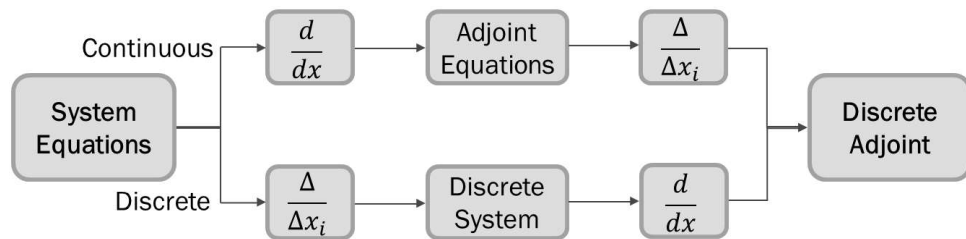
Figure 1.17. Continuous adjoint and discretized adjoint approaches

1.5. Literature Survey

Scramjet inlet design comprises aerodynamics, structures, noise, cost, and manufacturing issues. However, aerodynamics is directly related to the engine efficiency and thus the generation of thrust. The inlet aerodynamics is very complicated and it should be investigated extensively for effective engine design. Therefore many studies have been conducted in the research community with regard to inlet aerodynamic design.

In this part of the thesis, numerical scramjet inlet studies in the literature are examined. One of these works belongs to M. K. Smart [27]. Many different studies on this subject are quoted from this source. In the study, classical π_c optimization for two dimensional supersonic inlets is applied for scramjet inlets. If the shocks have equal

strength in a supersonic inlet, the optimal condition for maximum π_c is achieved. Smart's optimization study using the Lagrange multipliers method shows that this also applies to external shocks of the scramjet inlet. He presented the optimal π_c and turn angles for some typical scramjet inlet configurations up to five shocks. Another study is related with scramjet inlet optimization belongs to Ogawa et al. [28]. They used an axisymmetric inlet in their research. Their objectives are drag, adverse pressure gradient and η_C. Also, the temperature at the exit of the inlet is used as a constraint in their studies. The design variables are throat area, ramp lengths and angles. The number of the ramp is set to 3. In their study, it is observed that throat area is the most effective design variable for the constraint and all objective functions except adverse pressure gradient. Another optimization on scramjet inlet design was performed by Hasegawa et al. [1]. Their aim is to decrease the total pressure loss and drag of an inlet which will operate at 8 Mach and 35 km. The search technique using in this study is gradient-based. They use ramp lengths, angles and cowl position as design variables. They obtained an increase in π_c by %10, and they found that there is a tight tradeoff between π_c and drag. The research of Acharya et al. [29] is another study aims to improve π_c. Using various combinations of ramp angles and lengths, they designed two-shock and three-shock inlets that meet the shock on lip condition. Their findings are the same as Smart. They state that for an effective inlet design in terms of π_c, shocks' strength should be equal to each other. Raj et al. [30] are also researchers working on scramjet inlet. Their objectives are improving π_c and preventing separation in front of the shoulder. They used turning angles and gas dynamic relations while performing their study.

The above studies reveal that the optimization studies of scramjet inlets use ramp number, ramp length, ramp angle and position of cowl lip as design variables conventionally. In this thesis, a different method is used instead of traditional methods. In this approach, the design variables are the control points of the FFD box. In the literature, it is only Kline et al. that optimizes the inlet with this method. There are 3 publications including optimization studies using this method. In the first one, the

objective function is specified as $\dot{m}$ since it is directly related with thrust of the engine [31]. In the second study, in addition to RANS simulation of the inlet, also low fidelity models were used for the combustion and expansion process [32]. The combination of these models allowed to calculate the thrust of the engine. Thus, they could use the thrust as an objective function. Also, the nozzle exit area was optimized in this study. The third one is the doctoral thesis of Kline [33]. In the study, objectives are P_{tot} and thrust. Also, he defined the heat flux as a penalty in his study. All three studies uses the continuous adjoint approach to compute the gradients.

1.6. Objectives

The inlet for a scramjet engine is one of the most essential parts. Therefore, its performance is heavily effective on the overall performance of the engine. The conventional scramjet inlet designs consist of a combination of multiple flat ramps. The number of ramps refers to total pressure losses. As the number of ramps increases, π_c increases. However, the length of the engine also increases. A longer design means a heavier engine. The current study aims to improve the performance of a single-ramp inlet by an unconventional method. It is desired to maximize $\dot{m}$ and the average total pressure, P_{tot} at the exit surface of the inlet. While maximizing P_{tot} and $\dot{m}$; in order to provide required compression for robust combustion, averaged static pressure at the exit of the inlet is used as a constraint. Another objective of the study is generating an inlet design such that it is satisfied both the shock-on-shoulder and shock-on-lip conditions simultaneously. The same optimization strategy is applied in both inviscid and viscous flow optimizations. Using optimum designs, the difference between the two circumstances is assessed. These tasks are accomplished by aerodynamic shape optimization on the ramp. The discrete adjoint method is chosen to compute the gradients. SU2 software is selected as the solver. The Free Form Deformation (FFD) box strategy is used to define design variables and to deform the shape of the geometry.

Since the scramjet engine operates at 5 Mach and 25 km altitude, the first baseline geometry is designed such that shock-on-lip condition in inviscid Mach 5 flow is satisfied. Also in this design, Mach number at the combustor entrance is adjusted to be greater than 0.38 times of freestream Mach number which is another design criteria. In order to check the limits of the unusual technique used in this study, the ramp angle is indicated less than the examples in the literature. In the baseline design, shock-on-shoulder condition is neglected which is important to transform the air as parallel to engine surface. After the first baseline is optimized in terms of P_{tot} and $\dot{m}$, the tool sacrifices the shock-on-lip condition to provide the shock-on-shoulder condition. A new optimization process is introduced at this point. The previous optimization method is repeated for varying cowl lip positions. Also, the same process is repeated with a new baseline design in which the ramp angle is larger. Viscous flow optimizations are performed only the baseline designs have the bigger ramp angle.

1.7. Thesis Layout

This thesis will continue with the explanation of the methods used in the studies in Chapter 2. Verification studies, inviscid and viscous flow optimizations are provided in Chapter 3 after the background information has been presented. Chapter 4 includes a summary of the research and final comments.

CHAPTER 2

METHODOLOGY

Design optimization of propulsion systems has always been of great interest. Previously, inlet design optimizations were carried out using wind tunnel facilities. However, they are very costly, and it is hard to make an examination of the entire design space via this method [34]. In recent years, developments in computing systems have completely changed the design process. In order to reduce the duration and cost of the design process and to improve the quality of the designed product, automatized optimization with numerical simulation is now widely used in the industry. In the current study, a single-ramp scramjet inlet is optimized to maximize $\dot{m}$ and P_{tot} by using static pressure constraint with computational techniques. This section describes the methodology applied throughout the study.

2.1. Optimization Framework

The purpose of the current study is improving the performance of a single-ramp inlet by aerodynamic shape optimization. Adjoint based optimization is used to accomplish this task. This-method is one of the gradient based search techniques. The adjoint method is used to obtain gradient information during the optimization process. Flow solutions and adjoint solutions should be computed in the flow field for these kinds of problems. These solutions are obtained by using the open-source CFD suite SU2, developed in the Aerospace Design Lab at Stanford University. It is a RANS solver as well as it provides gradient information for optimal shape design by using adjoint method. The whole optimization process in the current study is conducted with this software. The optimization procedure within SU2 is shown in Figure 2.1.
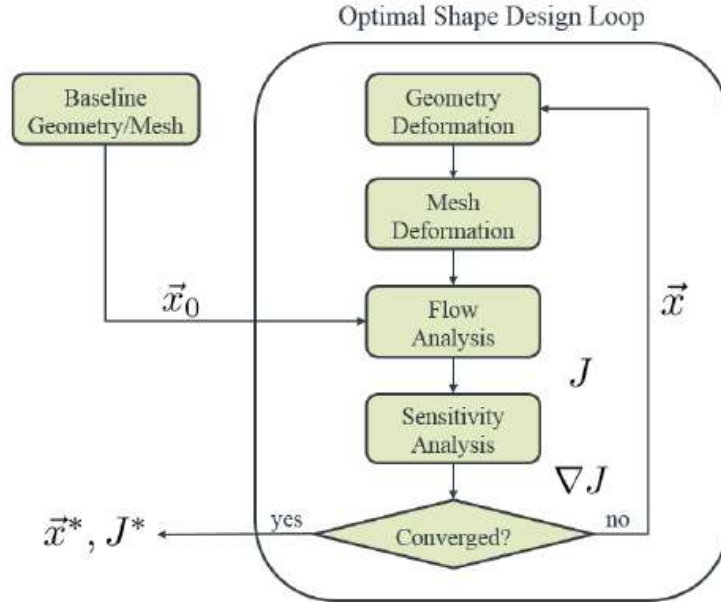
Figure 2.1. Optimization procedure within SU2 [35]

The SU2 software requires a baseline geometry and mesh as input. The optimization starts with the flow solver. This first step supplies the initial value of the objective function under the specified flight conditions with the baseline geometry. Then, the adjoint solution is obtained to estimate the gradient information. After this step, geometry and mesh are deformed. Then the objective function and gradient values are calculated on the new geometry. Until a convergent solution is achieved, the process keeps continuing.

2.2. Fluid Flow Modeling

The motion of a viscous fluid is described by Navier-Stokes equations. Analytical solution of these equations is quite difficult. Recently, it is possible with high-speed computers to obtain approximate solutions to these equations using various Computational Fluid Dynamics (CFD) techniques.

Navier-Stokes equations, turbulence models and numerical discretizations used to model fluid flow in this study are briefly discussed below.

2.2.1. Governing Equations

Navier-Stokes equations are the fundamental governing equations of fluid dynamics. Actually, they are a set of PDEs, namely the conservation equations of mass, momentum, and energy.

The mass conservation equation, or continuity equation, indicates that the mass is always conserved for a control volume. In other words, the amount of net mass which leaves from the control volume surface per unit time is equivalent to a change in mass of that control volume per unit time. If mass conservation is considered for a control volume with dimensions dx_1, dx_2, and dx_3, the continuity equation in tensor notation is obtained as given in Equation 2.1.

$$\frac{\partial \rho}{\partial t} + \frac{\partial (\rho u_i)}{\partial x_i} = 0, \quad i = 1, 2, 3$$

Equation 2.1

The conservation of momentum equation is an application of a fundamental physical principle to a model of the flow. In fluid dynamics, motion analysis is performed using Newton's laws of motion. Newton's 2nd law of motion states that the rate of change of momentum of a body is equivalent to the resulting force acting on the body. This physical principle is Newton's second law of motion (Equation 2.2).

$$\sum F_{net} = ma$$

Equation 2.2

According to this principle, the net force (pressure difference, viscous forces, body forces, and all other forces) acting on a fluid element is equal to the mass of the element and its acceleration. Thus, the most general form of momentum conservation equations is obtained by using tensor notation as given in Equation 2.3.

$$\frac{\partial (\rho u_i)}{\partial t} + \frac{\partial (\rho u_i u_j)}{\partial x_j} =$$
$$-\frac{\partial p}{\partial x_i} + \frac{\partial}{\partial x_j} \mu \left[\left(\frac{\partial u_i}{\partial x_j} + \frac{\partial u_j}{\partial x_i} \right) - \frac{2}{3} \frac{\partial u_k}{\partial x_k} \delta_{ij} \right] + f_b$$
$$i, j, k = 1, 2, 3$$

Equation 2.3

27

Here, body forces f_b can be neglected since the effect of this term is relatively small with respect to other terms.

Energy conservation equations are derived from the adjustment of the first law of thermodynamics to a fluid element. According to the first law of thermodynamics, the internal energy of a system (ΔU) is the sum of the net heat transfer (Q) to the system and the net work (W) applied to the system. As the equation, the first law of thermodynamics is given as follows.

$$\Delta U = Q + W \qquad \text{\textit{Equation 2.4}}$$

For a fluid element, conservation of energy equation in tensor notation is given in Equation 2.5.

$$
\frac{\partial(\rho E)}{\partial t} + \frac{\partial(\rho E u_i)}{\partial x_i} =
$$
$$
p\dot{q} + \frac{\partial}{\partial x_i}\left(k\frac{\partial T}{\partial x_i}\right) - \frac{\partial(u_i p)}{\partial x_i} + \frac{\partial(u_j \tau_{ij})}{\partial x_i} + \rho \vec{f}.\vec{V}
$$
$$
i,j = 1,2,3
$$

Equation 2.5

Then, the Navier-Stokes equations, which are the combination of mass, momentum, and energy conservation equations, are shown as follows.

$$\frac{\partial Q}{\partial t} + \frac{\partial F_i}{\partial x_i} = \frac{\partial G_i}{\partial x_i} \quad i = 1,2,3 \qquad \text{\textit{Equation 2.6}}$$

where Q is the state vector, F_i is the inviscid flux vector and G_i is the viscous flux vector. They are described as follows;

$$
Q = \begin{Bmatrix} \rho \\ \rho u_1 \\ \rho u_2 \\ \rho u_3 \\ \rho E \end{Bmatrix} \qquad \text{\textit{Equation 2.7}}
$$

$$
F_i = \begin{Bmatrix} \rho u_i \\ \rho u_i u_1 + p\delta_{i1} \\ \rho u_i u_2 + p\delta_{i2} \\ \rho u_i u_3 + p\delta_{i3} \\ \rho u_i H \end{Bmatrix} \qquad \text{\textit{Equation 2.8}}
$$

28

where H is the total enthalpy, $H = E + p/\rho$.

$$G_i = \begin{Bmatrix} 0 \\ \sigma_{ij}\delta_{j1} \\ \sigma_{ij}\delta_{j2} \\ \sigma_{ij}\delta_{j3} \\ u_j\sigma_{ij} + k\dfrac{\delta T}{\delta x_i} \end{Bmatrix}$$

Equation 2.9

σ_{ij} is the viscous stresses and they can be written as

$$\sigma_{ij} = \mu\left(\frac{\partial u_i}{\partial x_j} + \frac{\partial u_j}{\partial x_i}\right) + \lambda\delta_{ij}\frac{\partial u_k}{\partial x_k}$$

Equation 2.10

where μ is the dynamic viscosity, and λ is the kinematic viscosity. If G_i is equal to 0, the resulting system is known as Euler equations.

Actually there is another equation that is necessary to solve the system of equations. This is called the equation of state, and it is given in Equation 2.11.

$$p = \rho R T$$

Equation 2.11

In addition, to solve the system all terms of stress tensor should be specified. In CFD, stress tensor terms are approximately estimated by the turbulence models.

2.2.2. Turbulence Modelling

The flow over the scramjet inlets is highly turbulent, and the behavior of the turbulent flow has a high effect on engine performance. Therefore, turbulence should be effectively modeled in the aerodynamic analysis of scramjet inlets conducted with computational methods. In the current study, RANS based turbulence models are used. The adaptation of Navier-Stokes equations into RANS equations enables many engineering flows to be simulated. RANS equations are derived from the Navier-Stokes equations by using the mean values of turbulence-induced fluctuations. The RANS approach is more economical in terms of computational cost than other turbulence models such as Large Eddy Simulation (LES) and Detached Eddy

Simulation (DES). Therefore it is widely used in the industry. The results of three different RANS turbulence models available in SU2 (Spalart-Allmaras (SA), Spalart-Allmaras with Edwards Correction (SA_E), Menter shear-stress transport (SST)) are assessed against the experimental data in the verification part of the current study.

2.2.2.1. Spalart-Allmaras Turbulence Model

Spalart-Allmaras (SA) is a one-equation turbulence model. For the development of this model, empirical findings are used. This model aims to improve the estimates achieved by mixing-length models and providing a faster alternative to two-equation turbulence models [36]. In this equation model, only the term "k", which expresses turbulence kinetic energy, is included in the model.

2.2.2.2. Spalart-Allmaras with Edwards Correction Turbulence Model

Spalart-Allmaras with Edwards Correction (SA_E) is a modified version of SA turbulence model. The difference between the SA_E and SA is mainly related to the near-wall behavior of the strain rate norm. In the original application of the SA model, the behavior of the strain rate norm near the wall may produce an oscillating convergence behavior after a rapid period of decline in the residuals. SA_E model allows for a smooth and rapid convergence while maintaining the sensitivity of the original formulation close to the wall [37].

2.2.2.3. Menter Shear-Stress Transport Turbulence Model

Shear Stress Transport (SST) turbulence model is a two-equation turbulence model. It combines the strengths of other two-equation turbulence models (namely k-ω and k-ε turbulence models) into a single model. In this model, the coefficients are changed regionally. SST uses the k-ω turbulence model in regions close to the wall, while the k-ε turbulence model is used on the sides of the boundary layer edge and away from the wall. This change allows for better modeling of flows with high adverse pressure gradients and separations.

2.2.3. Numerical Discretizations

Space and time discretization of the governing equations are performed separately. The space-time separation enables a variety of distinct kinds of space and time integration models. In the SU2 software, the spatial integration of RANS equations is performed using the finite volume method, and it includes many convective flux scheme like JST, AUSM, HLLC, CUSP, and LAX-FRIEDRICH. For time integration there are many implicit and explicit methods [38]. For the current study, convective fluxes are discretized using second-order JST numerical scheme and time is integrated with the implicit Euler method.

2.3. Adjoint Method

Automatized optimization with numerical simulation is now widely used in the industry. However, for the large scale optimization problems which have numerous design variables, the CPU time is still notable. The decrease in the calculation time of the gradient of the objective function(s) can significantly minimize the time required for optimization. The adjoint method is efficient in this respect [33]. The adjoint method, like the finite difference method, is used to calculate the gradient of the objective function. Previously, Kline compared the required PDE solutions for adjoint methods and finite difference method to calculate the gradients of a function (Figure 2.2) [33].
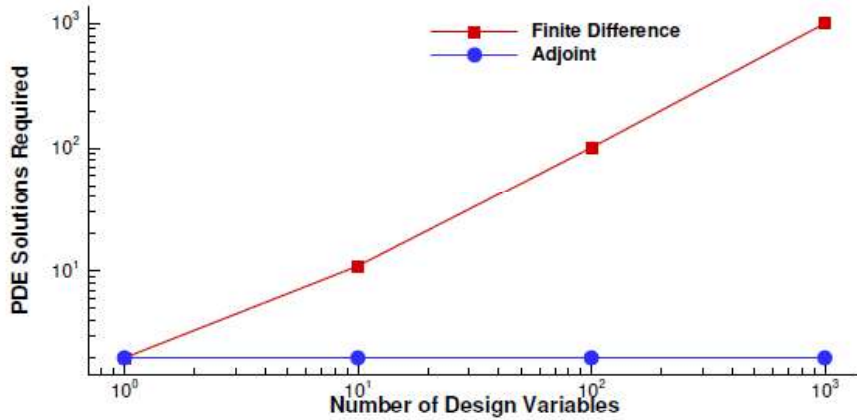
Figure 2.2. Required PDE solutions for adjoint method and finite difference method to calculate gradient of a function [33]

Figure 2.2 shows that finite difference method becomes more inefficient when the number of design variables increase since it requires more computations. However, the adjoint method is independent of the number of design variables.

The adjoint method requires a new PDE solution in order to find the sensitivity of the objective function. While performing the adjoint solution, the method uses the results of the flow solution. There are two types of adjoint methods: (i) continuous adjoint and (ii) discrete adjoint. In the continuous approach, adjoint equations are derived analytically from governing equations and then discretized. However, in the discrete approach, discretized adjoint equations are obtained from discretized governing equations. The SU2 software is capable of performing adjoint analysis using both approaches.

The continuous adjoint equations are not unique. They may differ according to the discretization method. This can in some cases damage the optimization process. In addition, the convergence behavior of discrete adjoint equations is better than the continuous ones [39]. Moreover, the discrete adjoint approach is usually more consistent with the gradients of finite difference.[33]. Kline verified the adjoint gradients of averaged static pressure and averaged total pressure with finite difference

gradients in his study [33]. His results are given in Figure 2.3 and Figure 2.4. Averaged static and total pressures were computed at an outflow boundary, and these computations were performed by using SU2. These are the common points of the current study and Kline's research.

Figure 2.3 and Figure 2.4 show that the agreement of adjoint methods with finite difference method is generally good. However, the discrete adjoint results are more close to finite difference gradients than the continuous adjoint results at some points. Therefore, the discrete adjoint solver of SU2 is chosen for the current study.
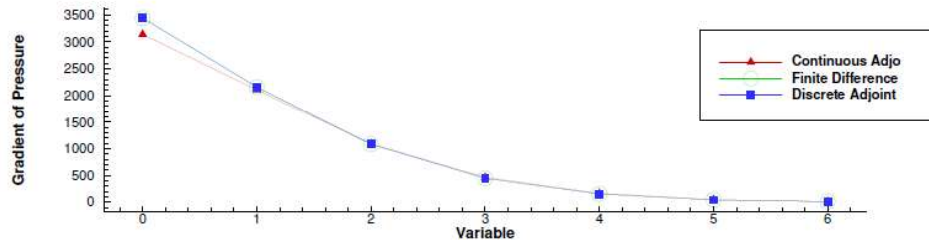
Figure 2.3. Comparison of continuous adjoint, discrete adjoint and finite difference methods for averaged static pressure gradients [33]
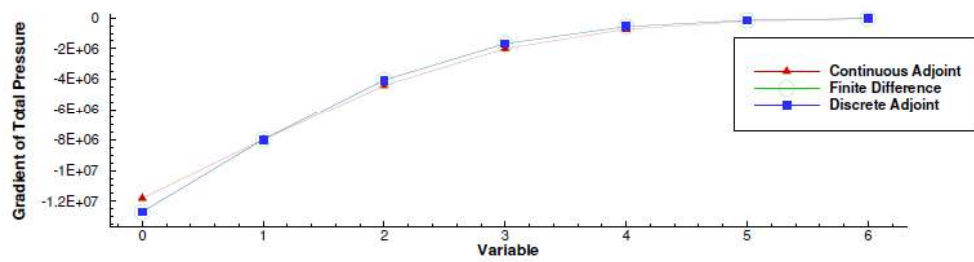
Figure 2.4. Comparison of continuous adjoint, discrete adjoint and finite difference methods for averaged total pressure gradients [33]

The derivation of discrete adjoint equations is known more difficult [40]. However, in the last years, automatic differentiation (AD) made it much easier [41]. Gauger's study may be helpful to get more detail information about AD [42].

The adjoint method with general terms is presented below.

Initially an objective function J is defined while deriving adjoint method.

$$J(U, x)$$

It depends on flow variables U and design variable x.

The aim is to compute the change in J with respect to varying x. However, the connection between x and U must be described to achieve this task. The governing equation R, which uses as a constraint while deriving adjoint equations, connects them to each other.

$$R(U, x) = 0$$

Then, δJ and δR can be shown as follows:

$$\delta J = \frac{\partial J}{\partial U} \delta U + \frac{\partial J}{\partial x} \delta x$$

$$\delta R = \frac{\partial R}{\partial U} \delta U + \frac{\partial R}{\partial x} \delta x = 0$$

δR is fixed to zero because it is a constraint and it should be satisfied for every δx and related δU. If δU is calculated from Equation 2.15, it can be put into Equation 2.14 in order to find $\frac{\delta J}{\delta x}$. However, this operation should be repeated when a new design variable is added. In order to eliminate this repetition, a new connection must be established between δJ and δx, that is independent of δU.

Since δR is equal to 0, the following equation can be written:

$$\delta J = \delta J - \lambda \delta R$$

where λ is adjoint variables.

If Equation 2.14 and Equation 2.15 are substituted into Equation 2.16 and the resulting equation is rearranged, the following equation will be obtained.

$$\delta J = \delta U \left(\frac{\partial J}{\partial U} - \lambda \frac{\partial R}{\partial U} \right) + \delta x \left(\frac{\partial J}{\partial x} - \lambda \frac{\partial R}{\partial x} \right) \qquad \text{Equation 2.17}$$

Equation 2.17 should be independent of δU, and λ can be chosen randomly. Thus, the following expression can be written.

$$\left(\frac{\partial J}{\partial U} - \lambda \frac{\partial R}{\partial U} \right) = 0 \qquad \text{Equation 2.18}$$

Equation 2.18, makes Equation 2.17 δU-independent, is called as adjoint equation, and λ can be determined from this equation. After λ is found, Equation 2.19 (a modified version of Equation 2.17) can be solved.

$$\frac{\delta J}{\delta x} = \left(\frac{\partial J}{\partial x} - \lambda \frac{\partial R}{\partial x} \right) \qquad \text{Equation 2.19}$$

Equation 2.19 represents the sensitivity of the objective function with respect to the design variable. At this point, the task is to solve the adjoint equation (Equation 2.18). This method is named as the adjoint method and it can be also applied to a system of PDEs.

2.4. Design Variables

In order to define design variables, Free Form Deformation (FFD) box strategy is used. In this strategy;

- A box covers the geometry to be redesigned is parameterized as a Bezier solid.
- On the surface of the box is specified a series of control points.
- The number of control points depends on the order of the chosen Bernstein polynomials.
- The cartesian coordinates of the points on the surface of the object are then transformed into parametric coordinates within the Bezier box.

- Control points of the box become design variables, and they control the shape of the solid.

Since the current study aims to improve the performance of the scramjet inlet by changing ramp geometry, an FFD box is created around the ramp of the baseline geometry. This FFD box is illustrated in Figure 2.5.
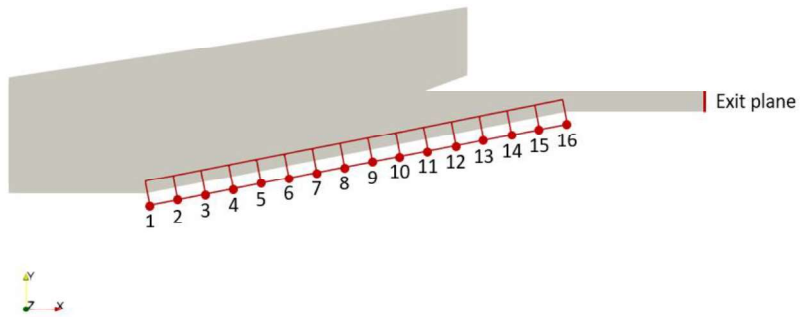
Figure 2.5. FFD box around the ramp of the baseline geometry

CHAPTER 3

RESULTS AND DISCUSSION

The performance parameters of a single-ramp scramjet inlet are improved by using the discrete adjoint method. This method needs the information of flow solutions. The flow solutions and the adjoint solutions are obtained via SU2 software. In Section 3.1, the verification studies are performed to check the capability of SU2. A parallel efficiency study is performed in Section 3.2. In Section 3.3, inviscid flow optimizations are presented. Finally, the viscous flow optimizations are given in Section 3.4.

3.1. Verification Studies

RANS simulation capability of the SU2 software is checked in this section. Inlet is the compression component of the scramjet engine. The flow on the inlet is very complex because there are many flow phenomena such as boundary-layer transition, shock wave-boundary layer interaction, boundary layer separation, and shock-shock interactions. It is quite difficult to resolve these issues with computational techniques. It should, therefore, be ensured that the solver is able to handle these challenges. Solver performance is directly related to the success of the product to be obtained after optimization. In order to test the performance of SU2 software in such problems, CFD analyses are performed with two different inlet geometries whose experimental data are available in the literature. CFD and experimental results are compared. These comparisons are given in the following subsections.

3.1.1. Scramjet Inlet at 5 Mach

Idris et al. used pressure-sensitive paint (PSP) and pressure transducers on ramps and isolator surface to investigate the shock structure of a two-ramped scramjet inlet at 5 Mach [43]. The inlet in the study satisfies the shock-on-lip condition in inviscid Mach

5 flow. In order to minimize P_{tot} losses, the strength of oblique shocks on the ramps is nearly equivalent. Another criterion in the inlet design is that the Mach number at the combustion entrance is more than 0.38 times the Mach number of the freestream. Otherwise, the inlet will have extremely high temperatures, which will cause air dissociation. Also, the Kantrowitz limit is satisfied in order to guarantee that the inlet starts self. However, the shock-on-shoulder condition is neglected. Figure 1 shows the inlet geometry used for this study. The complete length of the inlet is 155 mm and, it has two ramps. The deflection angle of the first ramp is 10 ° and of the second ramp is 12 °. The height of the isolator is equivalent to 6.8 mm and the width of the inlet is 36 mm. The pressure on the lower surface is measured using 12 transducers as seen in Figure 3.1.
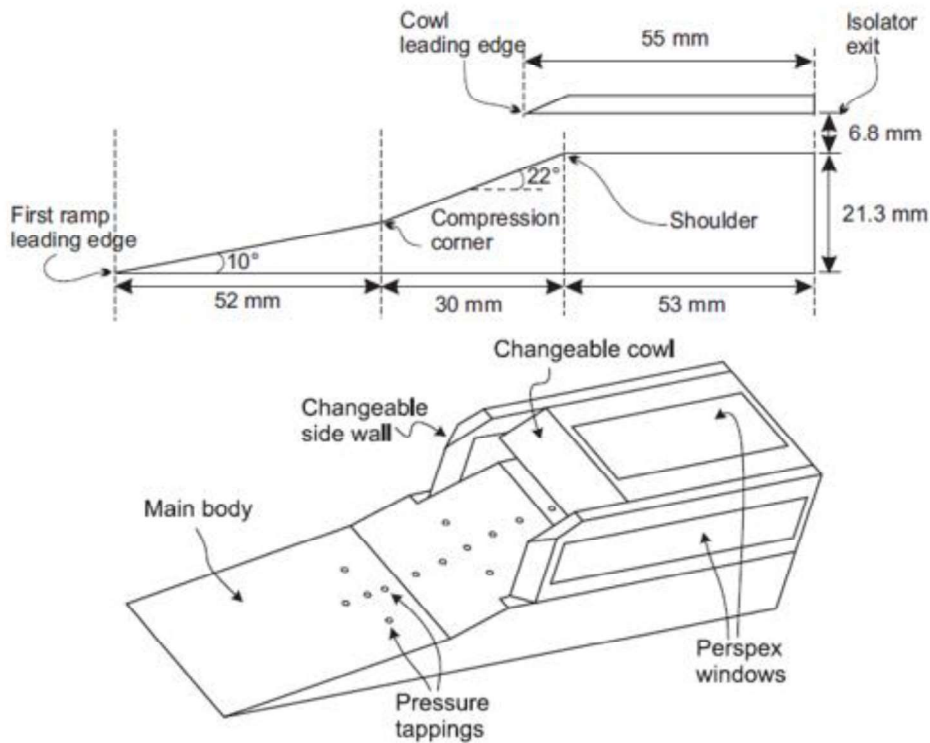
Figure 3.1. Dimensions of scramjet inlet at Mach 5 [43]

38

The effectivity of the grid refinement is examined. Then, the effect of SA, SA_E and SST turbulence models is evaluated. The results of these studies are given in the following sections.

In this work, 4 grids with different refinement levels are used to achieve a grid-independent solution. The convective fluxes are evaluated by the second order JST centered spatial discretization. The results of three different turbulence models available in SU2 (SA, SA_E, SST) are assessed against the experimental data [43]. The turbulence initialization parameters are adjusted according to values given in the reference study. The boundaries of the computational domain consist of an inlet, adiabatic wall, supersonic outlet and characteristic far-field boundary conditions (Figure 3.2). Freestream conditions are given in Table 3.1. Sutherland method is chosen as the viscosity model with the default settings of SU2.
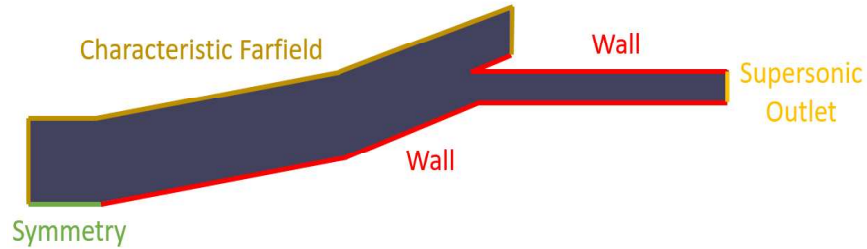
Figure 3.2: Boundary conditions

Table 3.1 Freestream conditions

Mach number	5.0
Angle of attack [°]	0
Freestream pressure [Pa]	1228.5
Freestream Temperature [K]	62.5

3.1.1.1. Grid Independence

The grid dependency analysis is performed by using 4 different grid refinement levels. The number of cells is given in Table 3.2. The first layer thickness is set to 2 microns to ensure that y+ value is smaller than 1.

Table 3.2 Number of cells of four different grid

Mesh 1	79200
Mesh 2	150568
Mesh 3	310484
Mesh 4	590446

Zoomed images to throat part of the inlet for 4 different grids are given in Figure 3.3.
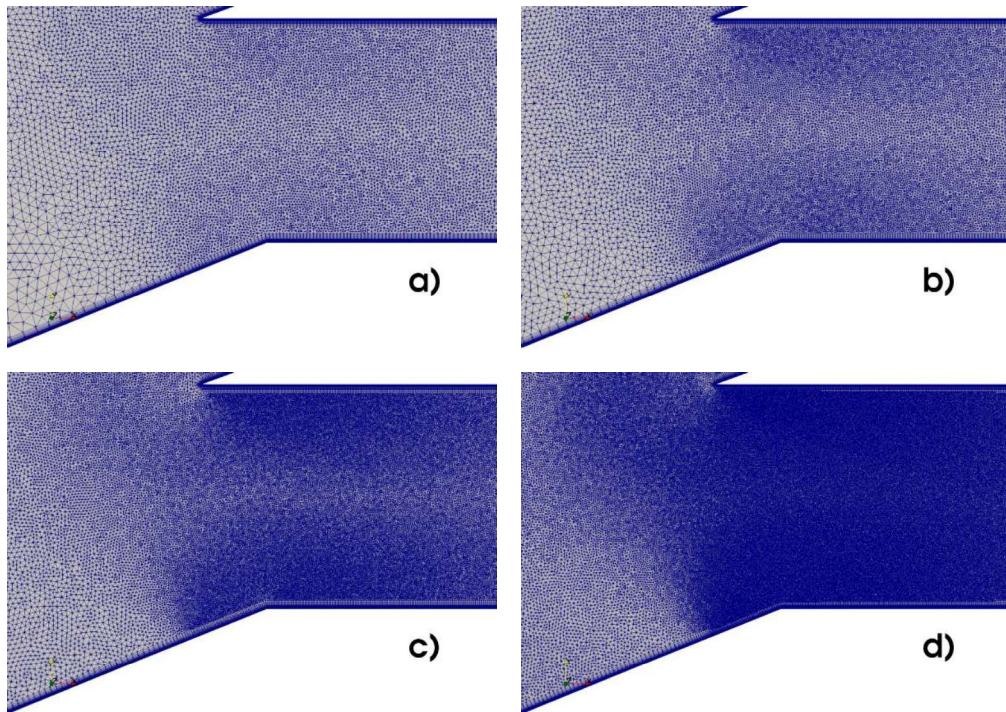
Figure 3.3. Zoomed images to throat for a) Mesh 1, b) Mesh 2, c) Mesh 3, d) Mesh 4

The pressure distribution on the lower surface (ramps and isolator surface) obtained from these grids are compared in Figure 3.4. It is observed that the refinement level

of grids does not have a significant effect on the ramps. However, the behavior of the flow inside the engine is dependent on the grid refinement level. Pressure increase at x/L = 0.84 cannot be captured with Mesh 1 and 2. A grid-independent solution is obtained with Mesh 3 having half the mesh count of Mesh 4 while converging to the same solution.
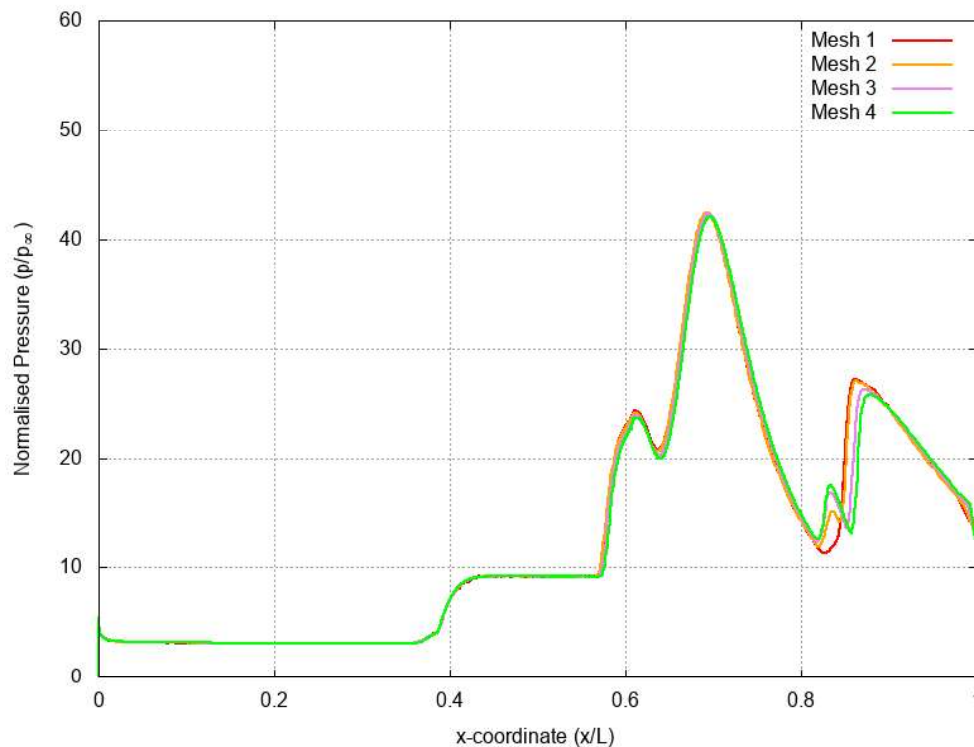
Figure 3.4 The comparison of different grid refinement levels

3.1.1.2. Effect of Turbulence Model

The results of 3 different turbulence models are compared with experimental data. Idris et al. used PSP and pressure transducers on ramps and isolator surface to investigate the shock structure of the baseline geometry of the current study. They also compared their results with CFD analysis. Their numerical and experimental data and SU2 results for the pressure distribution on the ramps and isolator surface are given in Figure 3.5. Black dots in this figure represent the transducer values, green ones represent the PSP results. The behavior of the SST turbulence model results differs

from that of other turbulence models and the experimental results. SST model captures the separation early with respect to other models and it gives different results than the experiment. This can be seen in Figure 3.6. Both SA and SA_E turbulence models are consistent favorably with the experimental data. SA model could not capture the pressure increase near x=0.84 seen in PSP result, whereas SA_E captures this pressure jump.
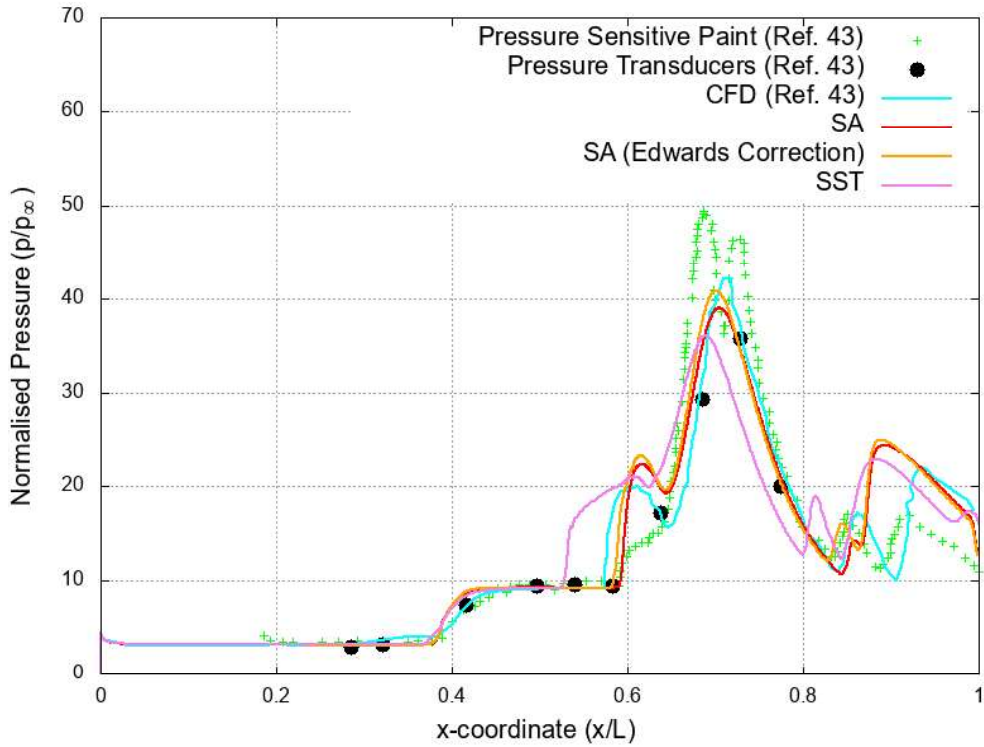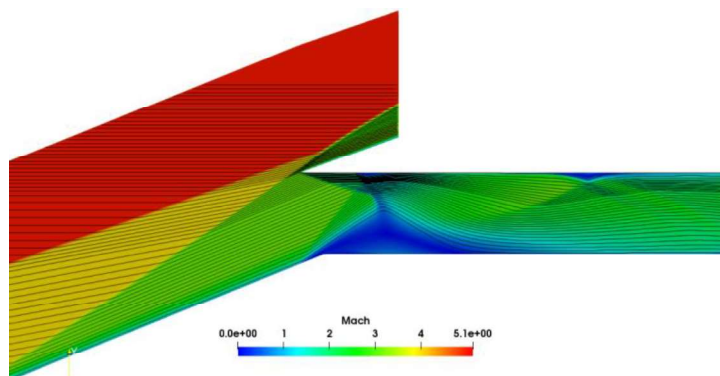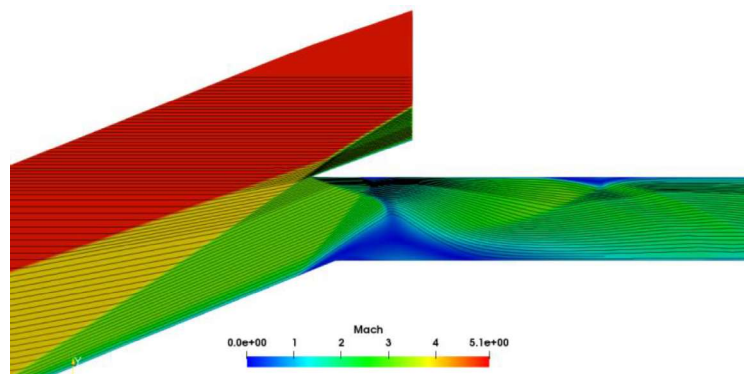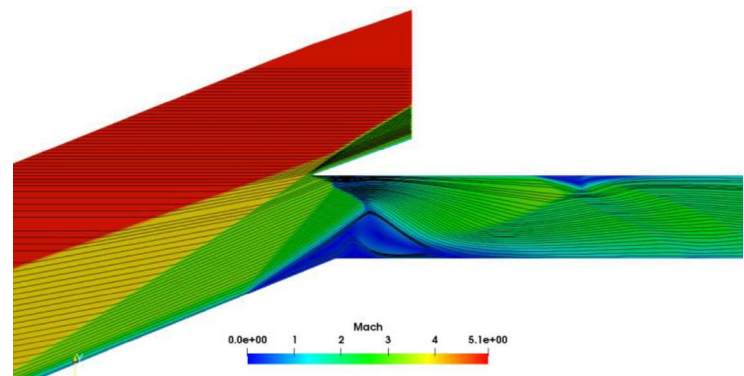
Figure 3.5: Turbulence model comparison

42

a) SA

b) SA_E

c) SST

Figure 3.6. Mach contour and streamlines at inlet throat for a) SA, b) SA_E, c) SST

In Figure 3.6, a comparison is taken with the distribution of Mach number and streamlines in the throat region. Separation region at the throat can be seen in the figure. It begins at an earlier position than other models in the analysis performed using the SST turbulence model. However, it occurs in nearly the same region for SA and SA_E turbulence models. Since the separation is obtained in different locations, different flow behaviors in the isolator arise. This is the primary source of the difference between the SST and the others.

Idris et al. give experimental schlieren image in the reference study [43]. This schlieren image is compared with the gradients of the density field obtained from SU2 analysis using SA_E turbulence model. (Figure 3.7). The flow phenomena observed in the experiment such as cowl tip shock, separation shock, reattachment shock, etc. are also successfully predicted in the SU2 analysis.
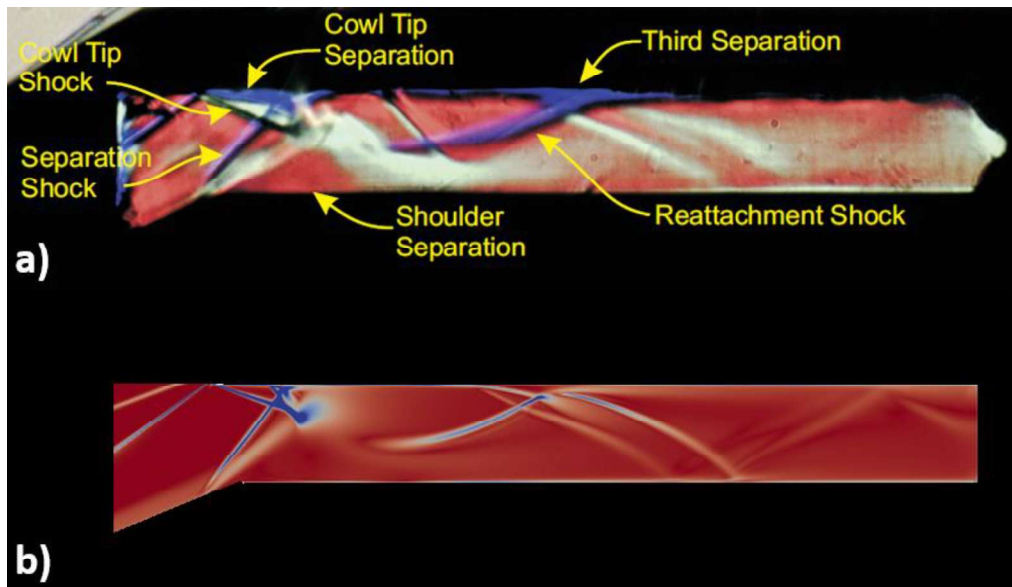
Figure 3.7. a) Experimental schlieren image (modified from [43]), b) The gradients of the density field obtained from SU2 platform

3.1.2. Scramjet Inlet at 6 Mach

In the first verification case, the scramjet geometry used has pressure transducers only on the ramps. Assessments with SU2 using SA and SA_E turbulence models demonstrate that the predictions in this region are successful. These models, however, offer different findings in the isolator region. To ensure that the model used also delivers successful results in the isolator region, it is desired to compare the experimental data obtained using pressure transducers in the isolator with the results of the SU2. Häberle tested SCR02 geometry experimentally [44]. SCR02 is a 2D scramjet inlet. The geometric details of it are given in Figure 3.8. The complete length of the inlet is 920 mm. It has two ramps and a convex shoulder. The deflection angle of the first ramp is 11° and of the second ramp is 14°. There exists a sidewall which starts from the first ramp. The height of the throat is equivalent to 20 mm. Isolator consists of a diverging channel. Pressure on the lower isolator surface is measured using 4 transducers and measured on the upper isolator surface using 5 transducers.
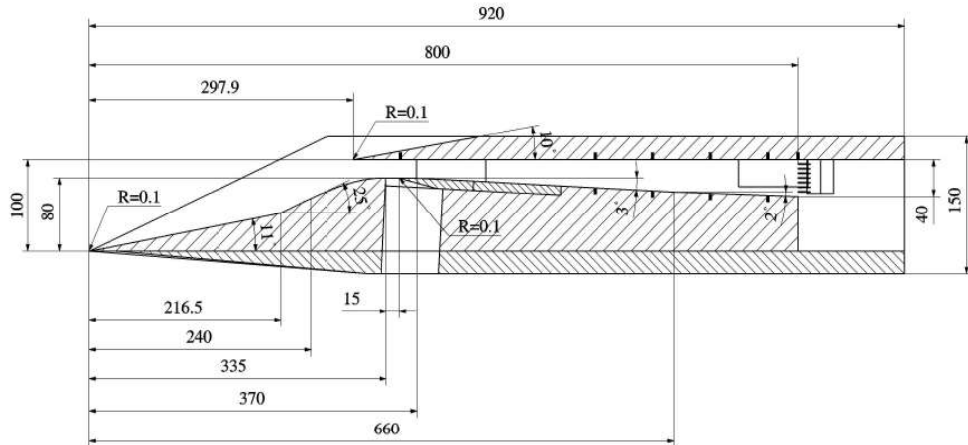
Figure 3.8 Dimensions of SCR02 inlet (Units are in mm) [44]

3.1.2.1. Turbulence Modeling

The results of 3 different turbulence models available in SU2 are compared with experimental data. The experimental data [44] and SU2 results of pressure distribution inside of the isolator for underside and upside are given in Figure 3.9 and Figure 3.10 respectively.
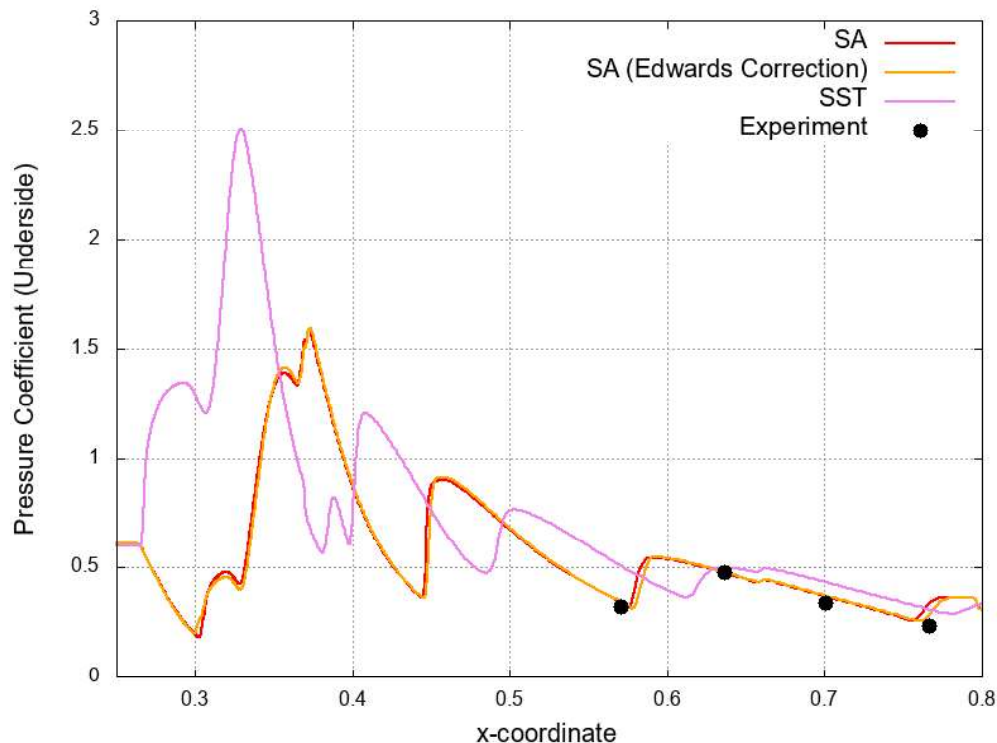
Figure 3.9. Pressure distribution at underside of SCR02 isolator
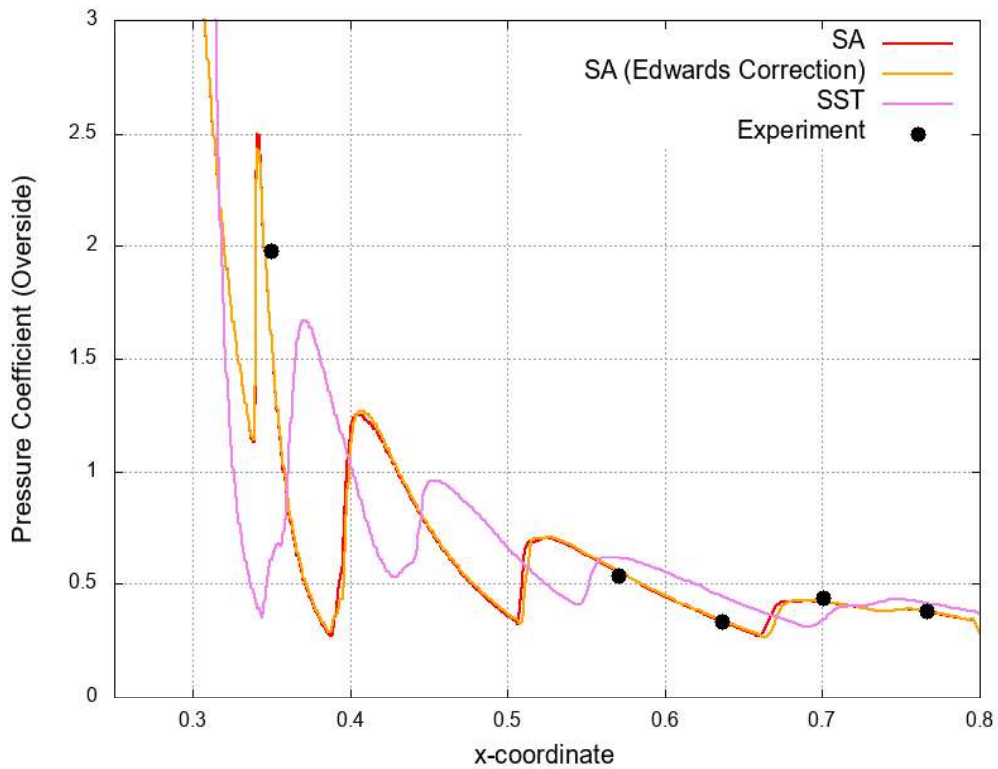
Figure 3.10. Pressure distribution at upside of SCR02 isolator

As in the first verification case, the SST turbulence model results differently from other turbulence models and the experiment. The findings of both SA and SA_E are consistent with the experimental data. The only tiny distinction is that at x = 0.76, the SA_E model is closer to the experiment results than SA.

The reference study has also Mach number measurements at the exit of SCR02 inlet [44]. These experimental Mach values compared with the SU2 analyses. The results are shown in Figure 3.11.
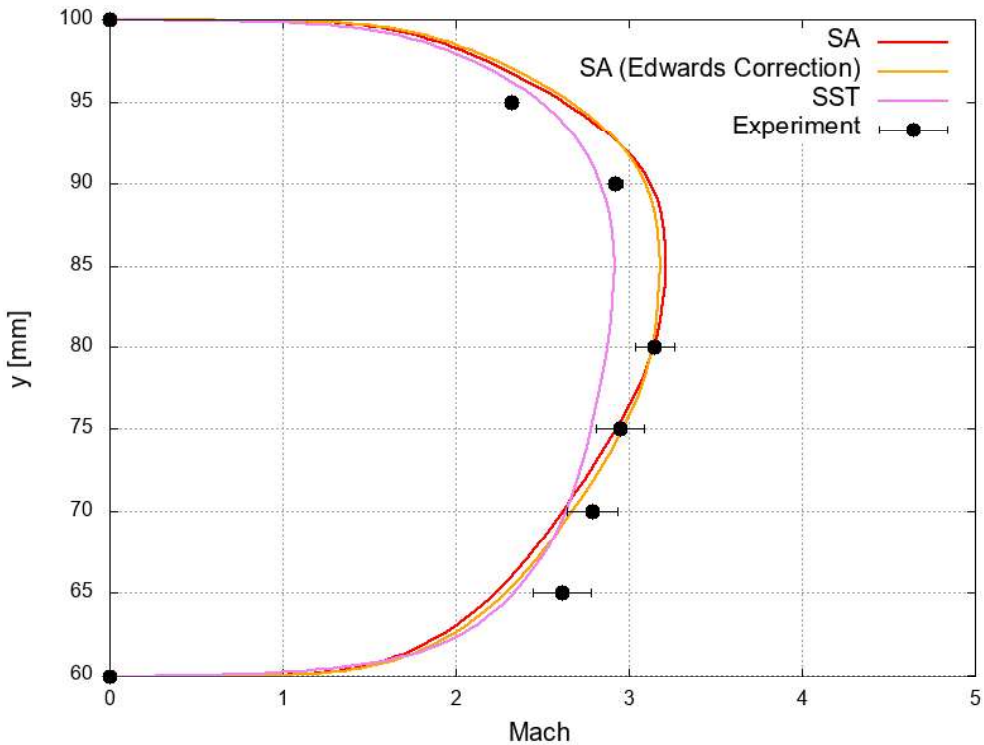
Figure 3.11. Mach number distribution at the exit plane of SCR02

There is a good coherence between the SA and SA_E turbulence model results and the experiment in the Mach number distribution at the exit of SCR02.

In order to compare the boundary layer resolutions of different turbulence models, the velocity profiles at x=0.15 m are plotted in Figure 3.12. The comparison does not include experimental information as there are no relevant experimental data available. The results obtained from the three models are very close to each other for x = 0.15 m.
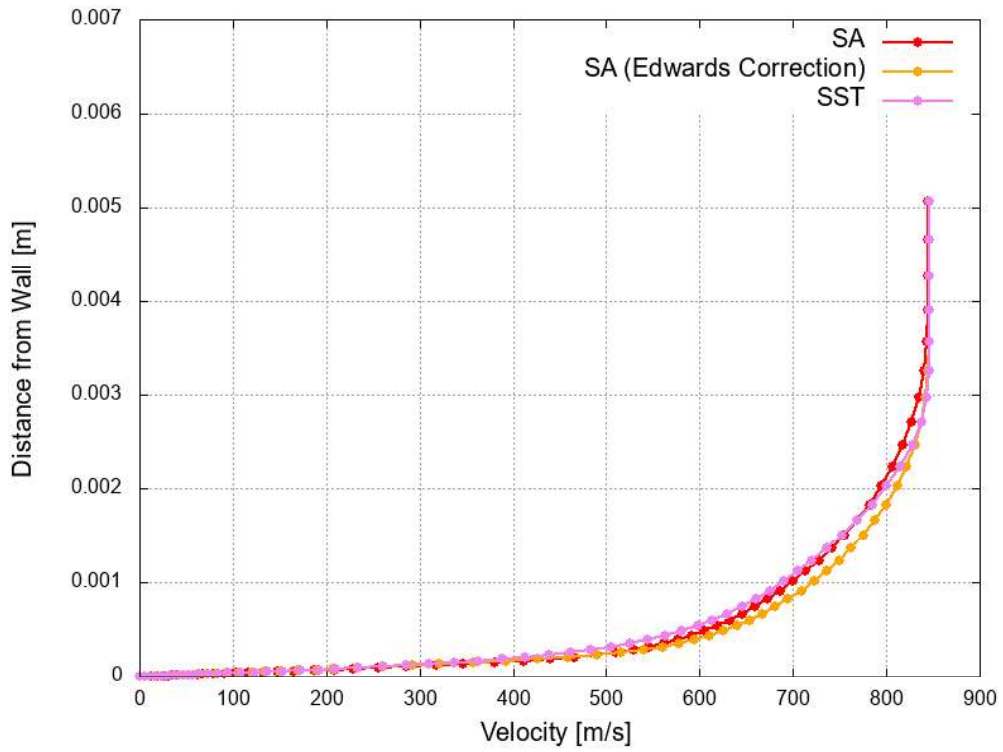
Figure 3.12. Velocity profile in the boundary layer at x=0.15 m

The findings of the two verification studies are criticized together and it is decided to use the SA_E turbulence model to continue the optimization runs.

3.2. Parallel Computations

A parallel efficiency study is performed using SA_E turbulence model for the scramjet inlet in the first verification case. The solution time of 2, 4, 8, 16 and 32 core solutions are compared with the time of serial solution. The speedup curve with parallel efficiency is given in Figure 3.13. Efficiency is maximum at 8 cores, while the maximum speedup occurs at 16 cores.
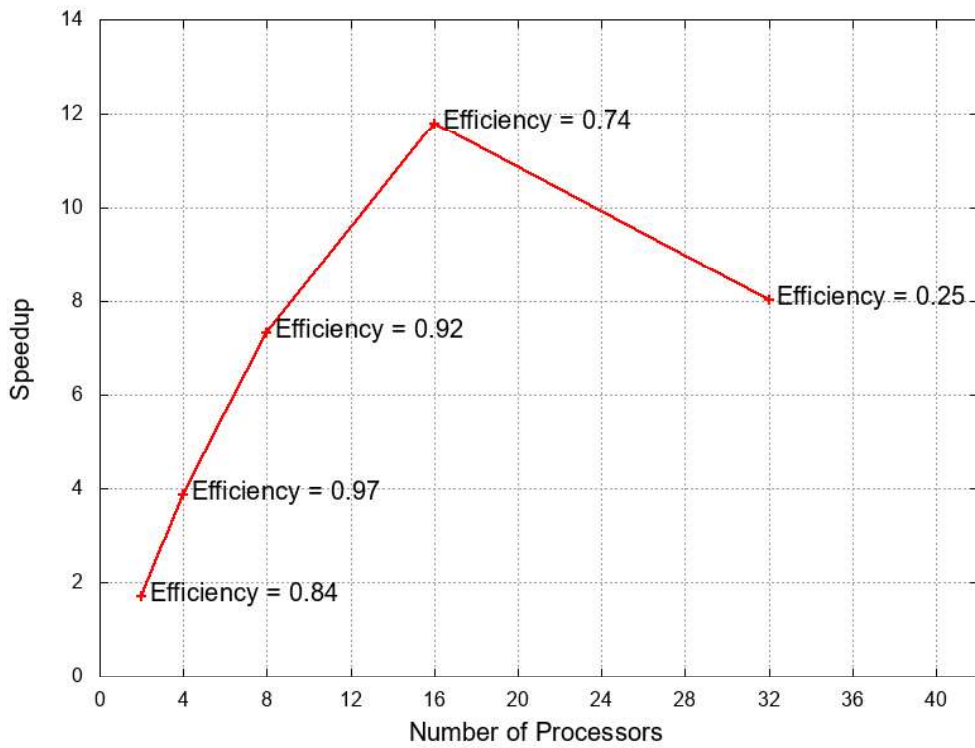
Figure 3.13 Speedups and Efficiencies

3.3. Inviscid Flow Optimizations

Generally, scramjet inlet designs are examined firstly via inviscid simulations in the conceptual design phase. The same strategy is followed in this study, and the optimization process is started with inviscid simulations. Neglecting the viscous effects makes it possible to obtain flow and adjoint solutions much quicker. Thus, the effects of some parameters such as the number and size of the design variables to the optimization process can be assessed faster. When the desired conditions are satisfied in these analyzes, new optimizations which include viscous effects will be performed using the same objectives and constraints.

3.3.1. Optimization Parameters

Since the design point of the hypersonic vehicle is defined as 5 Mach flow at 25 km altitude, freestream temperature and pressure are set to 221.55 K and 2549 Pa

50

respectively. Dynamic pressure is 44.6 kPa in this flight condition which is appropriate for scramjet engines.

The numerical scheme for the convective flux is specified as JST, and the time integration is performed with Euler implicit method. CFL number is adjusted as 5.0, and 2 levels V cycle multigrid option of the SU2 is used in the runs. The convergence criteria are constructed according to residuals. When the magnitude of order of residual reduction is achieved to 5 or minimum residual is achieved to 10^{-8}, convergence is accepted. If these conditions are not met, the flow and adjoint runs are completed when they reach 1000 iterations.
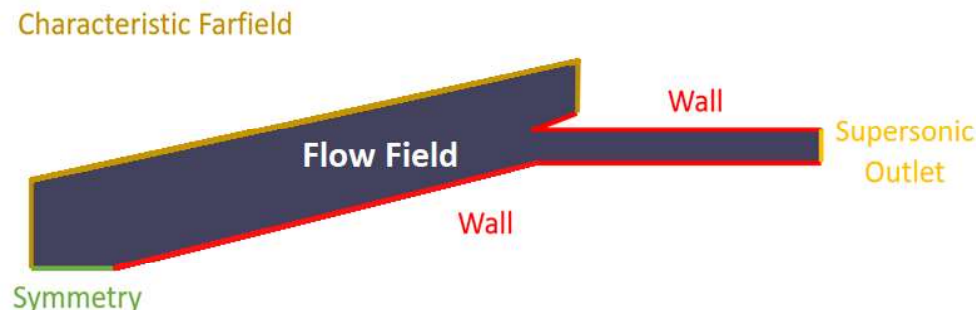
Figure 3.14. Boundary conditions

The boundary conditions are given in Figure 3.14. In the analyzes, four different boundary conditions are used. The surfaces of ramp, isolator, and cowl are specified as inviscid adiabatic wall. The exit of the inlet boundary is defined as a supersonic outlet. The characteristic farfield boundary condition is used for the boundaries represented with brown lines in Figure 3.14. The properties for the farfield boundary condition are taken from the flight conditions given above. The bottom boundary, which lies between the leading edge of the forebody ramp and the left boundary of the flow field, is defined as symmetry in order to keep iterations stable. In the first verification study, a grid-independent solution is obtained. The same physical space is used in the meshes of both inviscid and viscous flow optimizations.

All objective functions, J, and constraint, C, are calculated at the exit of the inlet.

Inviscid flow optimizations are performed by using four different baseline design. The difference between the first two and the last two is the ramp angle. The difference between the first and the second is the cowl lip position. That is the distinction between the third and the fourth. A layout for the inviscid flow optimization runs is given in Table 3.3. The origin is located at the leading edge of the forebody.

Table 3.3. Layout of Inviscid Optimizations

Baseline Name	Ramp Angle	Cowl Lip Position	Optimization Strategy	J	C
Baseline Design 1	11°	x = 594.87 mm y = 0 mm	Unconstrained Single-Objective Total Pressure Optimization	P_{tot}	-
	11°	x = 594.87 mm y = 0 mm	Unconstrained Multi-Objective Optimization	P_{tot} & $\dot{m}$	-
	11°	x = 594.87 mm y = 0 mm	Unconstrained Single-Objective Static Pressure Optimization	P	-
	11°	x = 594.87 mm y = 0 mm	Constrained Multi-Objective Optimization	P_{tot} & $\dot{m}$	P
Baseline Design 2	11°	x = 678.42 mm y = 0 mm	Constrained Multi-Objective Optimization	P_{tot} & $\dot{m}$	P
Baseline Design 3	16.5°	x = 664.83 mm y = 0 mm	Constrained Multi-Objective Optimization	P_{tot} & $\dot{m}$	P
Baseline Design 4	16.5°	x = 700.00 mm y = 0 mm	Constrained Multi-Objective Optimization	P_{tot} & $\dot{m}$	P

3.3.2. Baseline Design 1

The aim of the current study is improving the performance of a single-ramp design in terms of π_c, and $\dot{m}$ at Mach 5 flight condition. An initial geometry is required to perform this task. This initial geometry is designed such that the overall inlet length will be equal to 1.2 m. Also, the first baseline inlet design satisfies the shock-on-lip condition in inviscid Mach 5 flow.
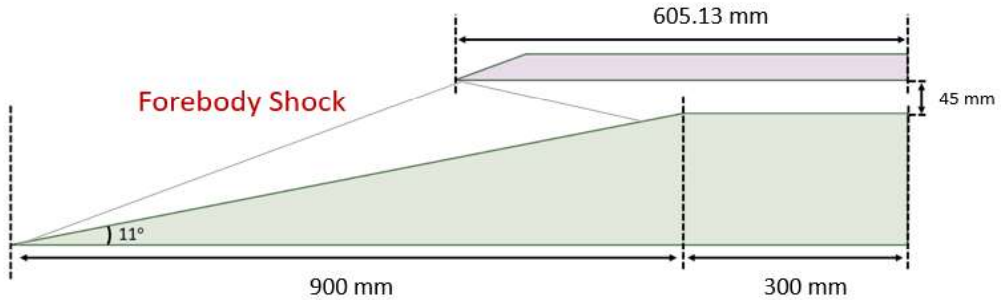
Figure 3.15. Baseline Design 1

The Mach number at the combustion entrance is set to be more than 0.38 times the freestream Mach number in order to prevent the high temperature inside the isolator to cause air dissociation which is another design criterion. The ramp angle is specified as 11°. This angle is smaller than other products in the literature (generally around 20°). This small angle creates the risk of not achieving the required pressure compression ratio for robust combustion. However, since this study aims to achieve a different inlet design than traditional ones and since static pressure is used as a design constraint, it is decided to set this angle for the baseline design in order to create a lower drag. The contraction ratio is fixed to 0.433, which is within the starting limits shown in Figure 1.11. However, in this design shock-on-shoulder condition is neglected to avoid the formation of a high contraction ratio. The resulting scramjet inlet geometry is given in Figure 3.15.

The main purpose of the study is to improve P_{tot} and $\dot{m}$ simultaneously and to use P as a constraint. However, for Baseline Design 1, it is desired to examine the effectivity of the constraint and the different objective functions. For this purpose, 4 different optimization runs are conducted using Baseline Design 1.

3.3.2.1. Unconstrained Single-Objective Total Pressure Optimization

In this optimization run, the aim is maximizing the averaged P_{tot} at the exit of the inlet without a constraint.

Firstly, the effect of the number of design variables on the optimizations is examined. For this purpose, the same analysis is repeated with 16 and 20 design variables. FFD boxes for them are given in Figure 3.16 and Figure 3.17 respectively.
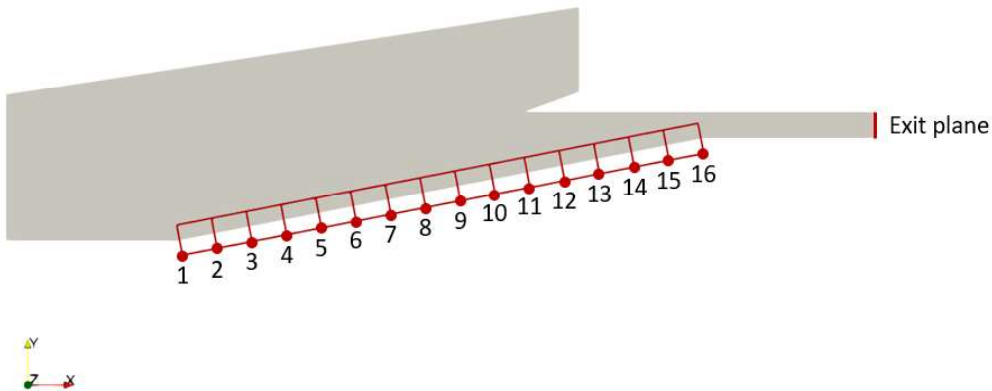
Figure 3.16. FFD Box with 16 design variables
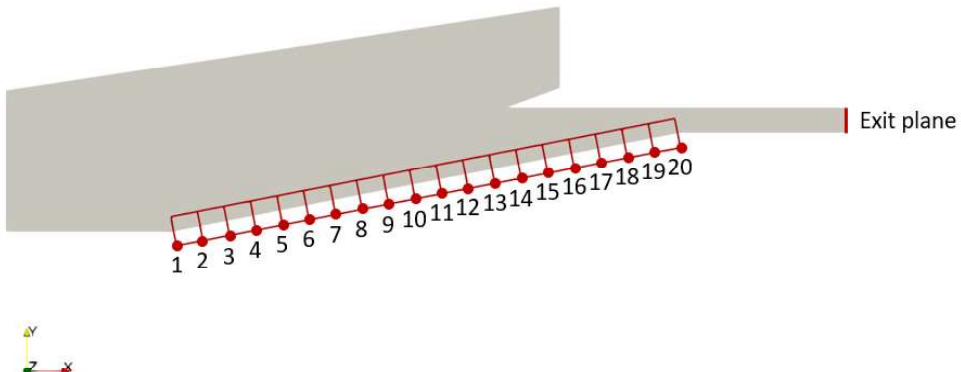
Figure 3.17. FFD Box with 20 design variables
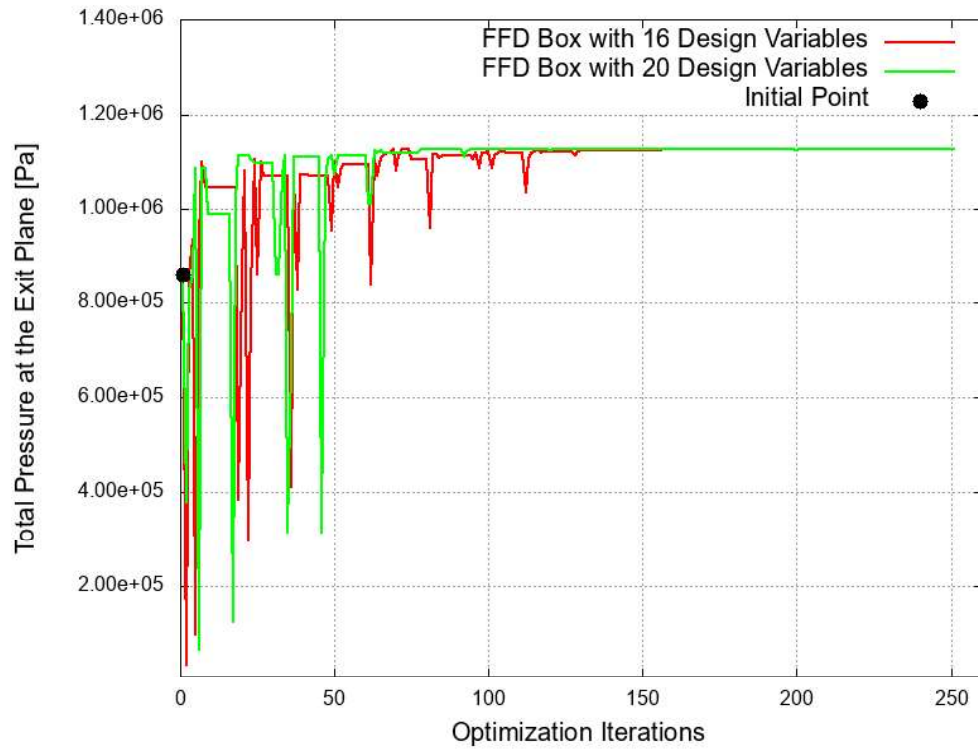
Figure 3.18. The effect of the number of design variables

Both runs converge nearly the same result. The change in the total pressure at the exit of the inlet with optimization iterations is given in Figure 3.18. When the FFD box with 16 design variables is used, there is a 30.66% increase in P_{tot} compared to the baseline design. This increase is 30.9% for FFD box with 20 design variables. There is no significant difference between the two runs in terms of P_{tot} raise, but there is a significant difference in the number of iterations. The optimization study carried out with 16 design variables converged in 156 steps while the other converged in 251 steps. Therefore, the FFD box with 16 design variables is used in all other optimization runs.
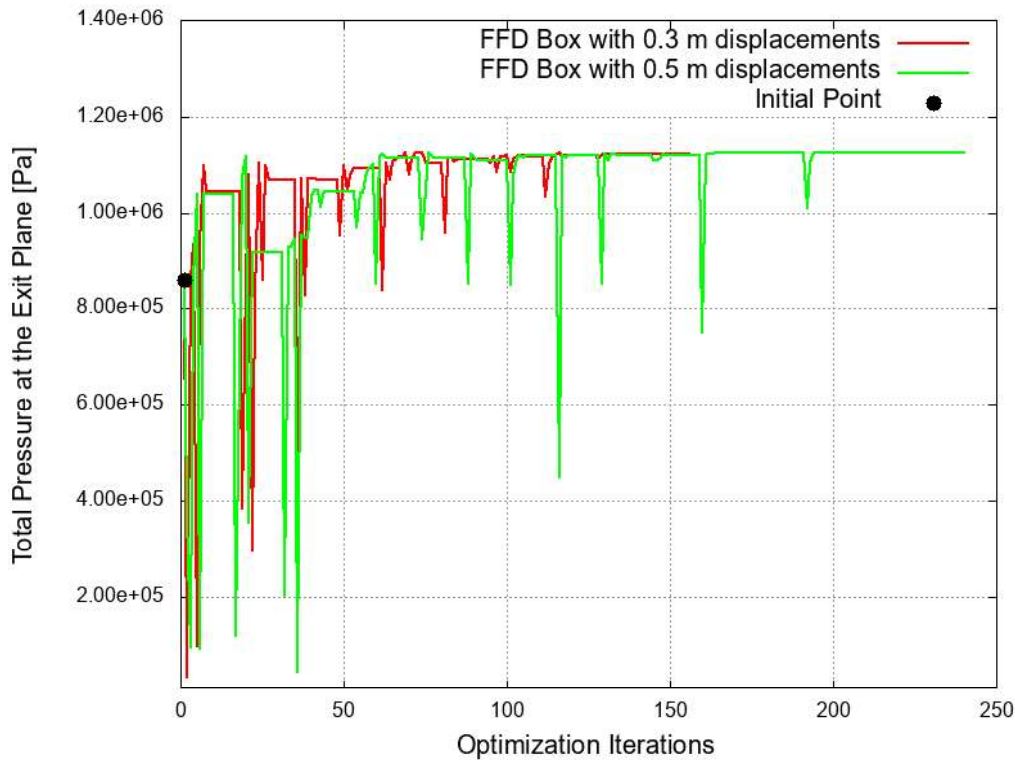
Figure 3.19. The effect of displacement size input for FFD box

FFD box strategy in SU2 needs to the direction of displacement and the size of displacement for the control points. In this study, the control points on the FFD box are adjusted so that they can only move up and down. The amount of displacement to the right and left is fixed to 0. For the upward and downward shifts, both 0.5 m and 0.3 m inputs are given to the software and two different optimizations are performed with these inputs. The findings of these optimization runs are given in Figure 3.19. Both runs converge nearly the same result. P_{tot} increases 30.92% with respect to baseline design when the FFD box with 0.5 m displacement input is used. It is 30.66% for 0.3 m displacement input. The difference between the two runs is quite small. However, the number of iterations of these runs are completely different. The optimization study conducted with 0.3 m displacement input converged in 156 steps while the other converged in 240 steps. This input can be thought of as design space. Since optimum geometry is obtained with less than 0.3 meters of variation at the

56

control points on the ramp, it is logical that both analyzes converge to the same result. For the other optimization runs, this input is defined as 0.3 m.
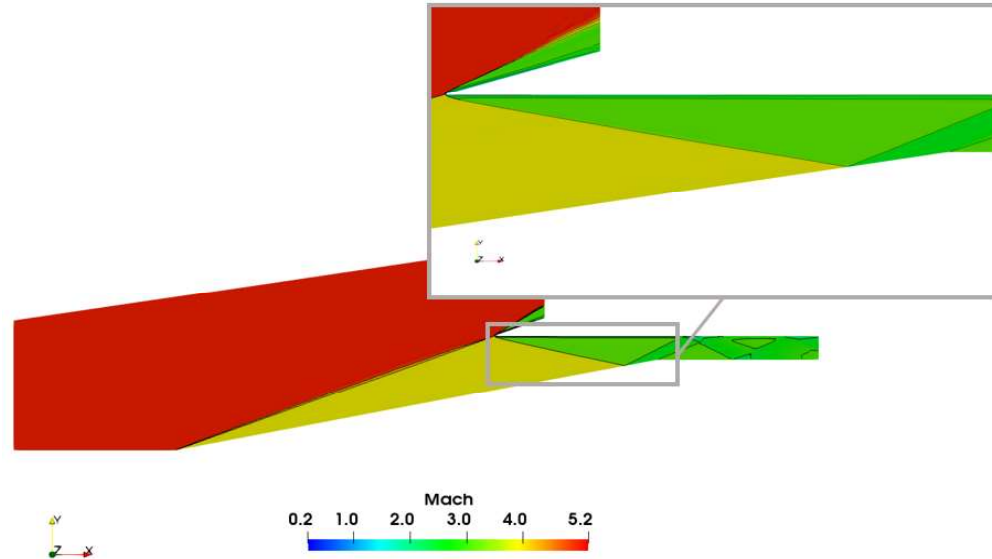
Figure 3.20. Mach contour for Baseline Design 1
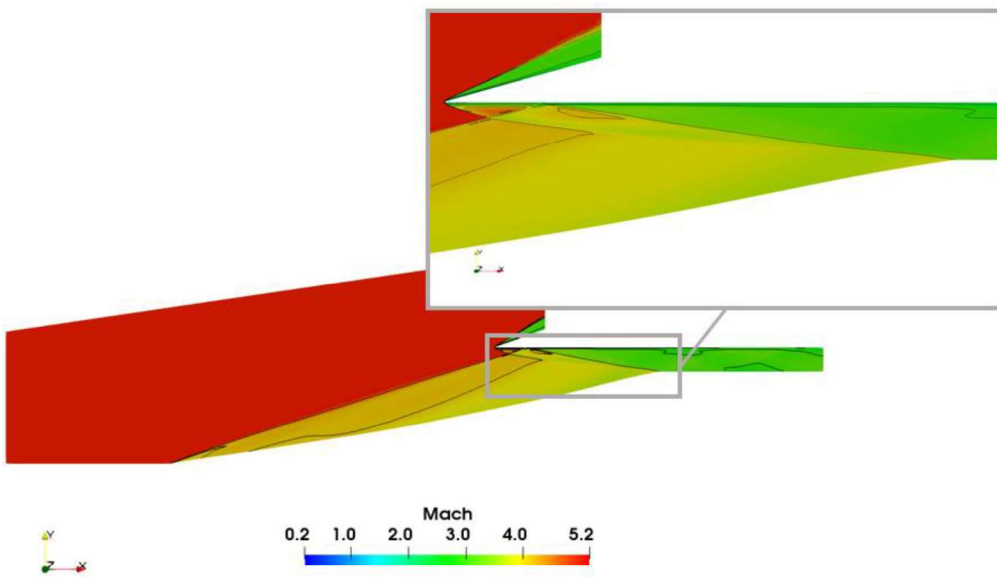
Figure 3.21. Mach contour for the optimized geometry (Unconstrained Single-Objective Total Pressure Optimization)

When the FFD box with 16 design variables and 0.3 m displacement input is the case, the convergence is obtained by performing 156 direct flow and 30 adjoint solutions for the unconstrained optimization run to maximize P_{tot}.

Mach contours for the baseline and the optimized designs are given in Figure 3.20 and Figure 3.21 respectively.

Figure 3.20 shows that Baseline Design 1 satisfies the shock-on-lip condition at 5 Mach inviscid flow. However, the optimization tool sacrifices the shock-on-lip condition to satisfy shock-on-shoulder condition while P_{tot} is maximizing (Figure 3.21).

Pressure contours for the baseline and the optimized geometry are given in Figure 3.22 and Figure 3.23 respectively. According to these figures, the shock pattern inside of the isolator completely changes after optimization.
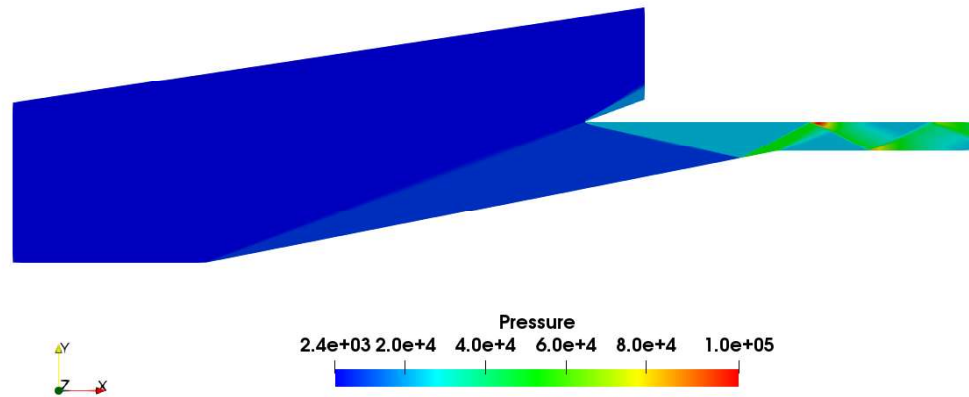
Figure 3.22. Pressure contour for Baseline Design 1
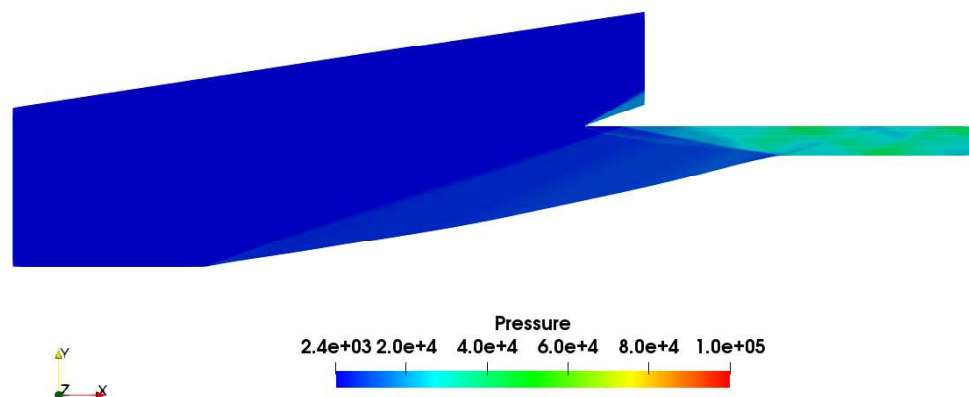
Figure 3.23. Pressure contour for the optimized geometry (Unconstrained Single-Objective Total Pressure Optimization)

Temperature contours for the baseline and the optimized design are given in Figure 3.24 and Figure 3.25 respectively.
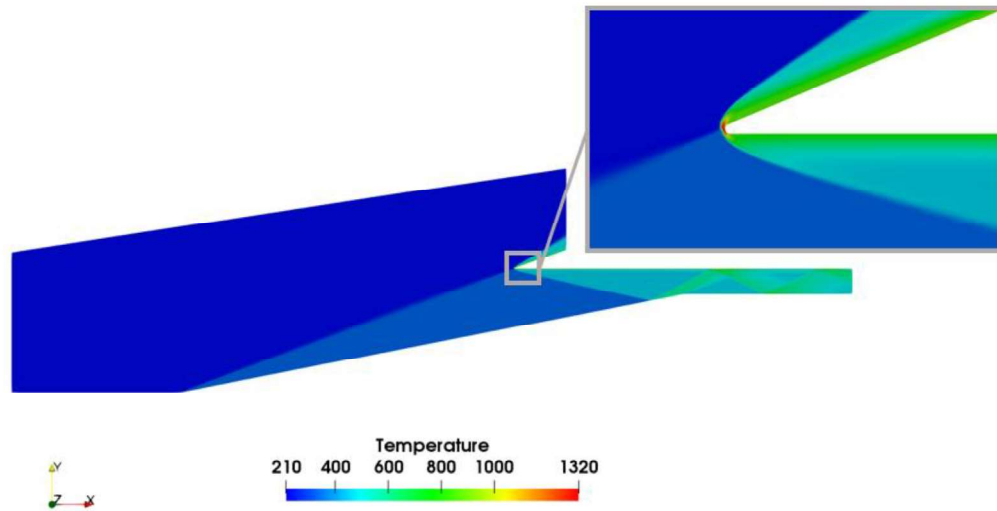
Figure 3.24. Temperature contour for the Baseline Design 1
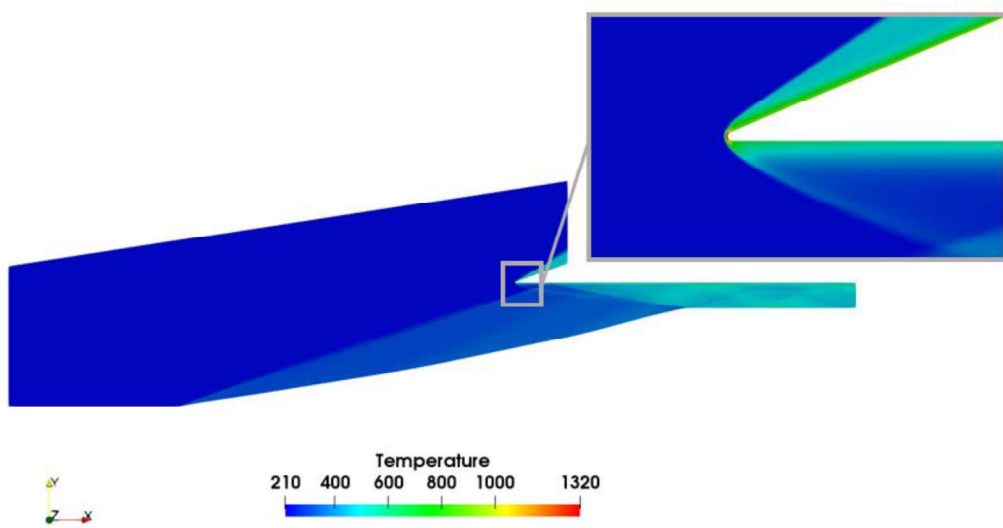
Figure 3.25. Temperature contour for the optimized geometry (Unconstrained Single-Objective Total Pressure Optimization)

Maximum temperatures occurring on the cow lip are around 1320 K for both baseline and optimized inlet. Although the temperature distribution patterns are not the same for two inlets, the temperature ranges are the same in both flow fields.

The change in the ramp surface is illustrated in Figure 3.26. Since the first and last control points of the FFD box are kept constant, there is no change in these regions. However, there is a downward shift in the middle of the ramp. At the end of the optimization, a convex-like ramp geometry is obtained.
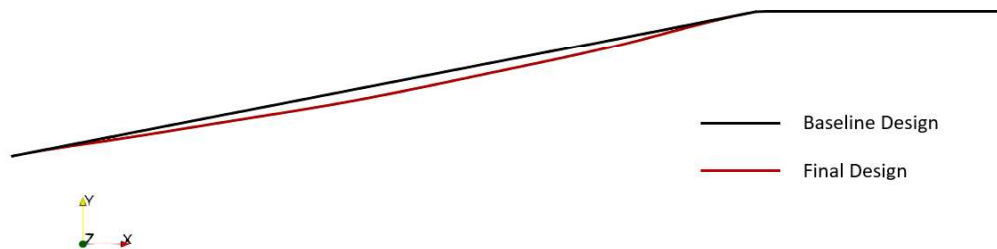
Figure 3.26. The change in the ramp surface (Unconstrained Single-Objective Total Pressure Optimization)

The changes in the inlet performance parameters as a result of optimization are summarized in Table 3.4.

Table 3.4. Optimization Summary (Unconstrained Single-Objective Total Pressure Optimization)

	J	C	P_{tot} [Pa]	ΔP_{tot} [%]	P	ΔP [%]	$\dot{m}$ [kg/s]	$\Delta \dot{m}$ [%]
Baseline		-	8.59E5	-	3.84E4	-	13.16	-
Final	P_{tot}	-	1.12E6	**30.66**	3.14E4	**-18.24**	13.18	**0.15**

With the optimization study, P_{tot} at the exit of the inlet is increased by 30%. An increase in $\dot{m}$ of 0.15% is achieved. However, averaged static pressure at the exit surface decreases by 18.24% to 31357.62 Pa.

3.3.2.2. Unconstrained Multi-Objective Optimization

In this case, the objective functions are specified as P_{tot} and $\dot{m}$. The aims are to increase π_c by increasing P_{tot} at the exit plane of the inlet and to increase the thrust by increasing the $\dot{m}$ captured by the engine. No constraint is used in this case.

The changes in P_{tot} at the exit of the inlet and $\dot{m}$ with optimization iterations are given in Figure 3.27.
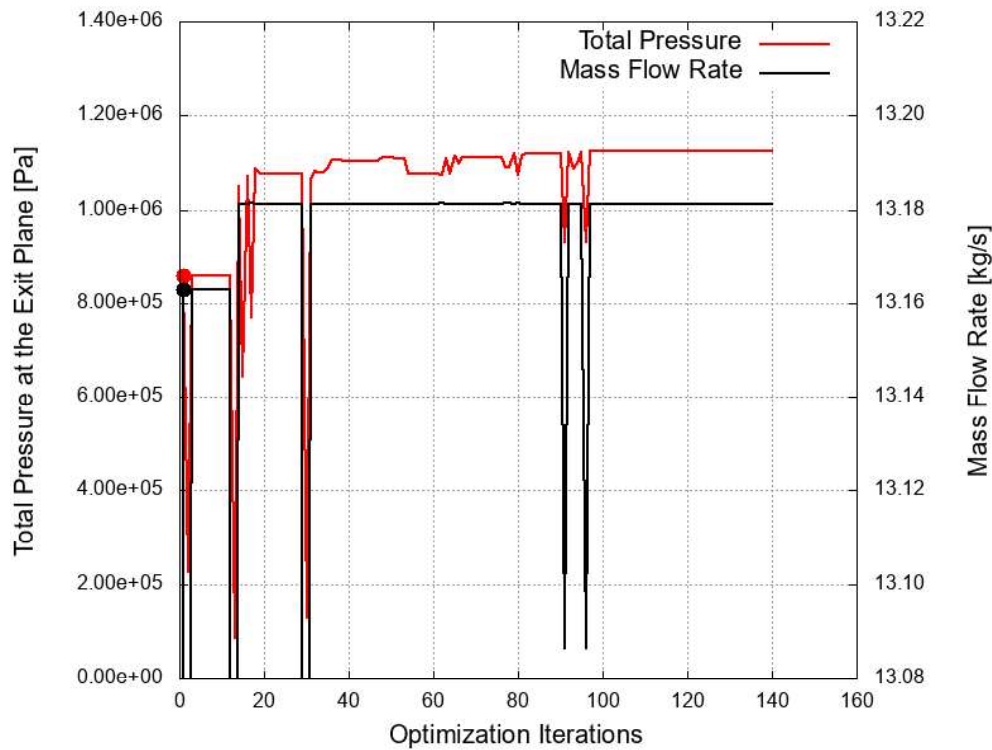
Figure 3.27. Total pressure and mass flow rate variation during the optimization process
(Unconstrained Multi-Objective Optimization)

Convergence is obtained by performing 140 direct flow and 32 adjoint solutions for this run.

Mach, pressure, and temperature contours for the optimized geometry are given in Figure 3.28, Figure 3.29 and Figure 3.30 respectively.
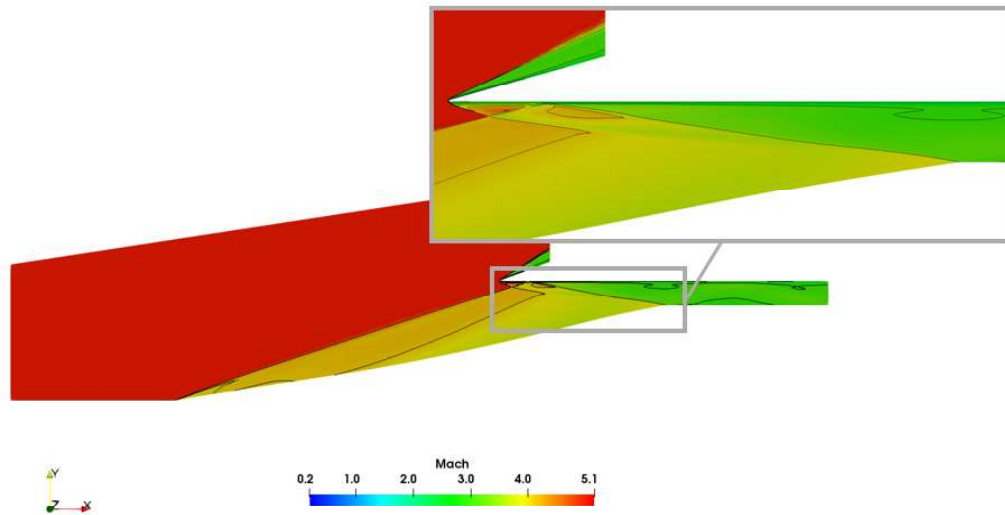
Figure 3.28. Mach contour for the optimized geometry (Unconstrained Multi-Objective Optimization)
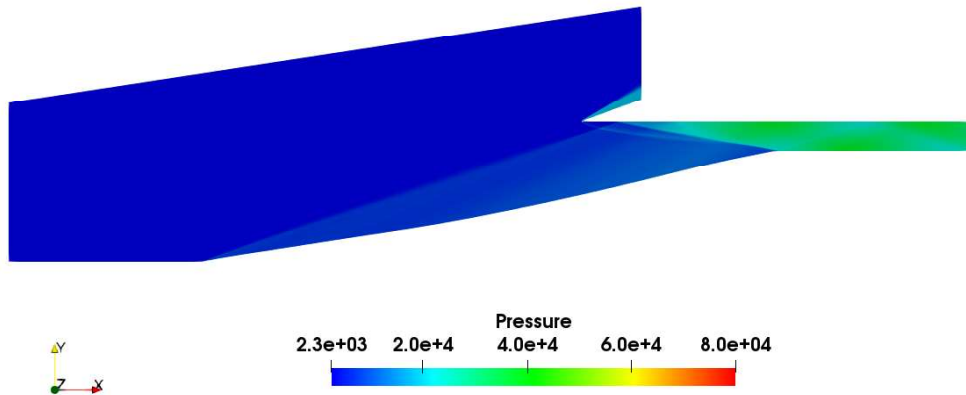
Figure 3.29. Pressure contour for the optimized geometry (Unconstrained Multi-Objective Optimization)
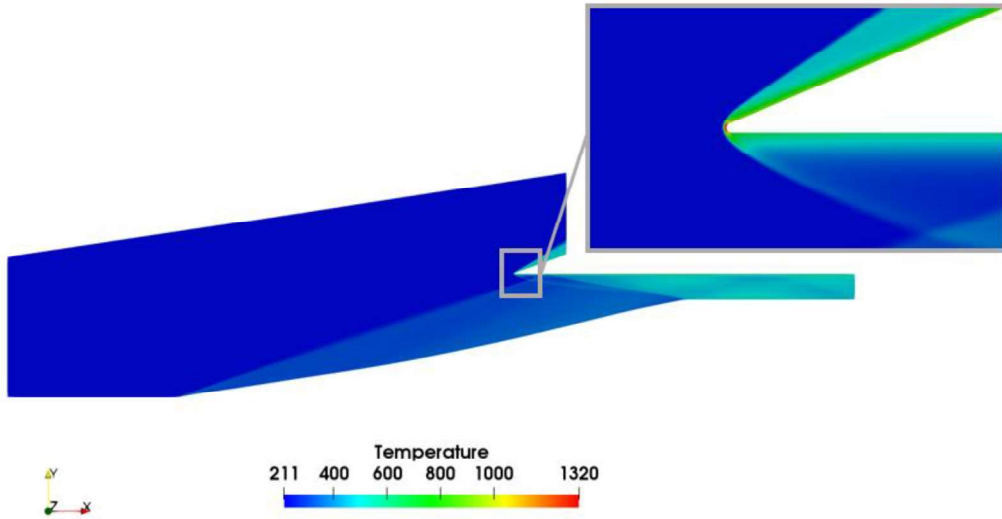
Figure 3.30. Temperature contour for the optimized geometry (Unconstrained Multi-Objective Optimization)

In this run, SU2 waived the shock-on-lip condition and satisfied the shock on shoulder condition as in Section 3.3.2.1.

The comparison of ramp surfaces of baseline and optimized geometry is illustrated in Figure 3.31. In this optimization case, a design similar to the previous one is obtained.
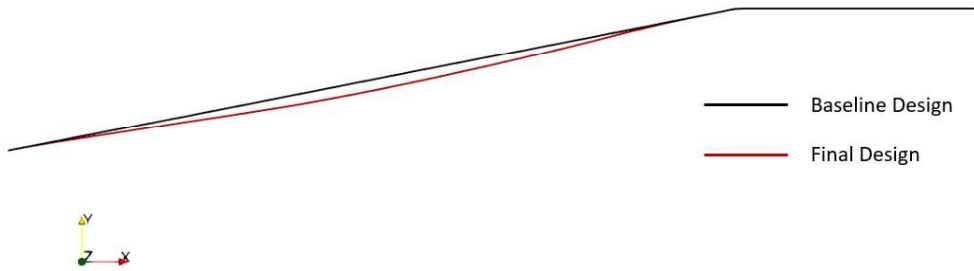
Figure 3.31. The change in the ramp surface (Unconstrained Multi-Objective Optimization)

The changes in the inlet performance parameters as a result of optimization are summarized in Table 3.5.

Table 3.5. Optimization Summary (Unconstrained Multi-Objective Optimization)

	J	C	P_{tot} [Pa]	ΔP_{tot} [%]	P	ΔP [%]	$\dot{m}$ [kg/s]	$\Delta \dot{m}$ [%]
Baseline		-	8.59E5	-	3.84E4	-	13.16	-
Final	P_{tot} & $\dot{m}$	-	1.13E6	**31.09**	3.07E4	**-20.04**	13.18	**0.15**

P_{tot} at the exit of the inlet is increased by 30%, and $\dot{m}$ is increased by 0.15% after the optimization. The increase in total pressure is 0.43% higher than the previous optimization run. Although $\dot{m}$ is not defined as an objective function in the previous one, the same amount of increase in $\dot{m}$ is obtained in these two optimization runs. Like in Section 3.3.2.1, a decrease in static pressure at the outlet of the inlet is observed in this case. It drops by 20% to 30670 Pa.

3.3.2.3. Unconstrained Single-Objective Static Pressure Optimization

The main purpose of a scramjet inlet is to compress the freestream flow and to deliver it to the combustor. Compression level is important for robust combustion. According to the literature, the pressure at the entrance of the combustor should be at least 50 kPa as rule of a thumb. Baseline Design 1 does not meet this requirement. In addition, optimization studies given above caused the static pressure to decrease further. It is therefore intended in this case to raise the static pressure at the exit of the inlet. For this optimization run, no constraint is indicated. The static pressure variation during the optimization is given in Figure 3.32.
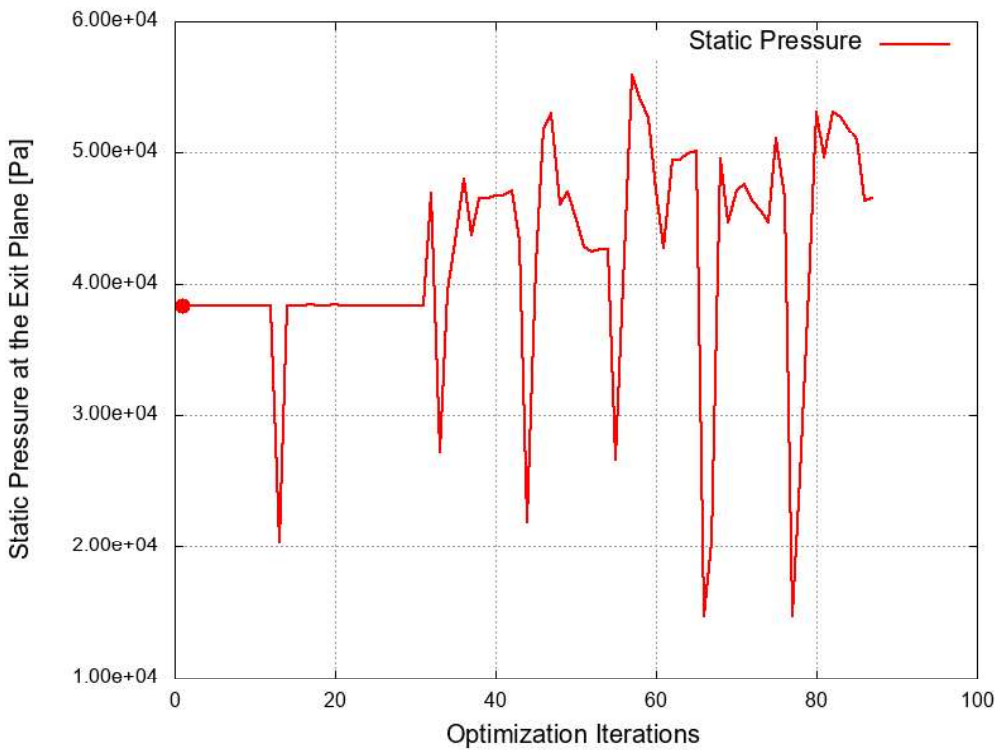
Figure 3.32. Static pressure variation during the optimization process (Unconstrained Single-Objective Static Pressure Optimization)

The convergence criteria are not satisfied for most of the flow and adjoint solutions of this run. The flow and adjoint runs end because they achieve the maximum iteration number. The main reason for this is that the geometries obtained during the optimization process have irregular shapes. This causes the oscillating residuals rather than converging. The abrupt changes in the ramp surface create shocks which increase static pressure at the exit of the inlet. Since the static pressure is defined as the objective function, the tool supports these abrupt changes during the optimization process. Highest static pressure is obtained at 57th design. The Mach contour for this design is given in Figure 3.33.

66
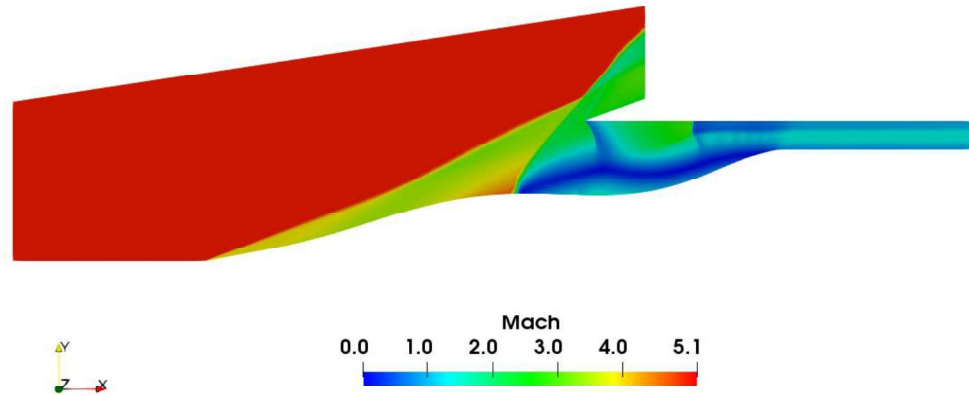
Figure 3.33. Mach contour for the optimized geometry (Unconstrained Single-Objective Static Pressure Optimization)
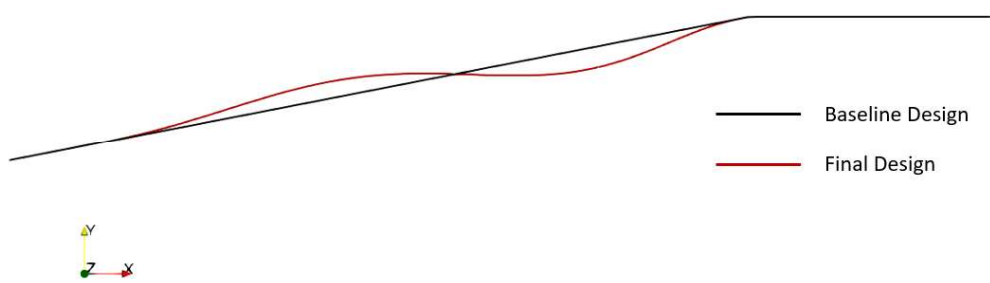
Figure 3.34. The change in the ramp surface (Unconstrained Single-Objective Static Pressure Optimization)

Both shock-on-lip and shock-on shoulder conditions are not satisfied in the optimized geometry (Figure 3.33).

Even when viscous effects are not included, a very complex flow field is created. This design will be completely useless when viscous effects are included. The comparison of ramp surfaces of baseline and optimized geometry is illustrated in Figure 3.34.

Table 3.6. Optimization Summary (Unconstrained Single-Objective Static Pressure Optimization)

	J	C	P_{tot} $[Pa]$	ΔP_{tot} [%]	P	ΔP [%]	$\dot{m}$ $[kg/s]$	$\Delta\dot{m}$ [%]	Drag
Baseline		-	8.59E5	-	3.84E4	-	13.16	-	0.77
Final	P	-	1.37E5	**-84.01**	5.60E4	**45.91**	6.29	**-52.19**	2.53

The changes in the inlet performance parameters as a result of optimization are summarized in Table 3.6. This design increases the static pressure by approximately 46%. However, it causes 84% decrease in P_{tot} at the outlet of the inlet, and a 52% decrease in $\dot{m}$. The final design is extremely inefficient for thrust and total pressure losses. Furthermore, it is seen that the final design has a 3.3 times drag of the baseline. The drag is calculated over the ramp surface only. While computing it, the reference area is used as 0.045 m^2.

3.3.2.4. Constrained Multi-Objective Optimization

A logical design cannot be achieved only when static pressure is defined as the objective function. Therefore, the static pressure is specified as the constraint to the multi-objective optimization performed in Section 3.3.2.2. In the current case, it is aimed that P_{tot} and $\dot{m}$ be maximized, while the static pressure should not fall below 50 kPa.

P_{tot} and $\dot{m}$ change as given in Figure 3.35 during the optimization. The change in static pressure is given in Figure 3.36.
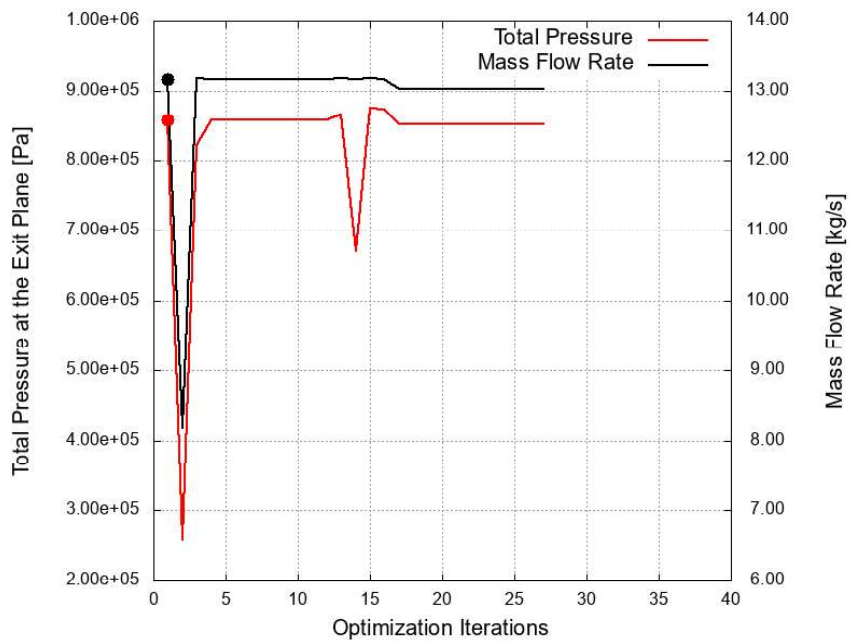
Figure 3.35. Total pressure and mass flow rate variation during the optimization process (Constrained Multi-Objective Optimization)
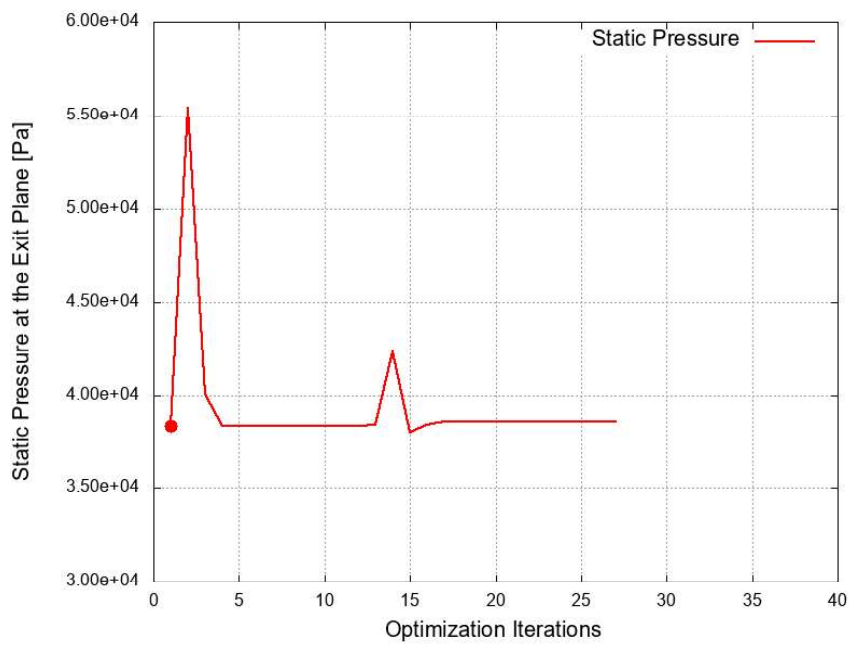

Figure 3.36. Static pressure variation during the optimization process (Constrained Multi-Objective Optimization)

The only case where the static pressure is above 50 kPa is obtained in the 2nd design. However, in this design, $\dot{m}$ and P_{tot} have taken the smallest values in the design process. The best design in terms of $\dot{m}$ and P_{tot} is the 15th design. Mach number, pressure and temperature distributions over the flow field of this design are given in Figure 3.37, Figure 3.38 and Figure 3.39 respectively.
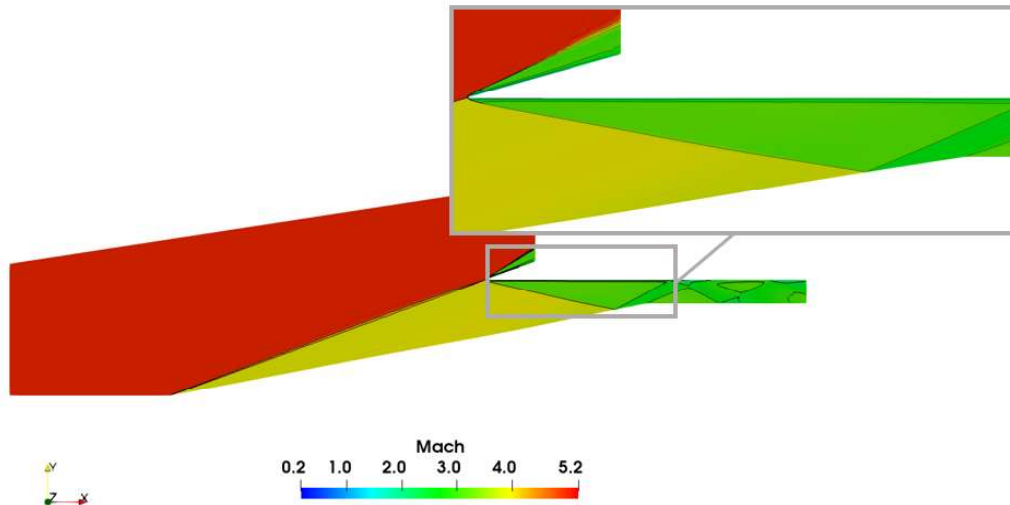
Figure 3.37. Mach contour for the optimized geometry (Constrained Multi-Objective Optimization)
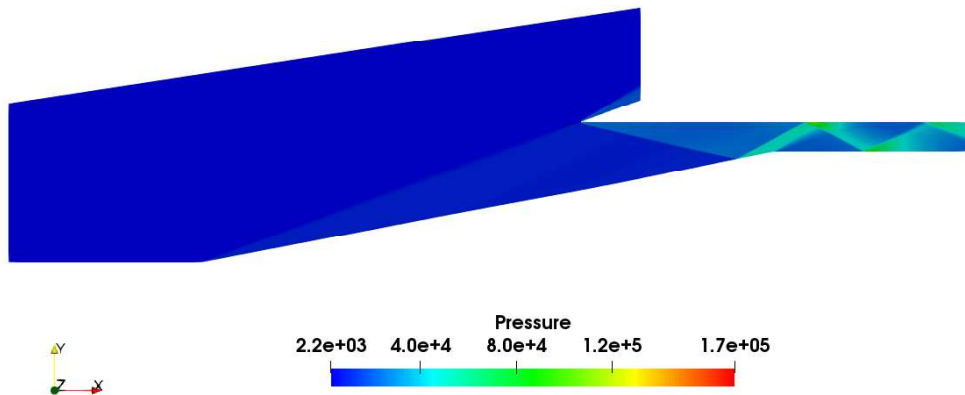
Figure 3.38. Pressure contour for the optimized geometry (Constrained Multi-Objective Optimization)
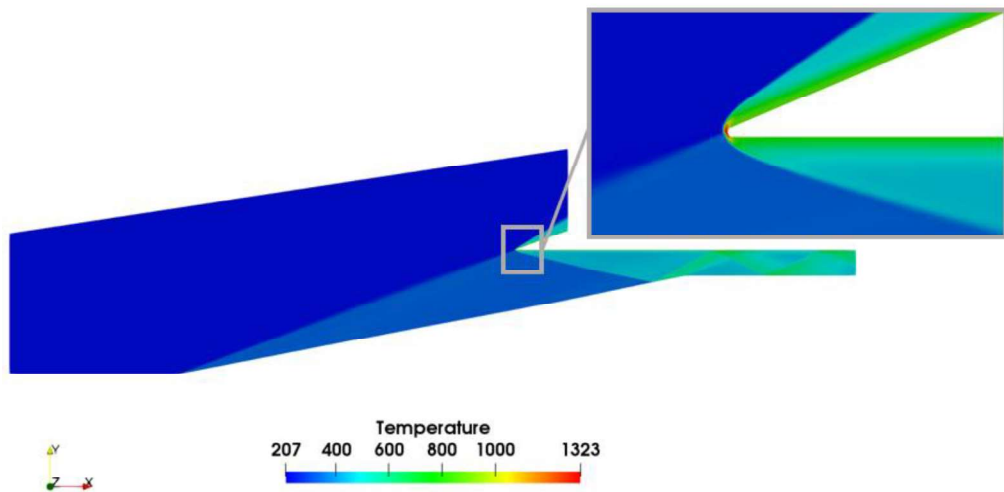
Figure 3.39. Temperature contour for the optimized geometry (Constrained Multi-Objective Optimization)
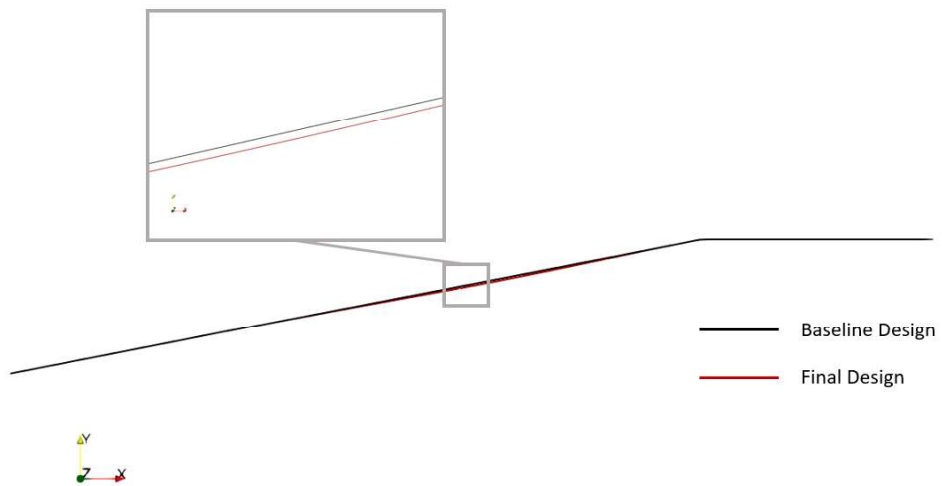
Figure 3.40. The change in the ramp surface (Constrained Multi-Objective Optimization)

When the pressure is set as optimization constraint, the software does not give up shock-on-lip condition to satisfy shock-on-shoulder condition. In this run, the baseline design is tried to be preserved. The difference between the first and the last geometry

is so small that it is invisible. The change in the ramp surface of the optimized geometry is given in Figure 3.40.

Optimization summary of this run is given in Table 3.7.

Table 3.7. Optimization Summary (Constrained Multi-Objective Optimization)

	J	C	P_{tot} $[Pa]$	ΔP_{tot} [%]	P	ΔP [%]	$\dot{m}$ $[kg/s]$	$\Delta\dot{m}$ [%]
Baseline		-	8.59E5	-	3.84E4	-	13.16	-
Final	P_{tot} & $\dot{m}$	P	8.76E5	**1.97**	3.80E4	**-0.87**	13.18	**0.14**

The static pressure constraint reduces the loss of compression which is 20% in Section 3.3.2.2. It is %0.87 in this case. However, averaged static pressure at the exit plane of the inlet is still below the desired level of 50 kPa. In addition, the increase in P_{tot} is limited to 1% for this case. The increase in mass flow rate is around 0.14% as in Section 3.3.2.2.

3.3.2.5. Summary for Baseline Design 1 Optimizations

The comparison of the optimized designs is given in Figure 3.41. Unconstrained single-objective P_{tot} optimization and unconstrained multi-objective optimization produces nearly the same design (red and brown surfaces in Figure 3.41). Since the constraint limits the change of ramp surface, the resulting geometry in constrained case is almost same with baseline (blue and black surfaces in Figure 3.41). Unconstrained single-objective P optimization gives a completely different design from others.
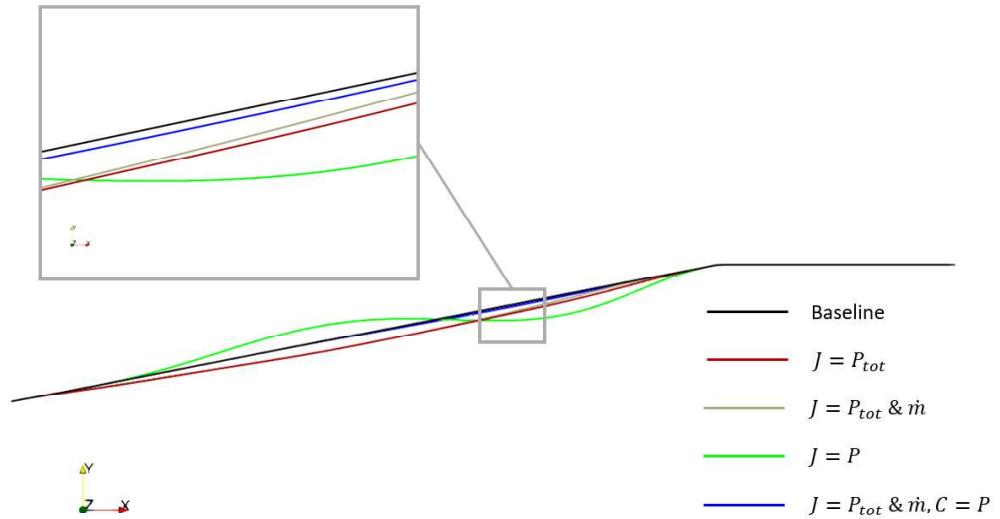
Figure 3.41. Optimized designs comparing different objectives

The results of all optimization studies performed for Baseline Design 1 is summarized in Table 3.8, and the state of the shock-on-lip and the shock-on-shoulder conditions are given in Table 3.9.

Table 3.8. Optimization Results of Baseline Design1

	J	C	P_{tot} [Pa]	ΔP_{tot} [%]	P	ΔP [%]	$\dot{m}$ [kg/s]	$\Delta \dot{m}$ [%]
Baseline	-	-	8.59E6	-	3.84E4	-	13.16	-
Final	P_{tot}	-	1.12E7	30.66	3.14E4	-18.24	13.18	0.15
Final	P_{tot} & $\dot{m}$	-	1.13E7	31.09	3.07E4	-20.04	13.18	0.15
Final	P	-	1.37E6	-84.01	5.60E4	45.91	6.29	-52.19
Final	P_{tot} & $\dot{m}$	P	8.76E6	1.97	3.80E4	-0.87	13.18	0.14

73

Table 3.9. Shock-on-shoulder and shock-on-lip conditions (Baseline Design 1)

	J	C	Shock-on-lip Condition	Shock-on-shoulder Condition
Baseline	-	-	✓	✗
Final	P_{tot}	-	✗	✓
Final	P_{tot} & $\dot{m}$	-	✗	✓
Final	P	-	✗	✗
Final	P_{tot} & $\dot{m}$	P	✓	✗

The highest P_{tot} increase is obtained with the unconstrained multi-objective optimization. Although, the gain is quite low, an increase in $\dot{m}$ is obtained with all optimized designs except unconstrained single-objective static pressure optimization case. In this run, it is decreased by %52.19, while the static pressure at the exit of the inlet is increasing. The compression level drops for other designs. Shock-on-lip and shock-on-shoulder conditions are not satisfied in any design simultaneously

3.3.3. Baseline Design 2

Shock-on-shoulder condition is an important design issue to get a uniform and parallel flow to the surface inside the isolator. However, as mentioned in Section 1.3.3 some designs may not meet this condition since a very high contraction ratio is required to meet it for conventional designs. In order to avoid a high contraction ratio, Baseline Design 1 is also designed not to meet this requirement. On the other hand, optimizations in "Baseline Design 1" part have shown that it is possible to obtain a design that satisfies both shock-on-shoulder and shock-on-lip conditions. By traditional design techniques, accomplishing this task is impossible without changing

the throat area. In order to do that, moving the cowl lip in the Baseline Design 1 is adequate with the design method used in this thesis.

Since the aim is to provide shock-on-shoulder and shock-on-lip conditions at the same time, only the cowl lip position has been shifted in the horizontal direction. The ramp angle of the new baseline is the same with the ramp angle of Baseline Design 1. The optimization strategy of this case is the same within Section 3.3.2.4 (objectives: P_{tot} and $\dot{m}$, constraint: static pressure).

After the constrained multi-objective optimization of Baseline Design 1, shock reflected from the cowl lip hits upstream of the shoulder (Figure 3.37). Since the reflected shock is desired to shift towards the shoulder, the cowl lip position is shifted slightly to the right. If the reflected shock still strikes the upstream of the shoulder, the cowl lip position has been shifted to the right by the same amount; if it hits the downstream of the shoulder, the cowl lip is shifted the left by half of the amount shifted to the right in the previous time. This process is continued until the desired conditions are met. Intermediate steps are excluded from this study. The resulting baseline is given in Figure 3.42.
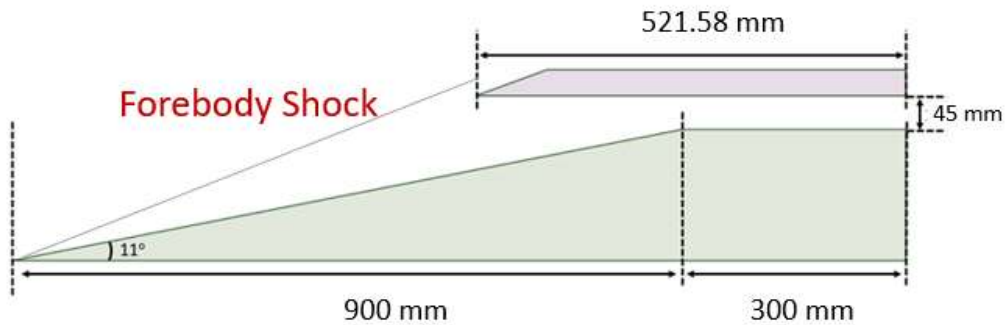
Figure 3.42. Baseline Design 2

Mach number distributions in the flow field of baseline and optimized design are illustrated in Figure 3.43 and Figure 3.44 respectively. While the shock-on-lip and shock-on-shoulder conditions cannot be observed in the baseline, both are satisfied in the optimized design.
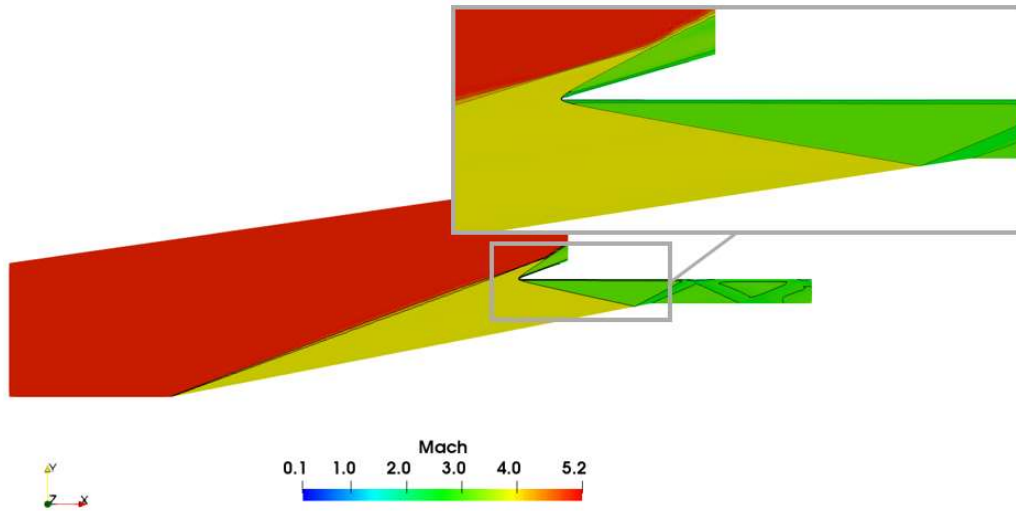

Figure 3.43. Mach contour of Baseline Design 2
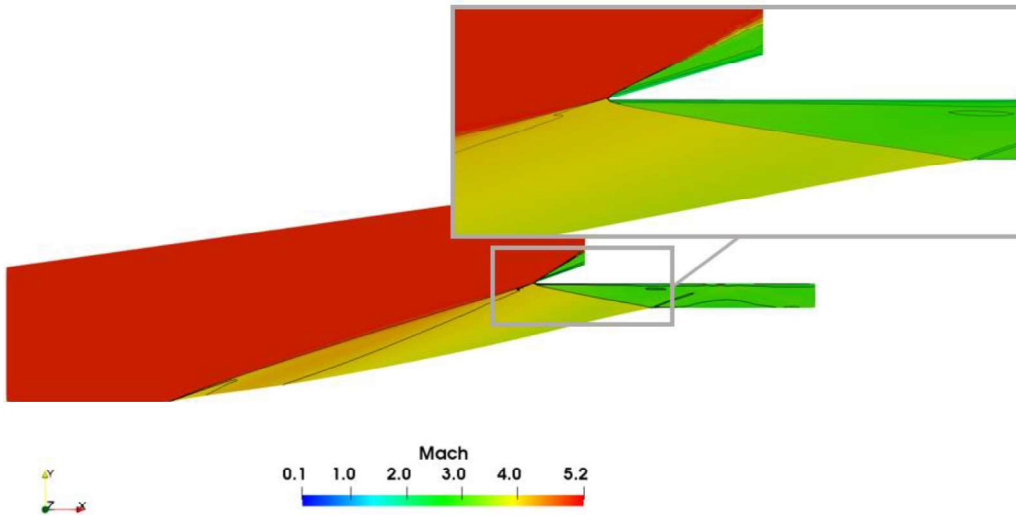
Figure 3.44. Mach contour for optimized design of Baseline Design 2

Pressure and temperature contours are given in Figure 3.45 and Figure 3.46 for the optimized geometry.
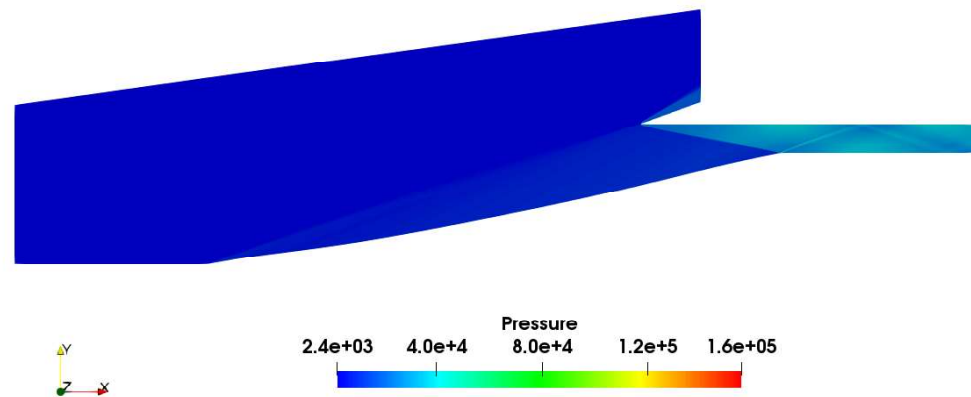

Figure 3.45. Pressure contour for optimized design of Baseline Design 2
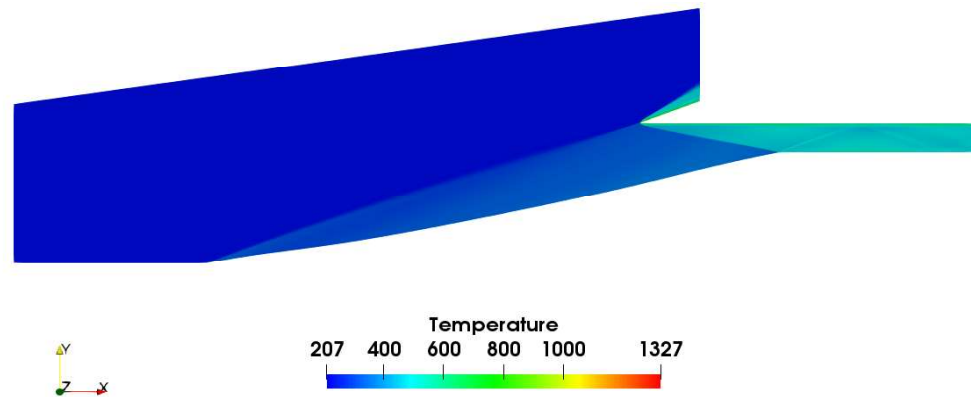
Figure 3.46. Temperature contour for optimized design of Baseline Design 2

Shock train inside of the isolator can be seen from Figure 3.45. The rejected shock from cowl lip hits the shoulder and then it strikes the cowl surface again.

The highest temperature occurs as 1327 K in front of the cowl lip of the optimized inlet which is stagnation point.

The comparison of ramp surfaces of baseline and optimized geometry is illustrated in Figure 3.47. Also, Baseline Design 1, Baseline Design 2 and their optimized versions are compared in Figure 3.48.
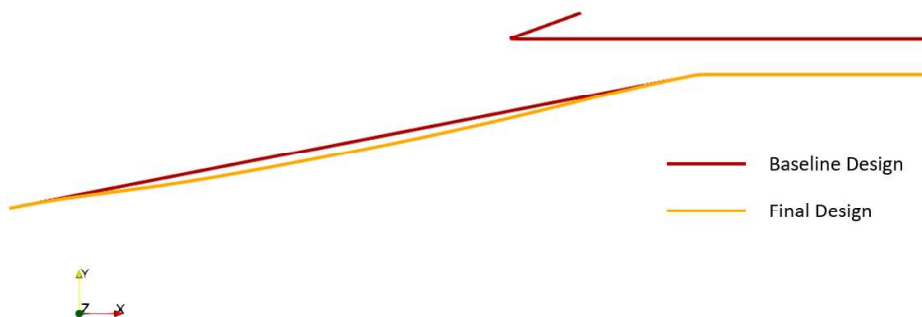
Figure 3.47. The change in the ramp surface of optimized design of Baseline Design 2
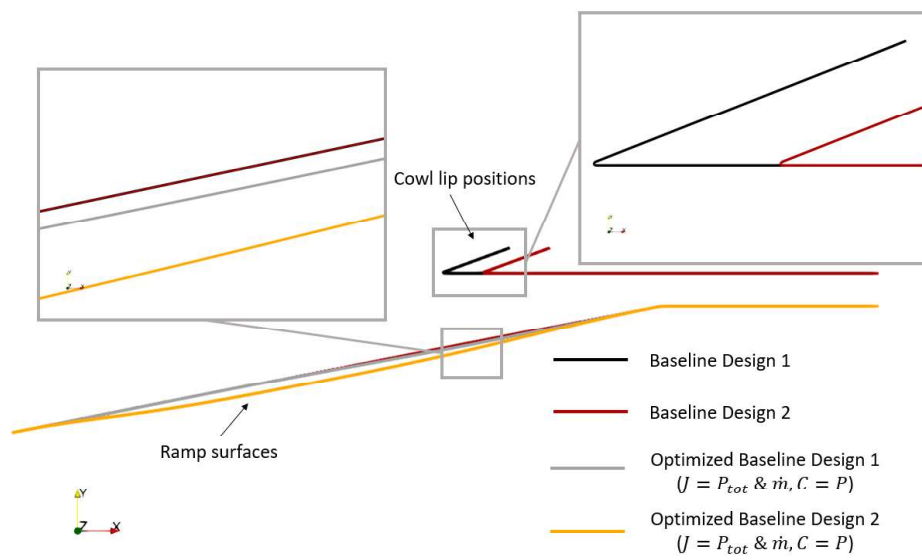
Figure 3.48. Comparison of Baseline Design 1, Baseline Design 2 and their optimized versions

The aim of the optimization is to increase P_{tot} and $\dot{m}$ using static pressure constraint. The value used for the static pressure limitation is 50 kPa. This is the same strategy as in Section 3.3.2.4. Some performance parameters of Baseline Design 1, Baseline Design 2 and their optimized versions are summarized in Table 3.10. Also, Table 3.11 shows the circumstances of shock-on-lip and shock-on-shoulder conditions for these inlets.

Table 3.10. Performance Parameters of Baseline Design 1 (BD1), Baseline Design 2 (BD2) and their optimized versions

	J	C	P_{tot} [Pa]	ΔP_{tot} [%]	P	ΔP [%]	$\dot{m}$ [kg/s]	$\Delta \dot{m}$ [%]
BD1	-	-	8.59E5	-	3.84E4	-	13.16	-
Optimized of BD1	P_{tot} & $\dot{m}$	P	8.76E5	**1.97**	3.80E4	**-0.87**	13.18	**0.14**
BD2	-	-	8.59E5	-	3.46E4	-	13.18	-
Optimized of BD2	P_{tot} & $\dot{m}$	P	1.05E6	**22.29**	3.02E4	**-21.05**	12.66	**-3.84**

Table 3.11. Shock-on-shoulder and shock-on-lip conditions for Baseline Design 1 (BD1), Baseline Design 2 (BD2) and their optimized versions

	J	C	Shock-on-lip Condition	Shock-on-shoulder Condition
BD1	-	-	✓	✗
Optimized of BD1	P_{tot} & $\dot{m}$	P	✗	✓
BD2	-	-	✗	✗
Optimized of BD2	P_{tot} & $\dot{m}$	P	✓	✓

Both optimization runs lead to an increase in P_{tot}. This result indicates that there is a connection between the P_{tot} level and shock-on-shoulder condition because a rise in P_{tot} at the exit surface takes place when it is satisfied. The optimization runs cause a decrease in compression level although they have limitation for the static pressure. $\dot{m}$ increases in the case of optimization of Baseline Design 1, but there is a decrease in the optimized version of Baseline Design 2. Only in the improved version of Baseline Design 2, shock-on-shoulder and shock-on-lip conditions are met simultaneously. This case reveals that it is possible to obtain a design such that shock-on-shoulder and shock-on lip-conditions are satisfied at the same time without increasing throat area by using adjoint-based optimization.

The static pressure at the exit plane of the inlet cannot exceed 50 kPa in any of the Baseline Design 1 and Baseline Design 2 studies. This makes the scramjet inlet impossible to perform its main task. This is because the ramp angle in the baseline designs is relatively small (11°). It should be increased further to reach the required pressure level. Therefore, it is decided to design a new baseline geometry. There is no need to perform RANS simulations for the baseline designs 1 and 2.

3.3.4. Baseline Design 3

The design of the current baseline takes into account the same design issues indicated in Baseline Design 1. The only difference is that the angle of the ramp is 16.5° for the new one. The resulting scramjet inlet geometry is given in Figure 3.49.

Optimization of this design aims to enhance averaged P_{tot} at the exit plane and $\dot{m}$ simultaneously, while providing the required compression level. Therefore, the objectives are P_{tot} and $\dot{m}$, the constraint is static pressure for this optimization case. The critical level for the static pressure is specified as 50 kPa.
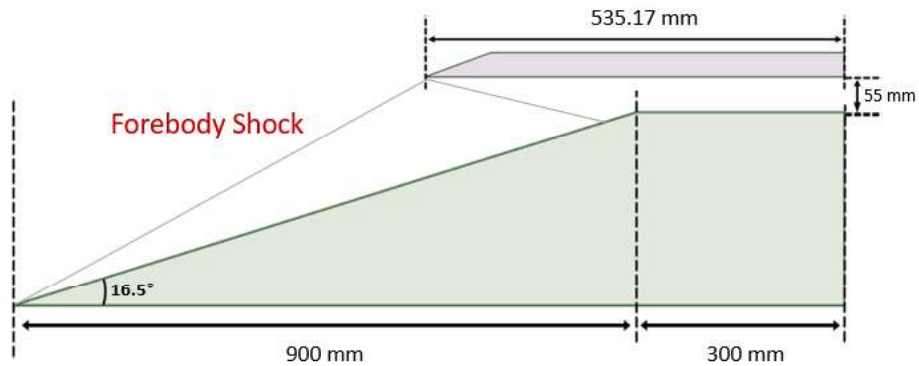
Figure 3.49. Baseline Design 3
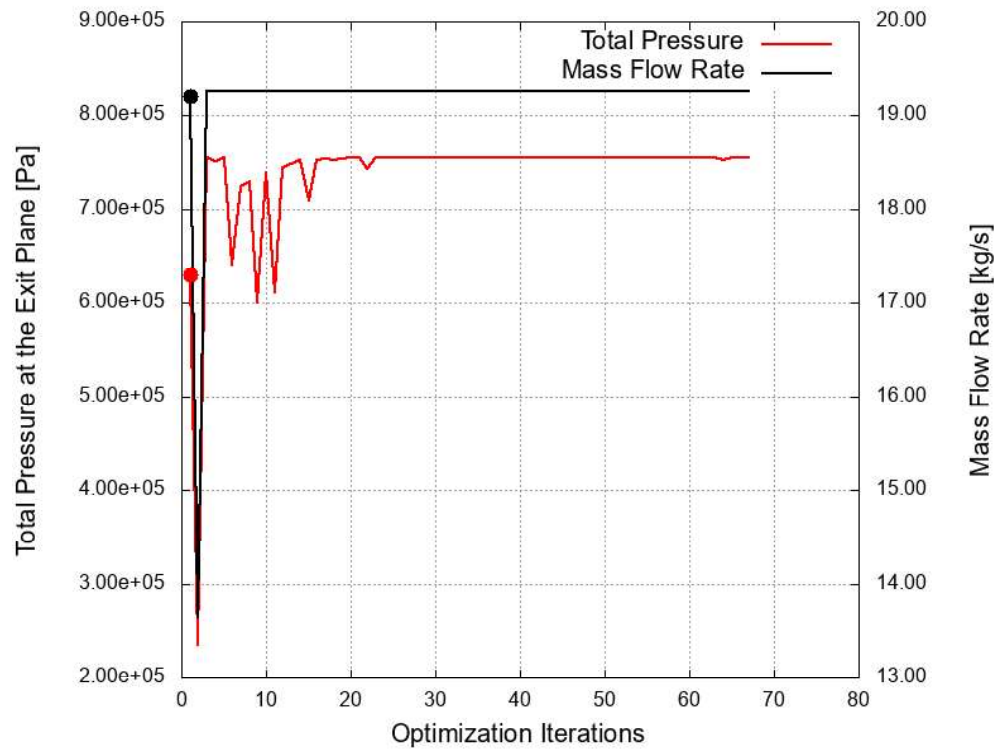
Figure 3.50. Total pressure and mass flow rate variation during the optimization of Baseline Design 3
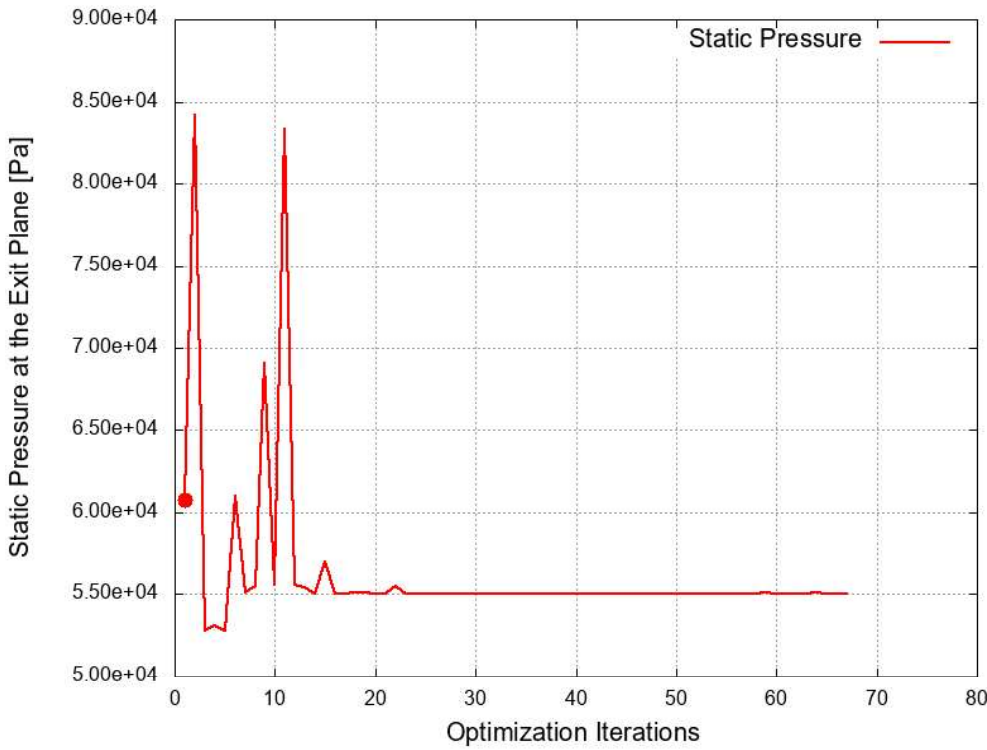
Figure 3.51. Static pressure variation during the optimization of Baseline Design 3

The change in P_{tot} and $\dot{m}$ during the optimization process and static pressure is provided in Figure 3.50. Also, the variation of static pressure is presented in Figure 3.51.

All designs produced by SU2 during the optimization process have static pressure higher than 50 kPa at the exit plane of the inlet. The best design is obtained at 67th iteration in terms of P_{tot} and $\dot{m}$.

Mach number distributions for baseline and optimized geometry flow fields are given in Figure 3.52 and Figure 3.53 respectively. As in previous cases, the tool sacrifices the shock-on-lip condition to provide shock-on-shoulder condition. This finding supports the idea that there is a connection between the shock-on-shoulder condition and P_{tot} level.
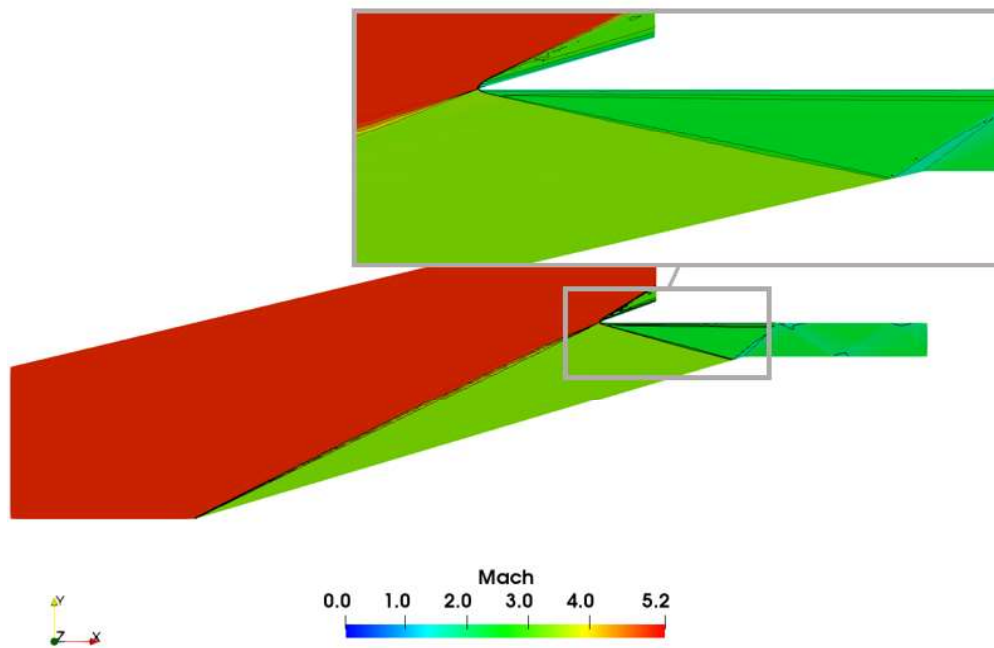
Figure 3.52. Mach contour for Baseline Design 3
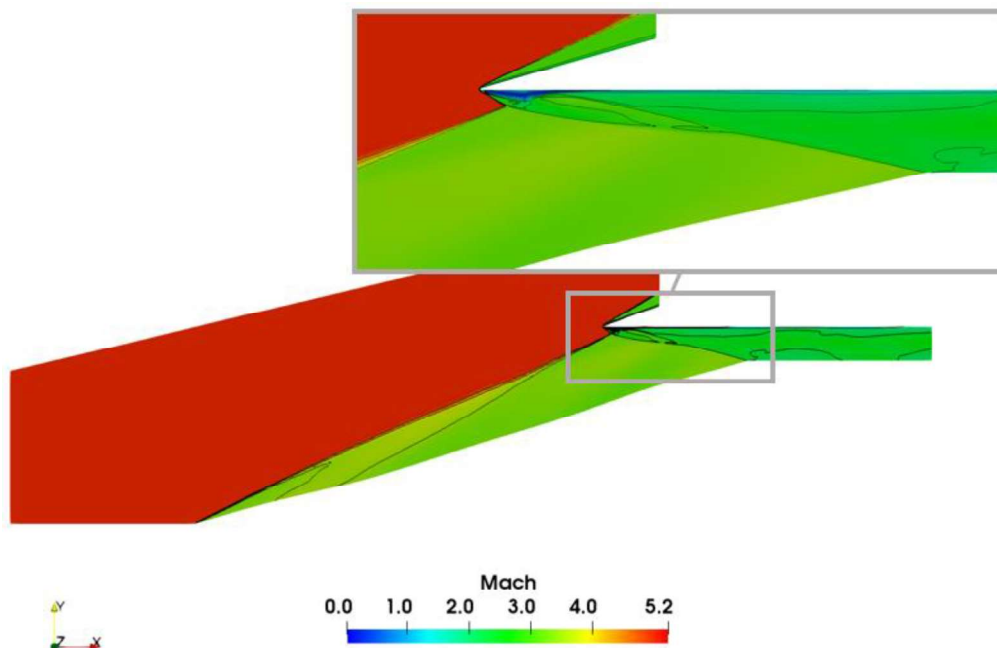
Figure 3.53. Mach contour for optimized geometry of Baseline Design 3

Pressure contour for the baseline and optimized geometry are given in Figure 3.54 and Figure 3.55 respectively. According to these figures, optimization affects the shock pattern inside of the isolator.
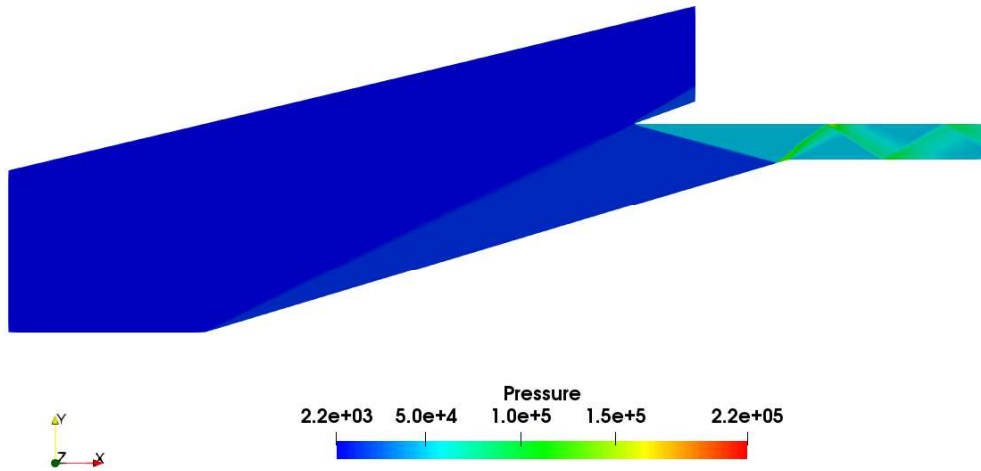
Figure 3.54. Pressure contour for the Baseline Design 3
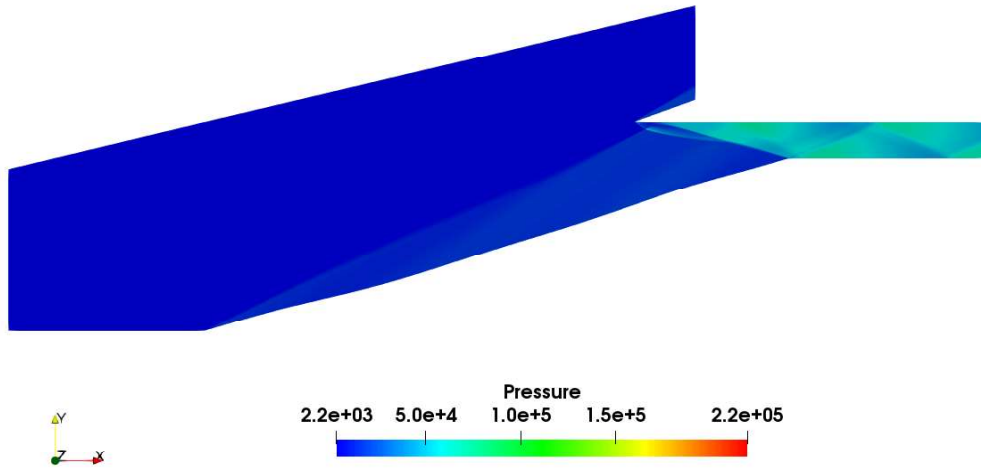

Figure 3.55. Pressure contour for optimized geometry of Baseline Design 3

Temperature contours for the baseline and optimized geometry are given in Figure 3.56 and Figure 3.57 respectively. The temperature ranges are the same in both flow fields.
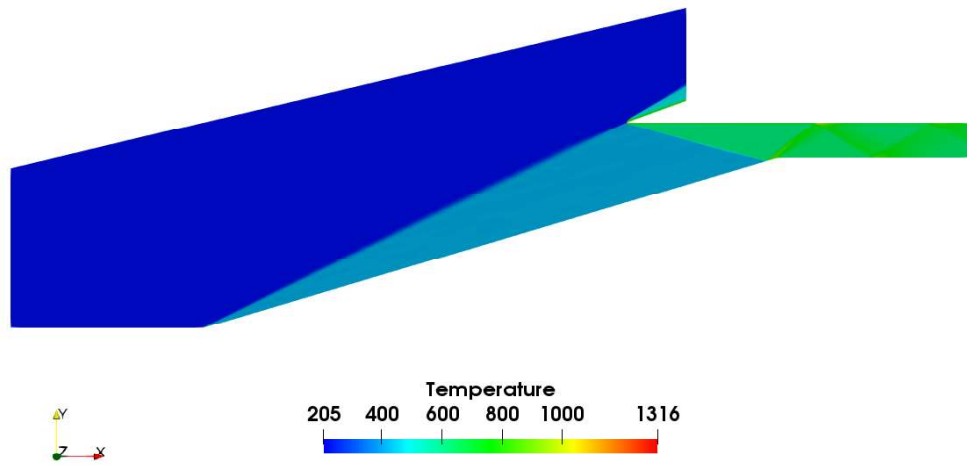

Figure 3.56. Temperature contour for the Baseline Design 3
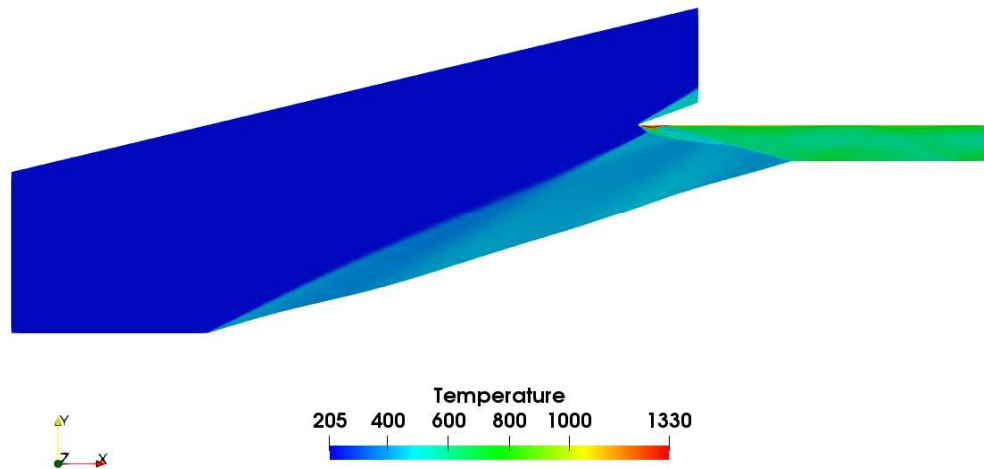
Figure 3.57. Temperature contour for "Optimization Run 3.1"

The change in the ramp surface is illustrated in Figure 3.58.


— Baseline Design
— Final Design
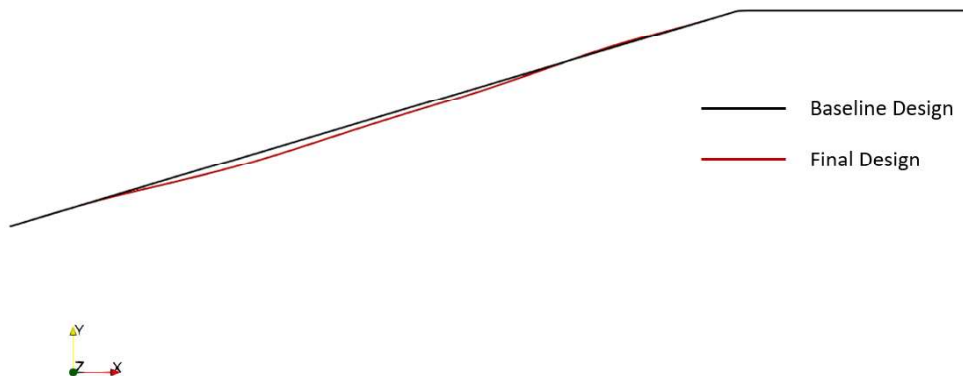
Figure 3.58. The change in the ramp surface of optimized design of Baseline Design 3

As the first and last control points of the FFD box remain constant, no changes occur in these regions, but downward shifts occur in the center of the ramp. The convex-like ramp-geometry is achieved at the end of the optimization process.

Table 3.12 summarizes the changes in the inlet efficiency parameters following optimization.

Table 3.12. Optimization Summary of Baseline Design 3

	J	C	P_{tot} [Pa]	ΔP_{tot} [%]	P	ΔP [%]	$\dot{m}$ [kg/s]	$\Delta \dot{m}$ [%]
Baseline		-	6.30E5	-	6.08E4	-	19.21	-
Final	P_{tot} & $\dot{m}$	P	7.55E5	**19.82**	5.50E4	**-9.50**	19.26	**0.27**

P_{tot} at the exit of the inlet is improved by nearly 20% with the optimization. In addition, a rise of 0.27% in $\dot{m}$ is obtained. Although the static pressure reduces by 9.50%, it is still above 50 kPa. Thus, P_{tot} and $\dot{m}$ are maximized in this case without disrupting the engine's operation.

86

3.3.5. Baseline Design 4

In order to obtain an inlet such that it satisfies the shock on lip and shock on shoulder conditions at the same time and it provides the required compression level for robust combustion, the previous inlet design is modified. The modification implies that the location of the cowl lip is altered according to the same approach as in Baseline Design 2. Intermediate steps also are not provided for this design. The resulting baseline is given in Figure 3.59.
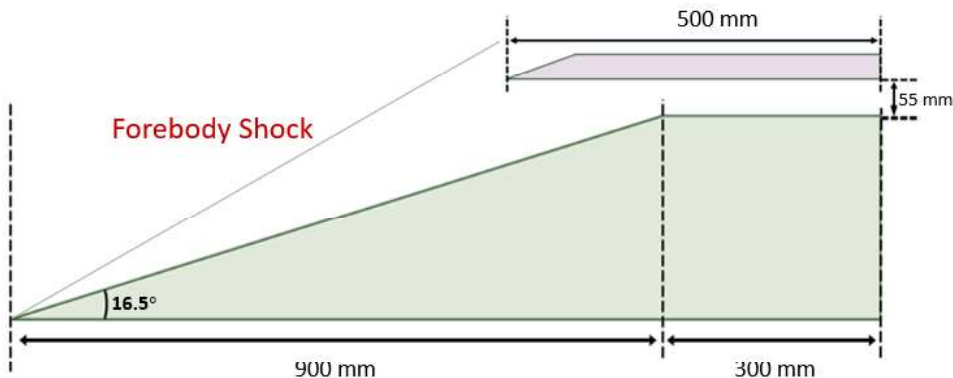
Figure 3.59. Geometrical properties of Baseline Design 4

The goal of the optimization is to maximize P_{tot} and $\dot{m}$, and the static pressure at the exit is not desired to drop below 50 kPa. In other words, objectives are P_{tot} and $\dot{m}$, and the constraint is static pressure.

The variation in P_{tot} and $\dot{m}$ and in the optimization process is given in Figure 3.60. The change in static pressure is presented in Figure 3.61. The final design produced by SU2 during the optimization process has static pressure higher than 50 kPa at the exit plane of the inlet. It is also the best design in terms of P_{tot} and $\dot{m}$.
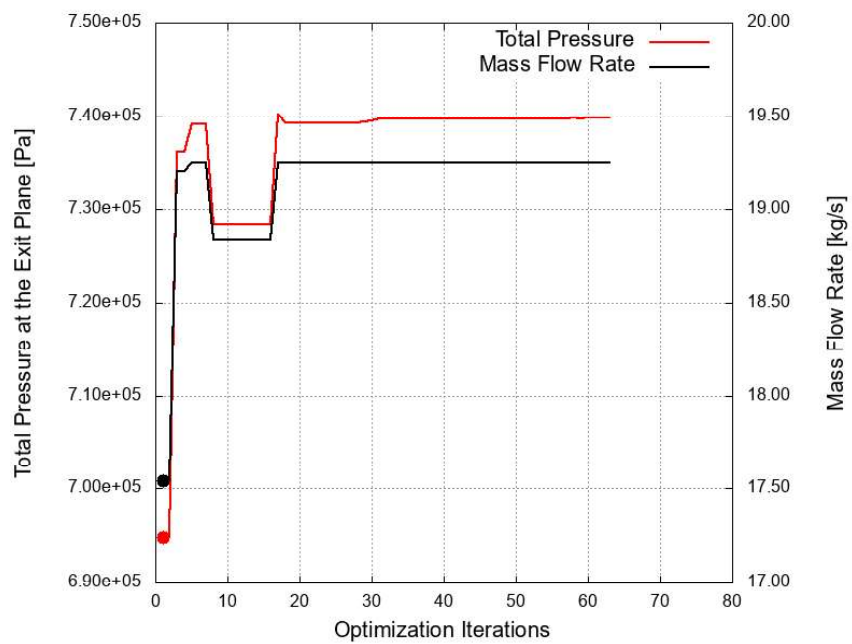
Figure 3.60. Total pressure and mass flow rate variation during the optimization of Baseline Design 4
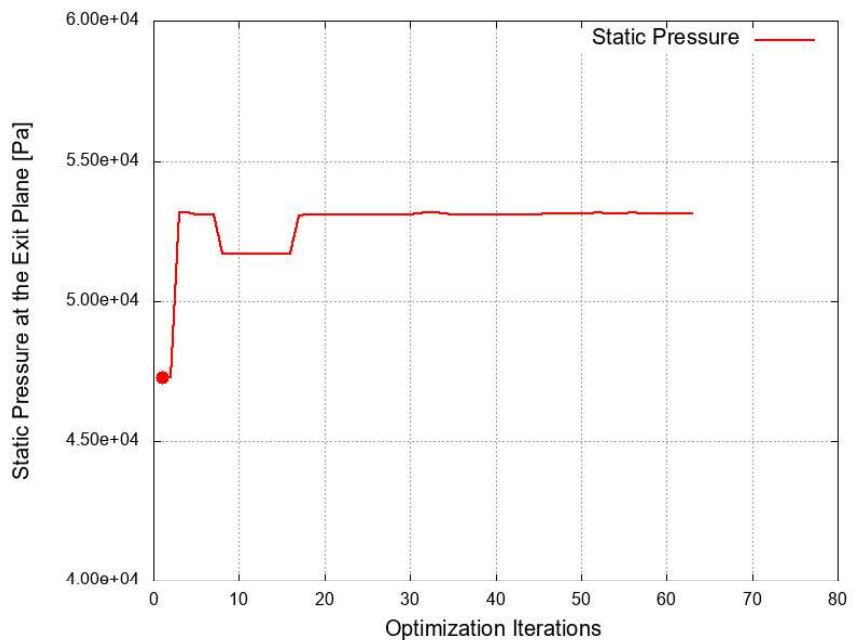
Figure 3.61. Static pressure variation during the optimization of Baseline Design 4

Mach contours for baseline and optimum design are given in Figure 3.62 and Figure 3.63. In the initial design, none of the shock-on-shoulder and shock-on-lip conditions are met, while both are provided at the optimized inlet.
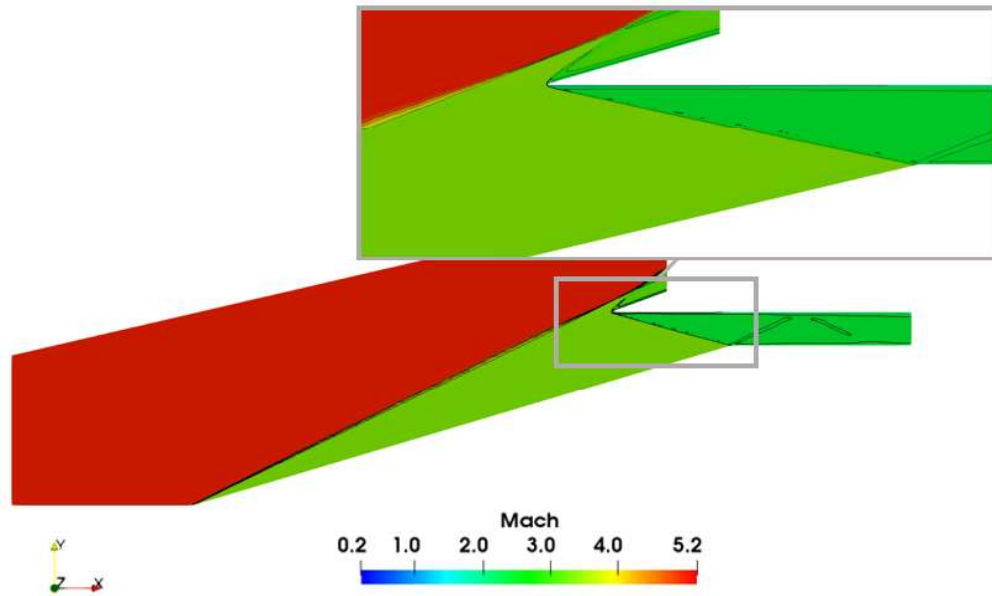
Figure 3.62. Mach contour for Baseline Design 4
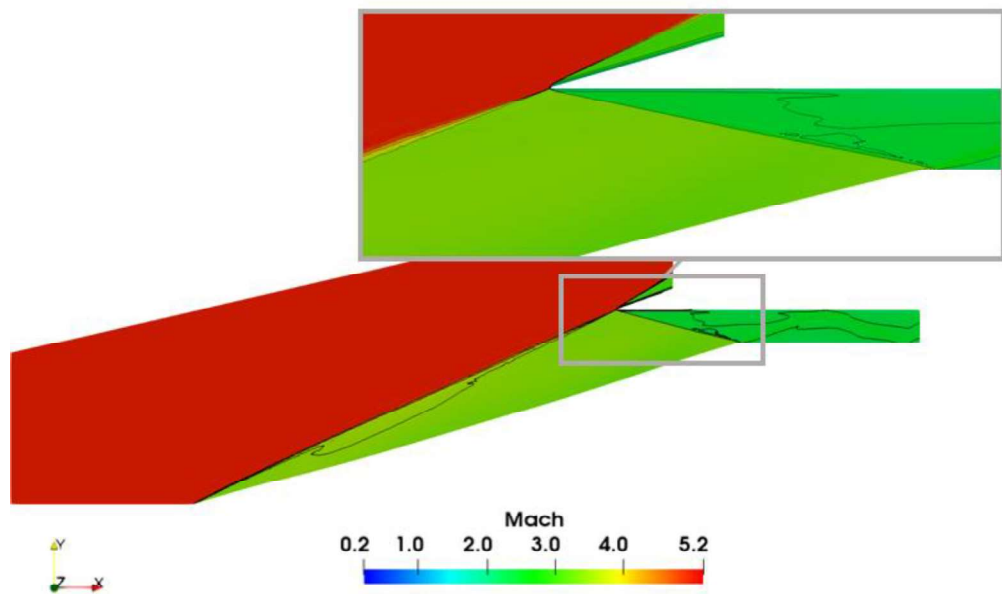
Figure 3.63. Mach contour for optimized geometry of Baseline Design 4

In Figure 3.64 and Figure 3.65, respectively, the pressure contours of the baseline and the optimized inlet are given.
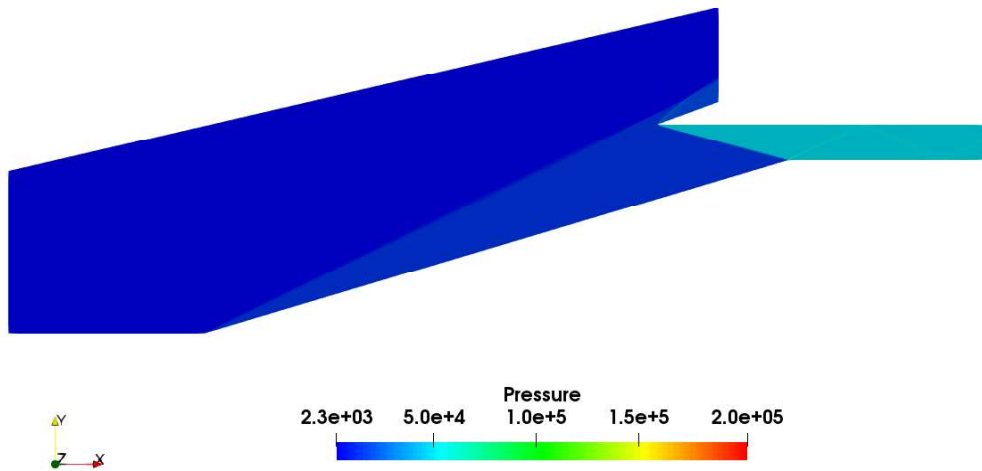
Figure 3.64. Pressure contour for the Baseline Design 4
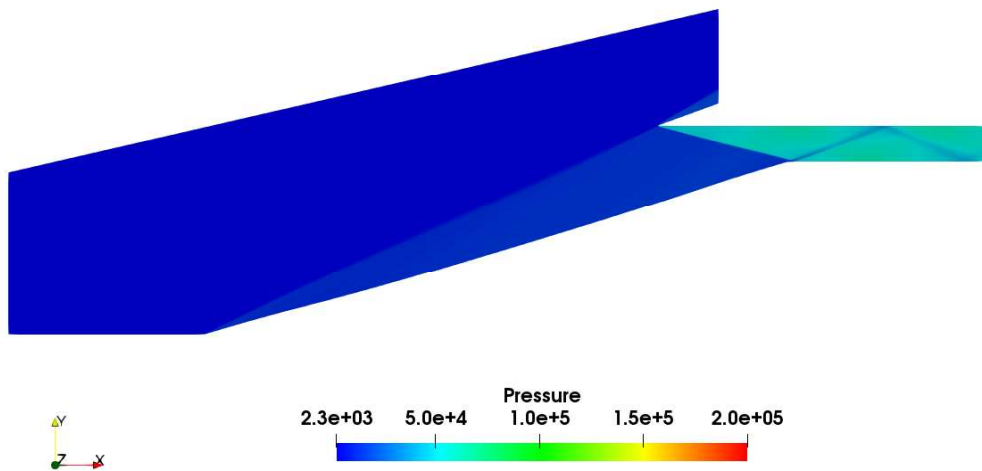
Figure 3.65. Pressure contour for optimized geometry of Baseline Design 4

Temperature distributions on the flow fields for the baseline and optimized geometry are given in Figure 3.66 and Figure 3.67 respectively. Temperature ranges are the same for both flow fields.
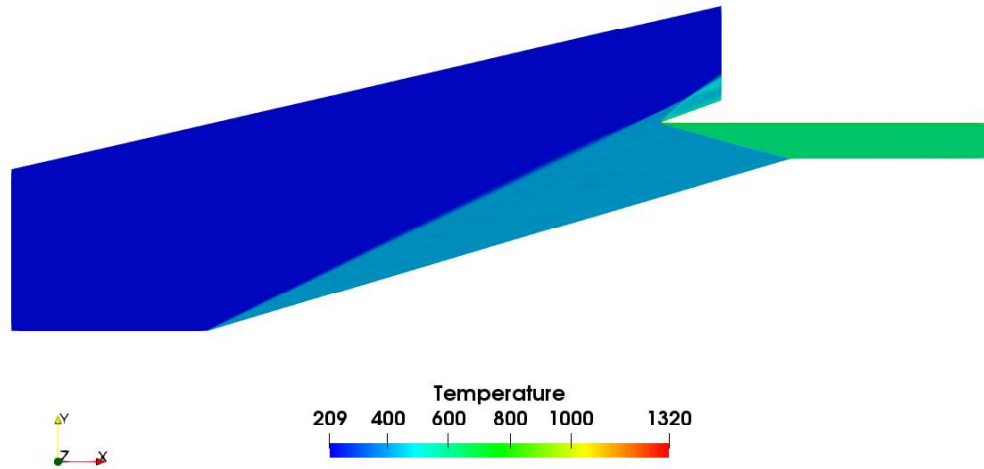
Figure 3.66. Temperature contour for the Baseline Design 4
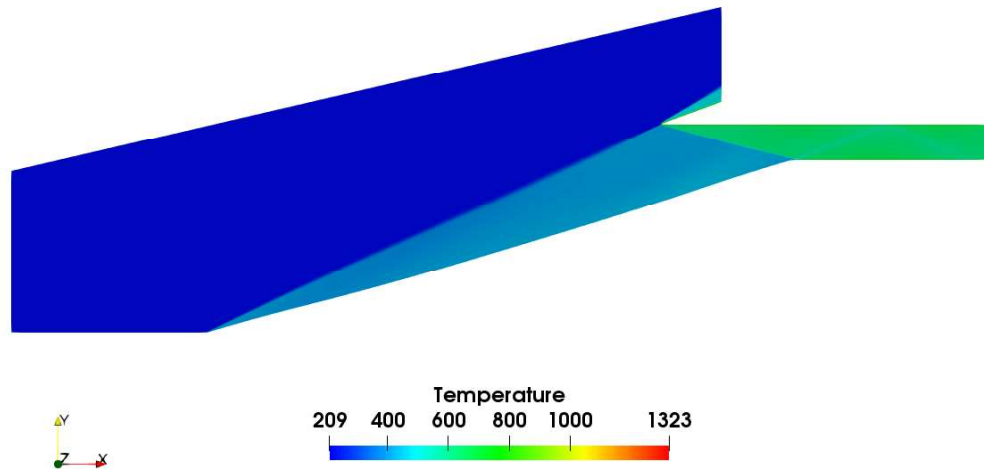
Figure 3.67. Temperature contour for "Optimization Run 4.1"

91
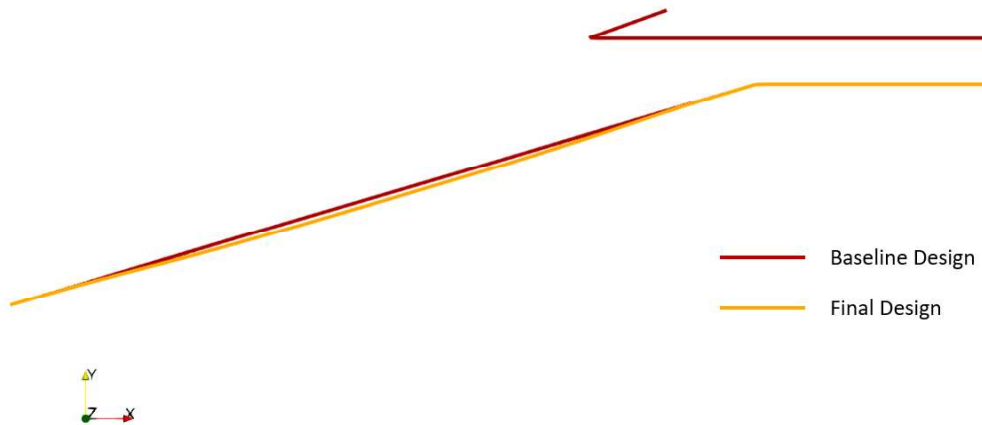
Figure 3.68. The change in the ramp surface of optimized version of Baseline Design 4
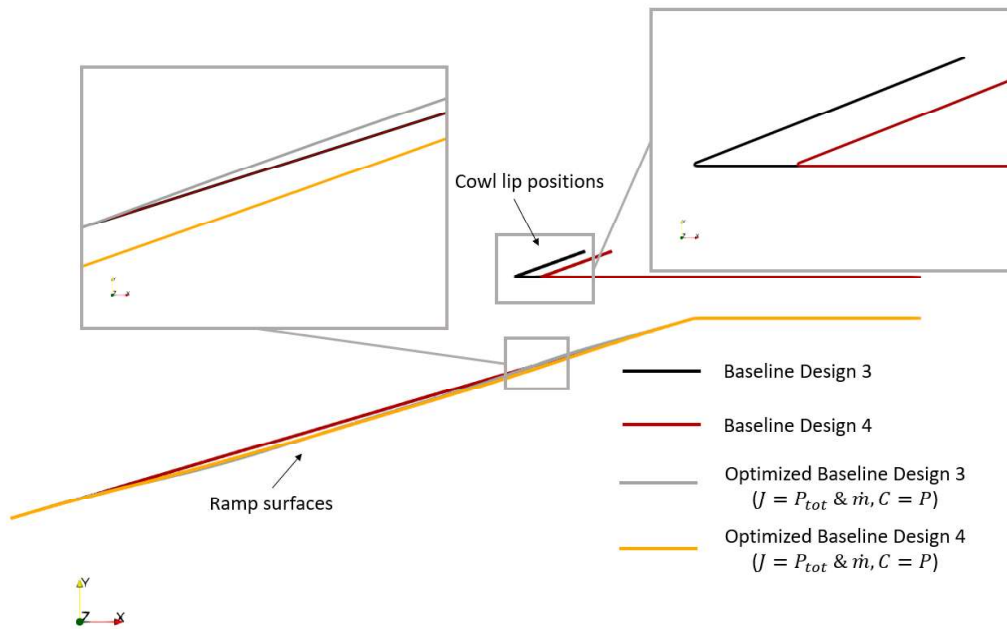
Figure 3.69. Comparison of Baseline Design 3, Baseline Design 4 and their optimized versions

Figure 3.68 shows the shift in the surface of the ramp and Figure 3.69 compares Baseline Design 3, Baseline Design 4 with their optimized versions.

The improvements achieved for Baseline Design 3 and Baseline Design 4 are summarized in Table 3.13. Also, Table 3.14 shows the circumstances of shock-on-lip and shock-on-shoulder conditions for these inlets.

Table 3.13. Performance Parameters of Baseline Design 3 (BD3), Baseline Design 4 (BD4) and their optimized versions

|	J	C	P_{tot} [Pa]	ΔP_{tot} [%]	P	ΔP [%]	$\dot{m}$ [kg/s]	$\Delta\dot{m}$ [%]
BD3	-	-	6.30E5	-	6.08E4	-	19.21	-
Optimized of BD3	P_{tot} & $\dot{m}$	P	7.55E5	**19.82**	5.50E4	**-9.50**	19.26	**0.27**
BD4	-	-	6.95E5	-	4.73E4	-	17.54	-
Optimized of BD4	P_{tot} & $\dot{m}$	P	7.40E5	**6.47**	5.31E4	**12.44**	19.24	**9.73**

Table 3.14. Shock-on-shoulder and shock-on-lip conditions for Baseline Design 3 (BD3), Baseline Design 4 (BD4) and their optimized versions

	J	C	**Shock-on-lip Condition**	**Shock-on-shoulder Condition**
BD3	-	-	✓	✗
Optimized of BD3	P_{tot} & $\dot{m}$	P	✗	✓
BD4	-	-	✗	✗
Optimized of BD4	P_{tot} & $\dot{m}$	P	✓	✓

P_{tot} at the exit of the inlet is increased by nearly 6.5% with respect to Baseline Design 4 and increased by nearly 17.4% with respect to Baseline Design 3 after the optimization. Although the increase in $\dot{m}$ is 9.73% with respect to Baseline Design 4, actually, it is nearly same with $\dot{m}$ of Baseline Design 3. Since spillage occurs in Baseline Design 4, the smallest $\dot{m}$ is obtained in this case. At the end of the optimization of Baseline Design 4, averaged static pressure at the exit plane is nearly 53 kPa which is above 50 kPa. Therefore, it can be said that P_{tot} and $\dot{m}$ are maximized without hindering engine operation and both shock-on-shoulder and shock-on-lip conditions are satisfied simultaneously in this optimization run. Thus, in inviscid circumstances, all the design issues that this thesis focuses on are achieved.

3.4. Viscous Flow Optimizations

Since Baseline Design 1 and Baseline Design 2 are inadequate to reach the required static pressure at the exit plane of the inlet and Baseline Design 4 is modified according to inviscid results of Baseline Design 3, viscous flow optimization is conducted for only Baseline Design 3 among four baseline designs. Then, Baseline Design 5 is created according to findings of optimization of Baseline Design 3.

3.4.1. Optimization Parameters

Except for a few differences, the SU2 settings used in the "Inviscid Flow Optimizations" part remain the same. The first of these differences is related to wall boundary condition. It is defined as no-slip and adiabatic for the viscous cases. The turbulence model is chosen as SA_E due to findings in Section 3.1.

3.4.2. Baseline Design 3

The same objectives and constraints (objectives: P_{tot} and $\dot{m}$, constraint: static pressure) are applied to viscous flow optimizations. The change in P_{tot} and $\dot{m}$ during the optimization process is given in Figure 3.70. and the static pressure variation is shown in Figure 3.71.
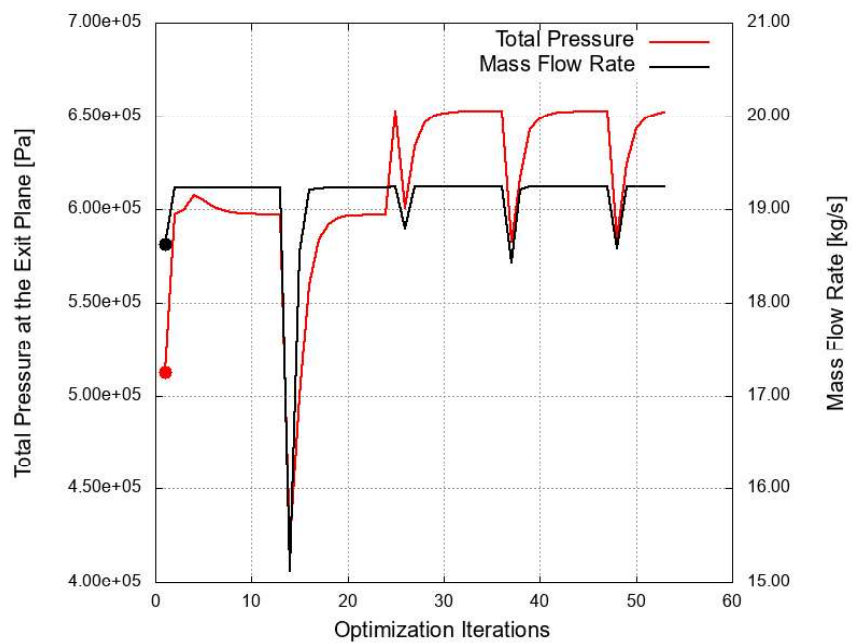
Figure 3.70. Total pressure and mass flow rate variation during the viscous optimization of Baseline
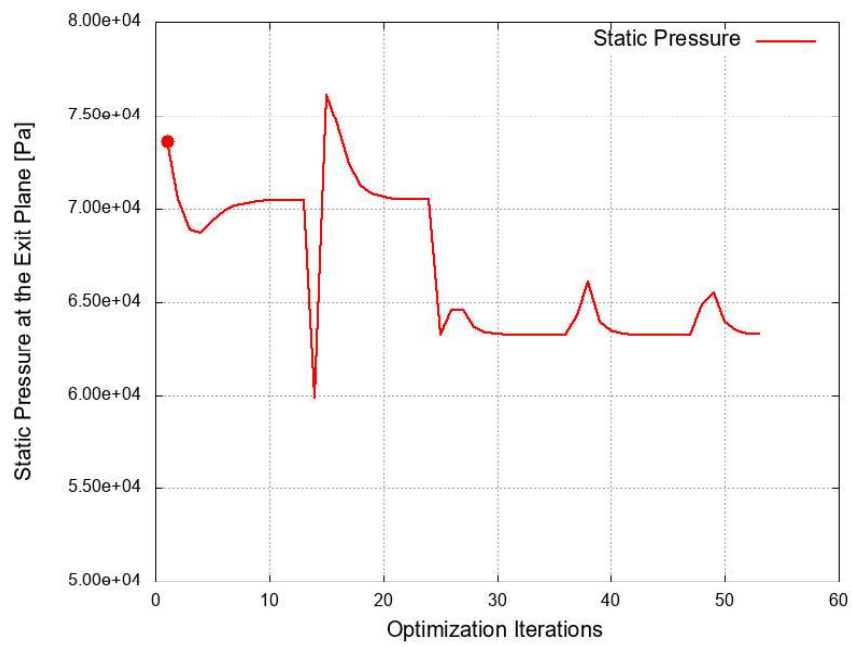
Design 3

Figure 3.71. Static pressure variation during the viscous optimization of Baseline Design 3

In viscous condition, all designs produced by SU2 during the optimization process have static pressure higher than 50 kPa at the exit plane of the inlet which is enough for robust combustion. The best design is obtained at 53rd iteration in terms of P_{tot} and $\dot{m}$. Mach contours for baseline and optimized geometry are illustrated in Figure 3.72. and Figure 3.73.
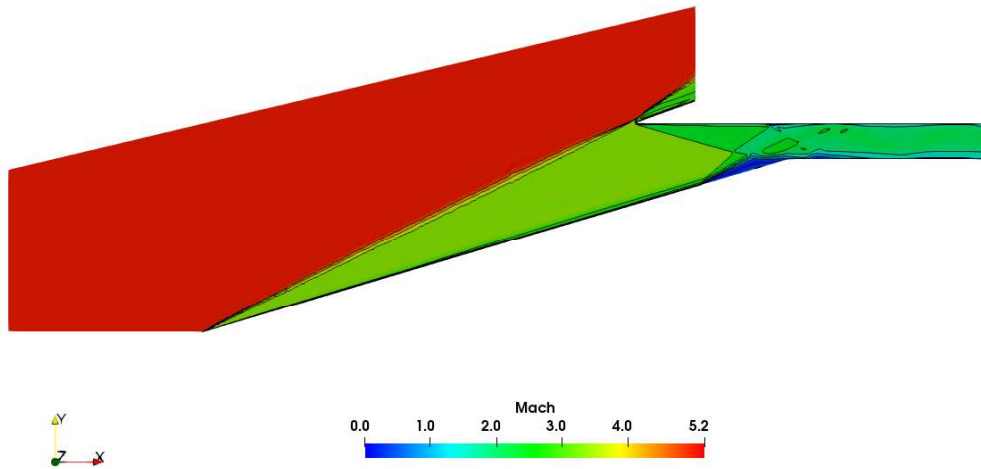
Figure 3.72. Mach contour for Baseline Design 3
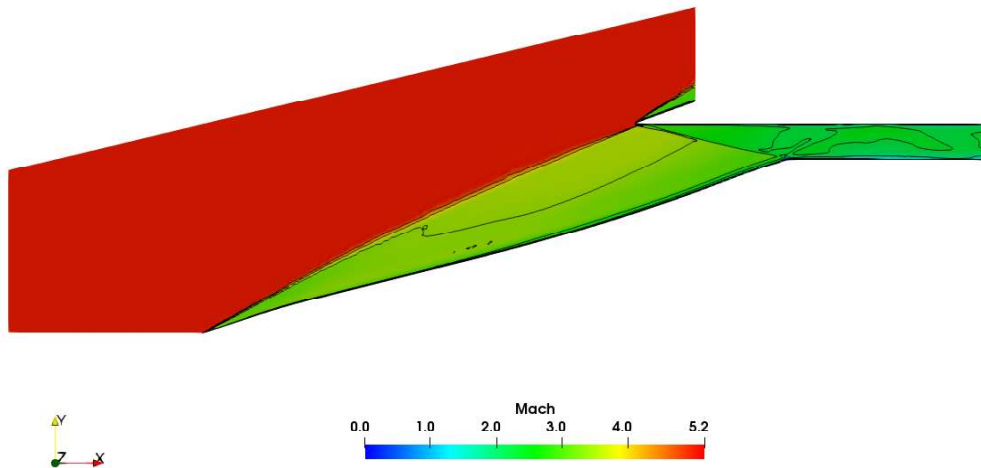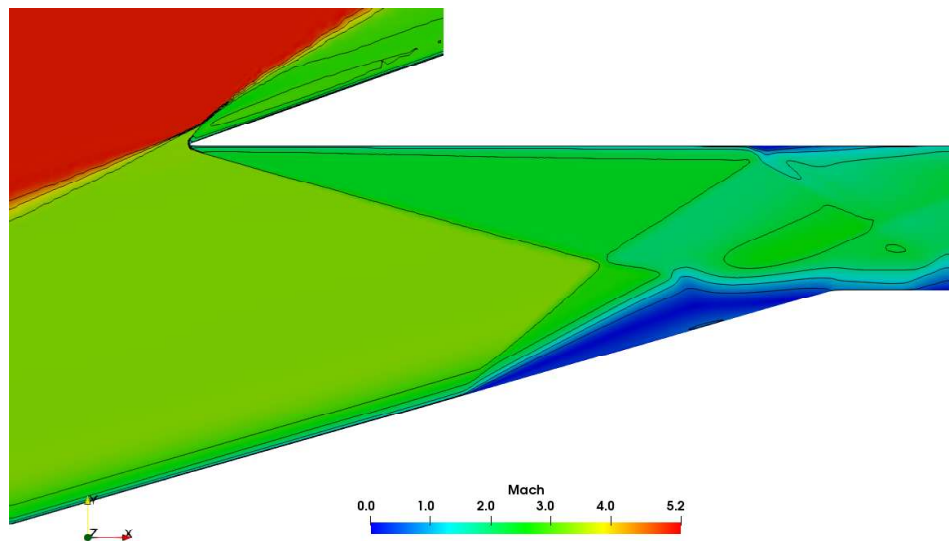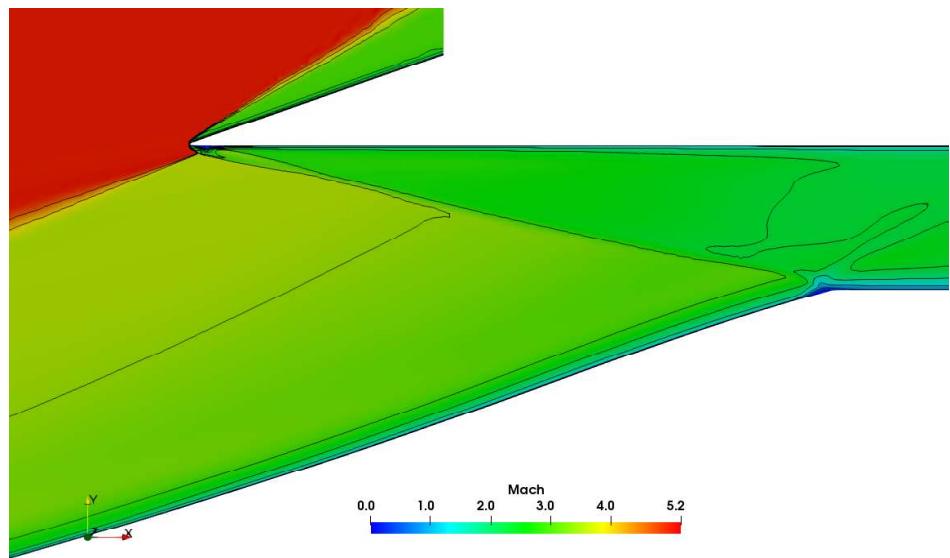
Figure 3.73. Mach contour for optimized geometry of Baseline Design 3

a) Baseline Design 3

b) Optimized geometry of Baseline Design 3

Figure 3.74. Mach contours at inlet throat for a) Baseline Design 3 and b) Optimized geometry of Baseline Design 3

Zoomed to the throat region to get a better perspective (Figure 3.74). Since the shock-on-lip condition is arranged according to inviscid flow, the baseline does not satisfy it. The flow is spilling over the cowl. It is called as spillage. It means loss of compressed air and is therefore not desirable at the design point. Also, a flow separation is observed over the ramp in Baseline Design 3. The separation is caused by the shock reflected from cowl lip. Reflected shock hits the ramp surface, and it creates adverse pressure gradients in this region. It causes the separation of the flow. The optimization to raise $\dot{m}$ and P_{tot}, however, succeeded eliminating this separation. Eliminating of the separation is accomplished by shifting the reflected shock over the shoulder. That causes the forebody shock to get into the engine. It is also undesirable at the design point.

Pressure distributions for the baseline and optimized geometry flow fields are given in Figure 3.75 and Figure 3.76. The shock patterns inside the isolator change entirely after optimization.
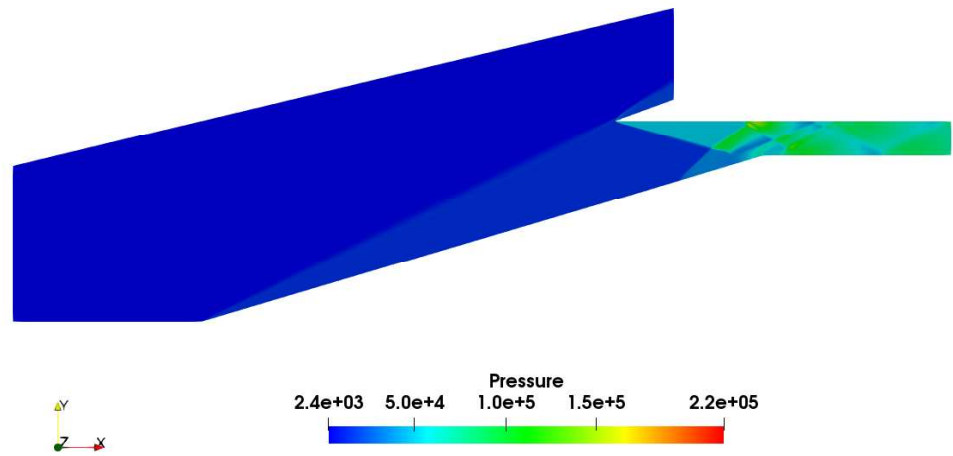
Figure 3.75. Pressure contour for Baseline Design 3
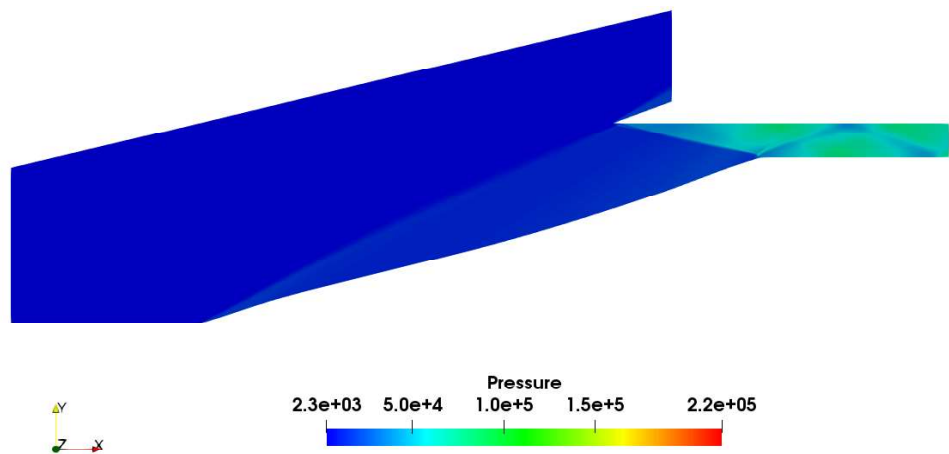
Figure 3.76. Pressure contour for the optimized geometry of Baseline Design 3

Figure 3.77 and Figure 3.78 show the temperature contours of baseline and optimized geometry respectively. After optimization, the high temperatures observed in the separation zone disappear.
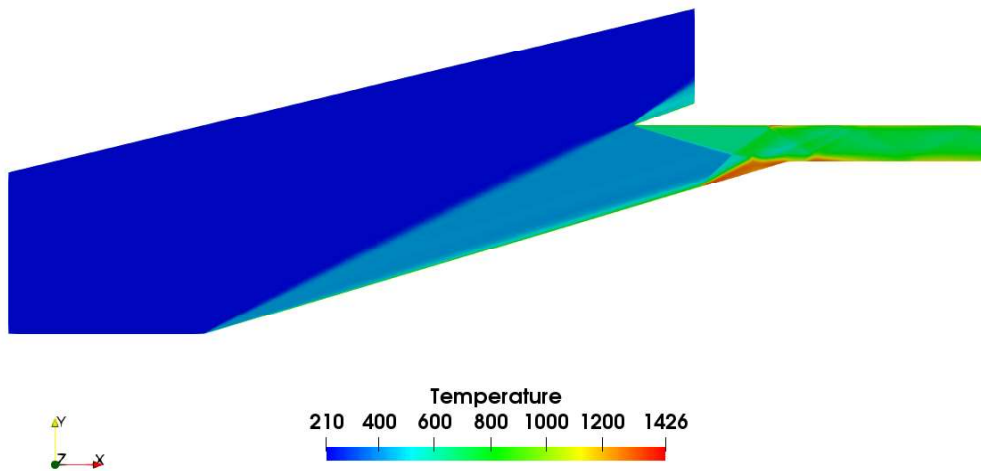

Figure 3.77. Temperature contour for Baseline Design 3
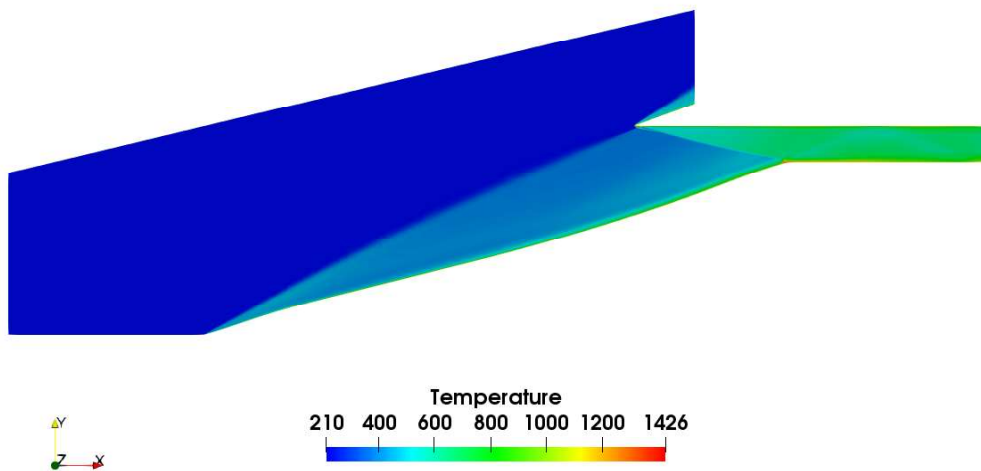
Figure 3.78. Temperature contour for optimized geometry of Baseline Design 3

The change in the ramp surface is illustrated in Figure 3.79.
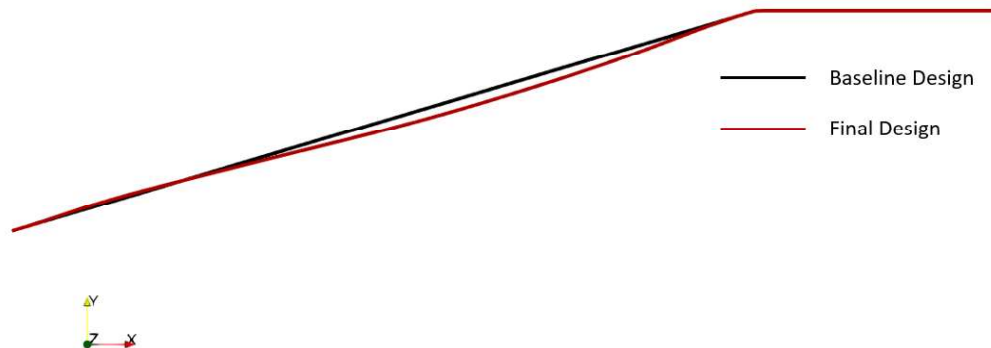
Figure 3.79. The change in the ramp surface of optimized geometry of Baseline Design 3

Since the first and last control points of the FFD box are kept constant, there is no change in these regions. However, there is a downward shift in the middle of the ramp. At the end of the optimization, a convex-like ramp geometry is obtained.

Table 3.15 summarizes the changes in the inlet efficiency parameters following optimization.

Table 3.15. Optimization Summary of Baseline Design 3

	J	C	P_{tot} [Pa]	ΔP_{tot} [%]	P	ΔP [%]	$\dot{m}$ [kg/s]	$\Delta \dot{m}$ [%]
Baseline	-	-	5.13E5	-	7.36E4	-	18.63	-
Final	P_{tot} & $\dot{m}$	P	6.52E5	**27.15**	6.33E4	**-13.98**	19.25	**3.33**

The viscous flow optimization of Baseline Design 3 resulted in a 27% increase in P_{tot}. This is achieved by eliminating shock due to separation. In addition, an increase of 3.33% in $\dot{m}$ is obtained as spillage is prevented. The reduction in static pressure also occurs in this case but it is still above 50 kPa.

In the conceptual design phase of scramjet inlets, inviscid simulations may be used to acquire data roughly. However, viscous effects must be taken into account in the later stages of the design. In this study, inlet aerodynamics under both viscous and inviscid conditions are investigated. As expected, the results obtained in the two conditions are very different from each other. The flow pattern and behavior completely changes when viscous effects are included. For example, the separation due to shock-boundary layer interaction cannot be observed in Euler simulations. The inviscid and viscous flow optimizations of Baseline Design 3 yielded different geometries. Optimized ramp surfaces obtained under inviscid and viscous conditions are given in Figure 3.80. The optimized geometry obtained under viscous conditions has a more curved structure. In the locations near the forebody leading edge and ramp shoulder, these two geometries are deformed in exactly the opposite directions with respect to the baseline design. Therefore, it can be stated that the aerodynamic shape optimization of a scramjet inlet ramp should be performed under viscous flow conditions. Otherwise, a completely different result will be obtained.
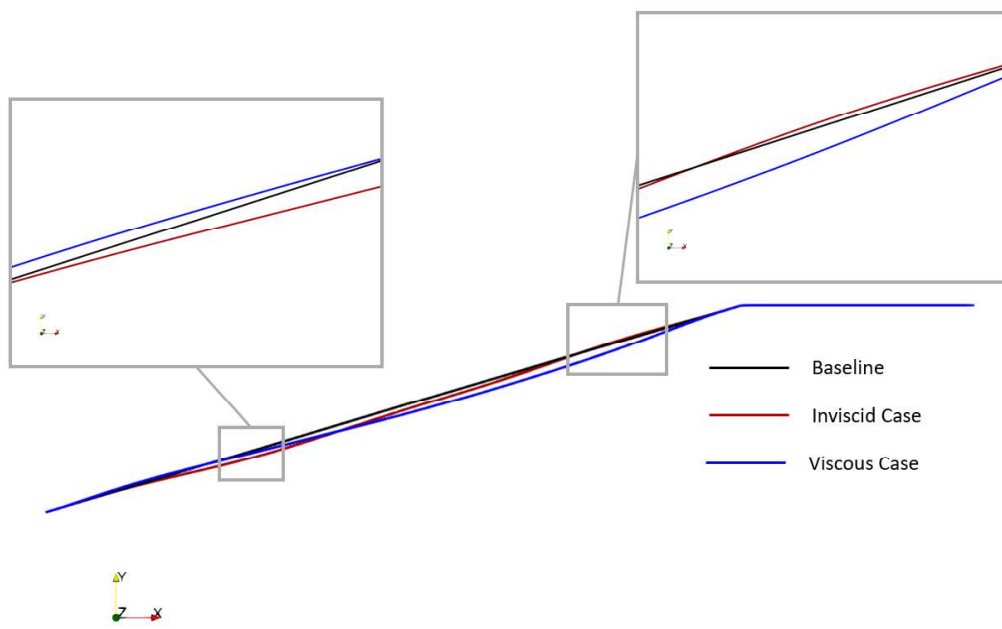
Figure 3.80. Comparison of viscous flow and inviscid flow optimizations

3.4.3. Baseline Design 5

The geometry obtained in the previous optimization study does not meet the shock-on-lip condition. Therefore, the cowl lip in Baseline Design 3 is shifted 9 mm to the right to achieve a design that meets this requirement. The resulting baseline design is visualized in Figure 3.81. The optimization strategy is still the same (objectives: P_{tot} and $\dot{m}$, constraint: static pressure). The change in P_{tot}, $\dot{m}$ and P during the optimization steps is shown in Figure 3.82 and Figure 3.83.
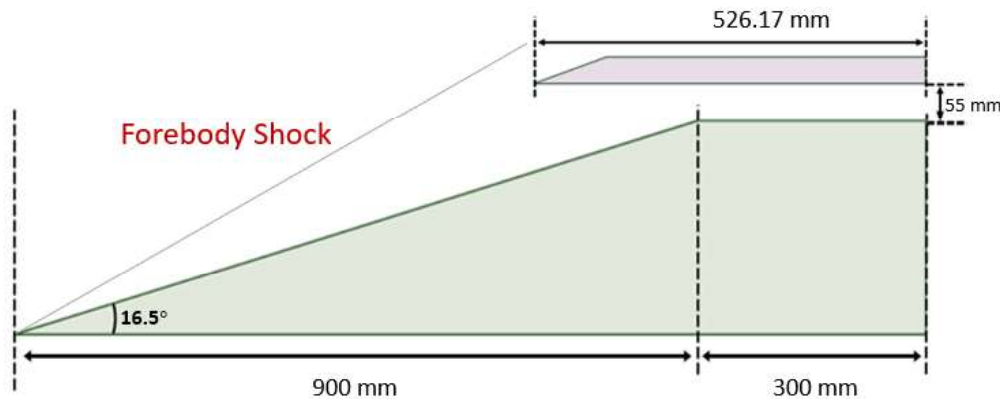
Figure 3.81. Baseline Design 5
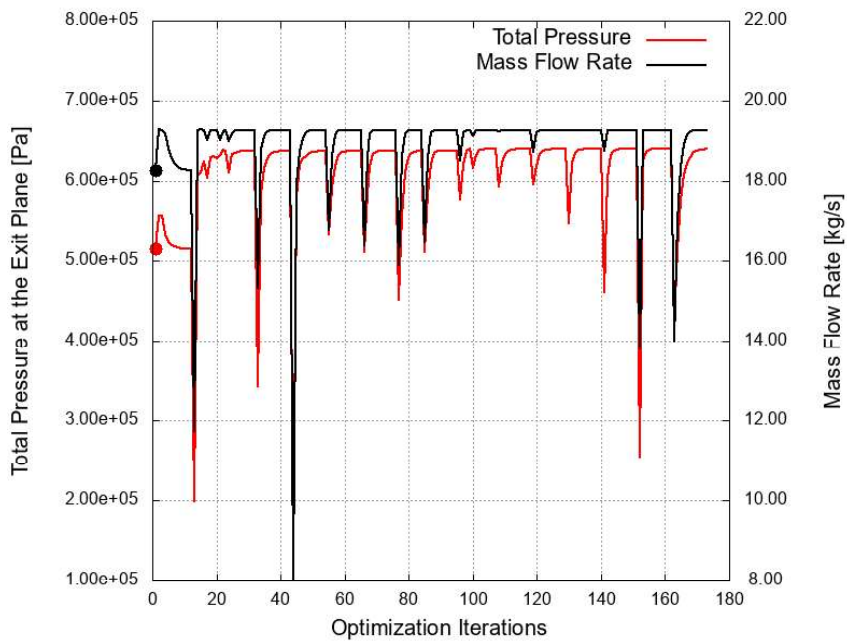
Figure 3.82. Total pressure and mass flow rate variation during the viscous optimization of Baseline
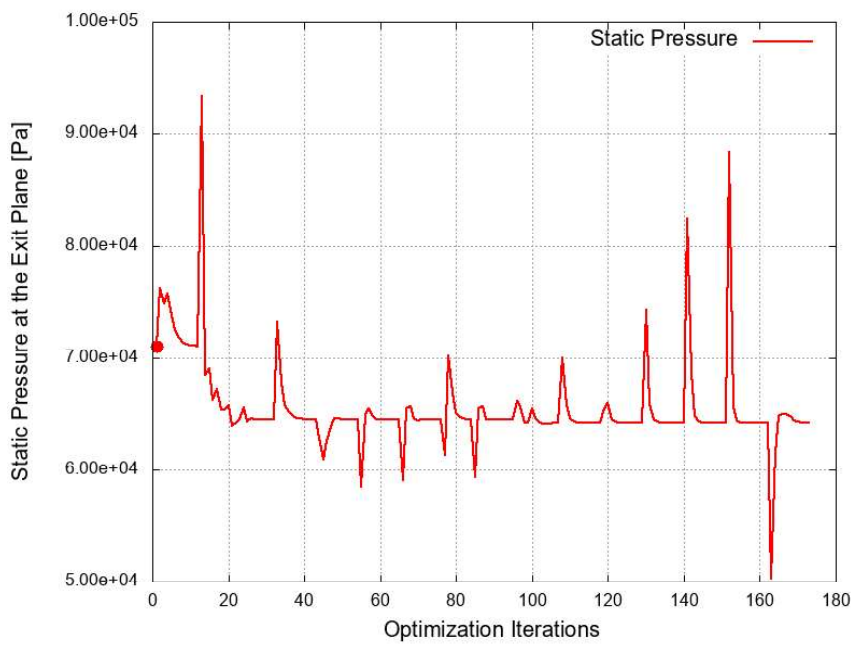
Design 5

Figure 3.83. Static pressure variation during the viscous optimization of Baseline Design 5

During the optimization, no design is created that damages the constraint. For all designs, the pressure at the exit is greater than 50 kPa. Mach contours for the baseline and optimized inlet are shown in Figure 3.84 and Figure 3.85.
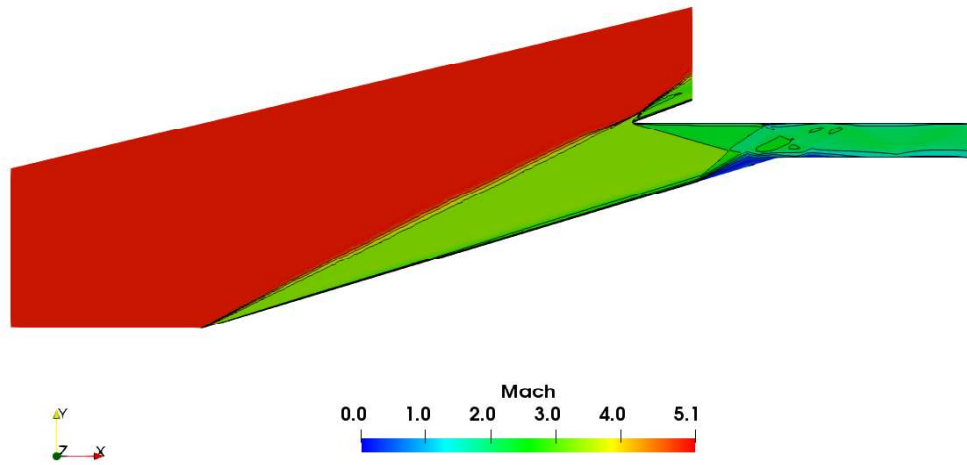
Figure 3.84. Mach contour for Baseline Design 5
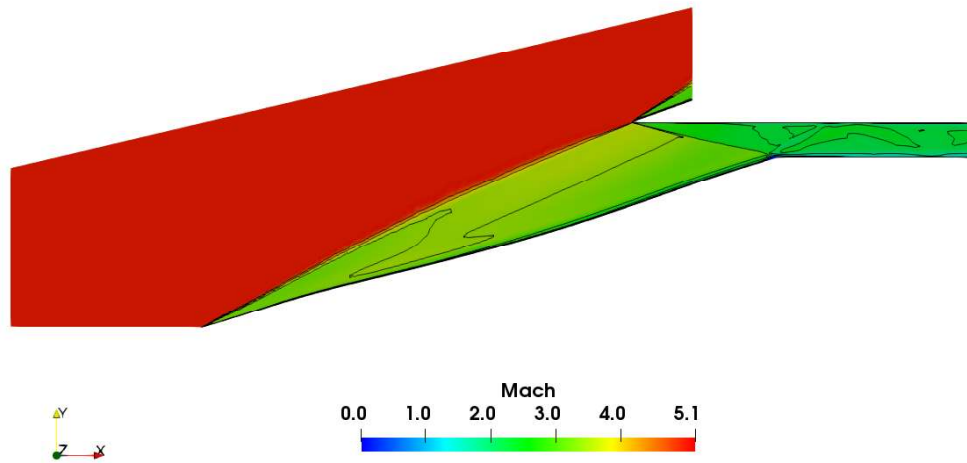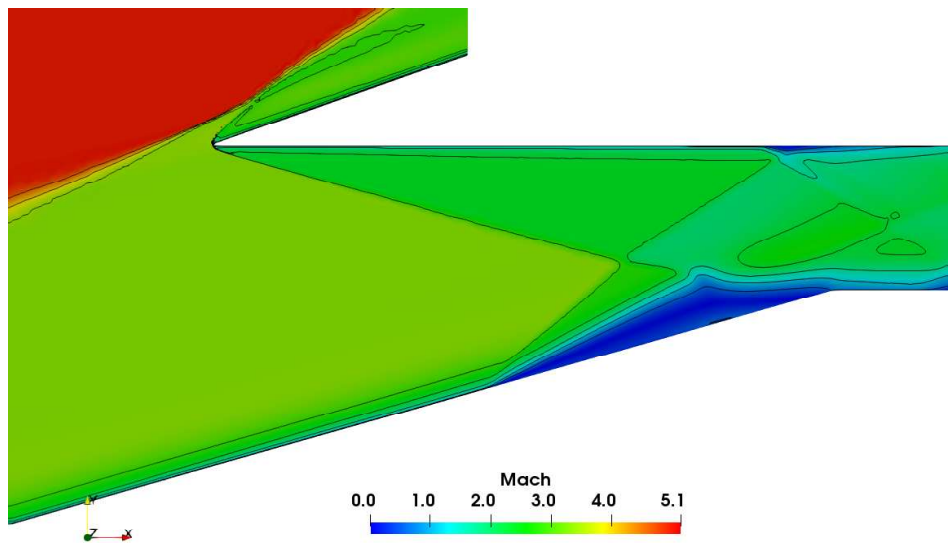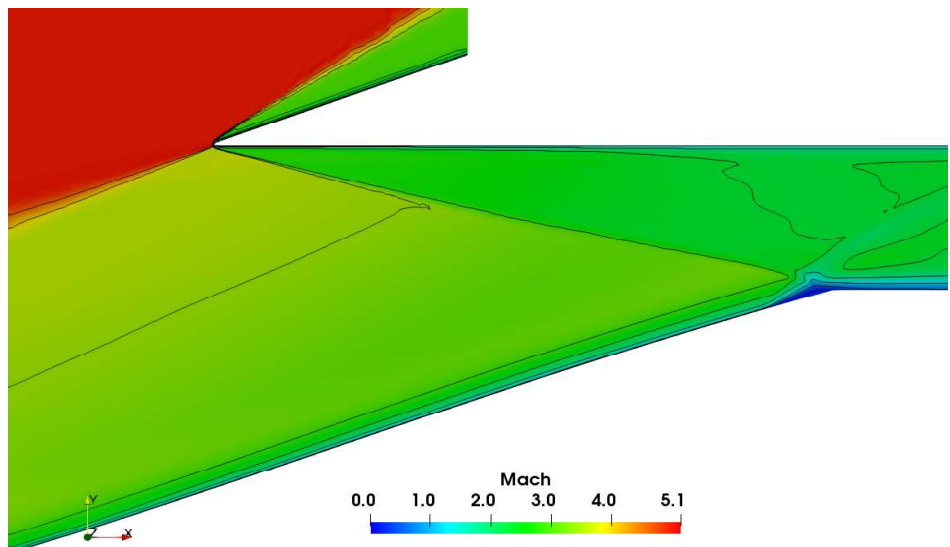
Figure 3.85. Mach contour for optimized geometry of Baseline Design 5

a) Baseline Design 5

b) Optimized geometry of Baseline Design 5

Figure 3.86. Mach contours at inlet throat for a) Baseline Design 5 and b) Optimized geometry of Baseline Design 5

106

Mach contours at the throat area are shown in Figure 3.86. The initial design does not meet both the shock-on-shoulder and shock-on-lip conditions, while both conditions are satisfied in the optimized geometry. This narrows the separation zone. While the separation starts on the ramp before optimization, it is observed only in a small area in the shoulder region after optimization.

Pressure distributions on the flow fields of baseline and optimized geometry are illustrated in Figure 3.87 and Figure 3.88 respectively. The inside shock patterns alter completely following optimization.
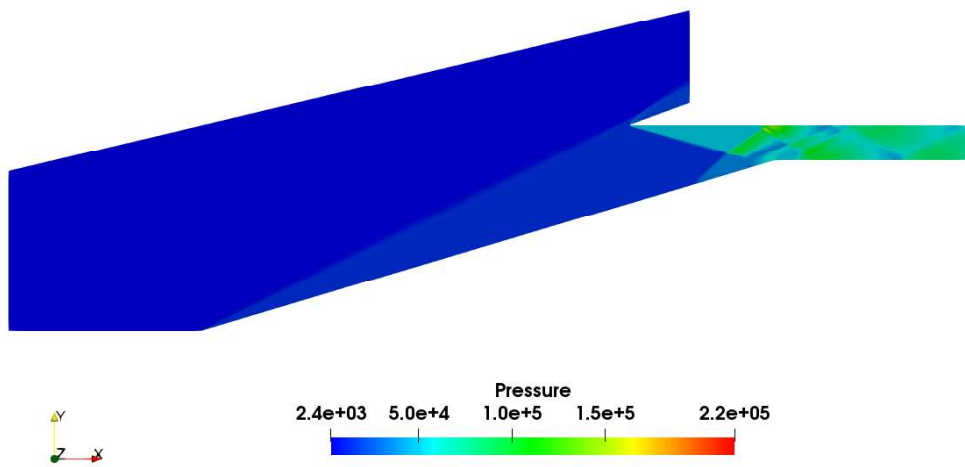
Figure 3.87. Pressure contour for Baseline Design 5
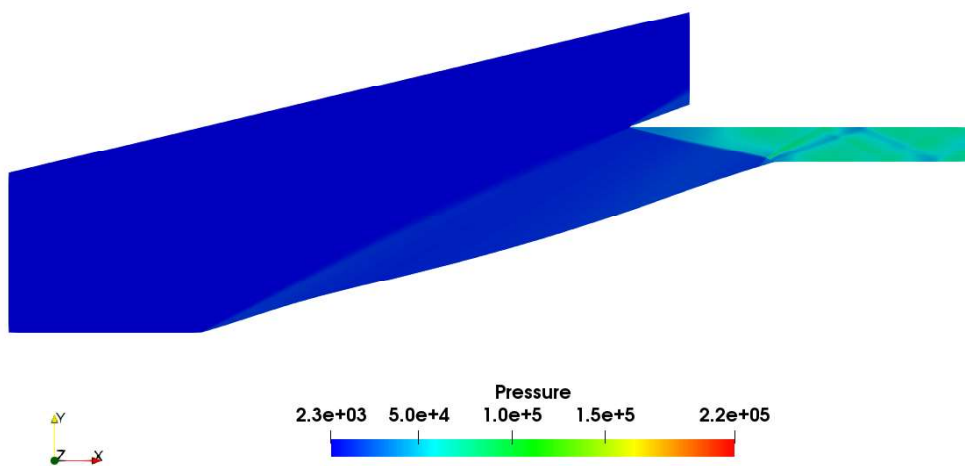
Figure 3.88. Pressure contour for the optimized geometry of Baseline Design 5

Figure 3.89 and Figure 3.90 show the temperature contours of baseline and optimized geometry respectively. The optimization reduces the high temperature-zones observed in the baseline flow field.
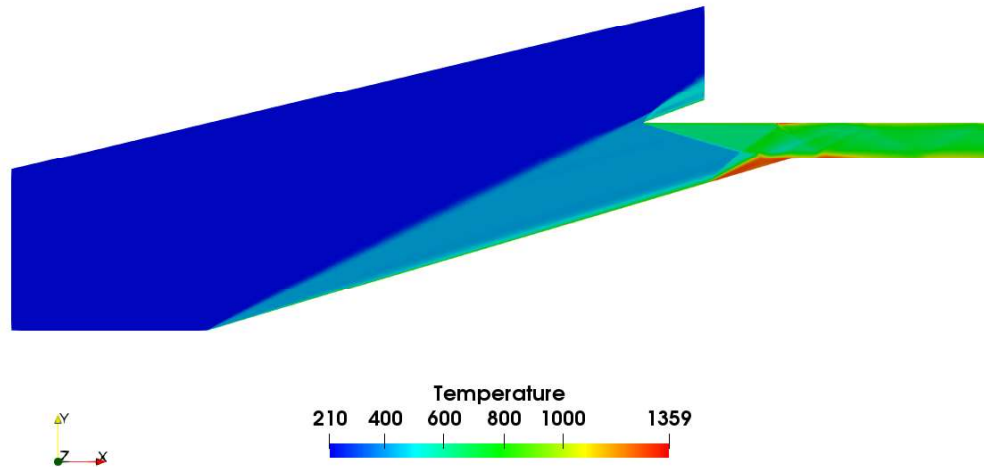
Figure 3.89. Temperature contour for Baseline Design 5
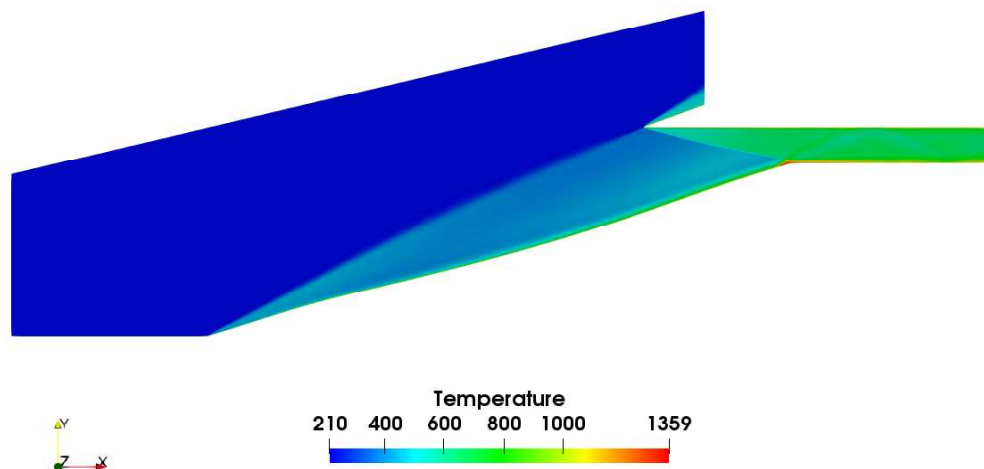
Figure 3.90. Temperature contour for optimized geometry of Baseline Design 5

The change in the ramp surface is illustrated in Figure 3.91.
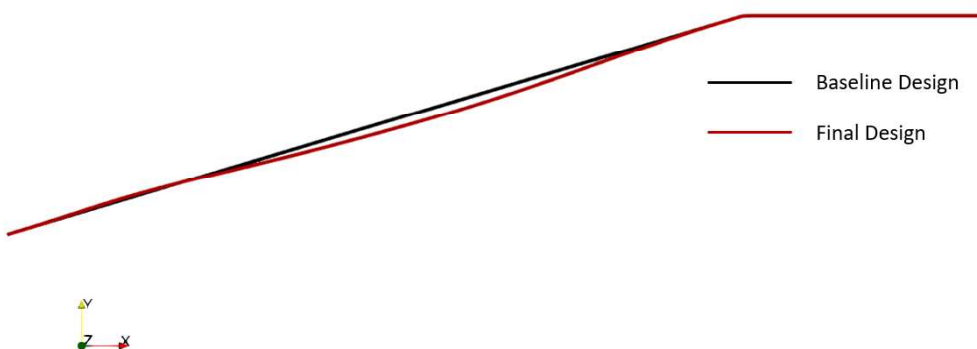
Figure 3.91. The change in the ramp surface of optimized geometry of Baseline Design 5

The results of optimizations conducted for Baseline Design 3 and Baseline Design 5 are tabulated in Table 3.16.

Table 3.16. Performance Parameters of Baseline Design 3 (BD3), Baseline Design 5 (BD5) and their optimized versions

	J	C	P_{tot} [Pa]	ΔP_{tot} [%]	P	ΔP [%]	$\dot{m}$ [kg/s]	$\Delta\dot{m}$ [%]
BD3	-	-	5.13E5	-	7.36E4	-	18.63	-
Optimized of BD3	P_{tot} & $\dot{m}$	P	6.52E5	**27.15**	6.33E4	**-13.98**	19.25	**3.33**
BD5	-	-	5.14E5	-	7.10E4	-	18.25	-
Optimized of BD5	P_{tot} & $\dot{m}$	P	6.39E5	**24.31**	6.42E4	**-9.62**	19.26	**5.52**

The inlets that meet and do not meet the shock-on-shoulder and shock-on-lip conditions are given in Table 3.17.

Table 3.17. Shock-on-shoulder and shock-on-lip conditions for Baseline Design 3 (BD3), Baseline Design 5 (BD5) and their optimized versions

	J	C	Shock-on-lip Condition	Shock-on-shoulder Condition
BD3	-	-	✗	✗
Optimized of BD3	P_{tot} & $\dot{m}$	P	✗	✓
BD5	-	-	✗	✗
Optimized of BD5	P_{tot} & $\dot{m}$	P	✓	✓

The optimization of Baseline Design 5 improves P_{tot} with a 19.% increase in P_{tot}. In addition, an increase of 5.52% in $\dot{m}$ is obtained. The reduction in static pressure also occurs in this case. However, the average pressure at the exit of the inlet drops by %9.62. Consequently, this optimization case improved the objectives of the study. Also, the static pressure constraint for robust combustion is satisfied. Moreover, both shock-on-lip and shock-on-shoulder conditions are fulfilled simultaneously with this design while they are failing before the optimization.

CHAPTER 4

CONCLUSIONS

In this thesis, aerodynamic shape optimizations for single-ramp inlets are performed. The adjoint method is chosen for this task. Generally, this optimization method is not used for scramjet inlet optimizations. Conventional design methods use parameters such as ramp angle, ramp length and ramp number as design variables. This study uses the FFD box strategy to specify design variables. The control points of the FFD box are design variables in this strategy. The variation in FFD control points deforms the mesh and the solid surface. The surface deformation is carried out in accordance with the sensitivity information obtained from the adjoint solution.

Before the optimization process, a verification study is performed at Mach 5. In this verification case, various turbulence models available in SU2 software are assessed, and a mesh dependence study is performed. Results are in harmony with the experimental data. Also, another verification study is conducted at Mach 6. The findings in the first study are confirmed in the second case

In this study, five baseline inlets have been designed and optimized. In order to check the limits of this unconventional optimization method, the ramp angles of the first two baseline designs are indicated less than the examples in the literature. In the design of the first baseline, shock-on-shoulder condition is neglected which is important to transform the air as parallel to engine surface. Four different optimization case is performed for the first baseline. These are unconstrained single-objective total pressure optimization, unconstrained multi-objective optimization (objectives: P_{tot} & $\dot{m}$), unconstrained single-objective static pressure optimization and constrained multi-objective optimization (objectives: P_{tot} & $\dot{m}$; constraint: static pressure). Unconstrained single-objective static pressure optimization does not produce a logical

113

design. In the constrained multi-objective optimization, the software keeps the baseline design mostly due to challenging static pressure constraint. In the unconstrained single-objective total pressure optimization and unconstrained multi-objective optimization cases, the shock-on-lip condition is sacrificed to fulfill the shock-on-shoulder condition. These optimization cases show that it is possible to obtain a design that satisfies both shock-on-shoulder and shock-on-lip conditions by moving the cowl lip in the first baseline. By traditional design techniques, accomplishing this task is impossible without changing the throat area. Although the desired conditions are met with the optimization of the second baseline, averaged static pressure at the exit plane of the inlet cannot exceed 50 kPa. This makes the scramjet inlet impossible to perform its main task. This is because the ramp angle in the baseline designs is relatively small (11°). It should be increased further to reach the required pressure level. Therefore, it is decided to design a new baseline geometry which has larger ramp angle. After the same process is repeated for the new baseline, the shock-on-shoulder and shock-on-lip conditions are both satisfied simultaneously, and the required compression is achieved with the optimized geometry in inviscid circumstances. In addition, P_{tot} is improved. However, the increase in $\dot{m}$ is not as much as P_{tot}.

RANS simulations are performed for only the baseline design has bigger ramp angle. The similar results are also obtained in the viscous case. In the optimized design, P_{tot} and $\dot{m}$ are maximized and shock-on-shoulder is satisfied. This eliminates the flow separation due to reflected shock, but it causes the forebody shock to get into the engine. It is undesirable at the design point. Therefore, the cowl lip is shifted to the right, and a new baseline is designed. After the optimization of the last baseline, both shock-on-shoulder and shock-on-lip conditions are met at the same design. Also, optimization of the last baseline is improved P_{tot} by %24.31. $\dot{m}$ increases by %5.52.

REFERENCES

[1]   S. Hasegawa and D. Knight, "Application of Optimization Algorithms to Scramjet Inlet Design," 2012.

[2]   E. T. Curran, "Scramjet Engines: The First Forty Years," *J. Propuls. Power*, 2001.

[3]   M. Smart, "Scramjets," *Aeronaut. J.*, 2007.

[4]   R. J. Weber and J. S. MacKay, "An Analysis of Ramjet Engines Using Supersonic Combustion," *J. Appl. Phys.*, 1958.

[5]   N. Hall, "Specific Impulse," *NASA Glenn Research Center*, 2015. [Online]. Available: https://www.grc.nasa.gov/WWW/K-12/airplane/specimp.html. [Accessed: 12-Jul-2019].

[6]   E. T. Curran and S. N. B. Murthy, *Scramjet propulsion*, vol. 189. AIAA, 2001.

[7]   S. Seckin and K. B. Yuceil, "Flow visualization of a scramjet inlet–isolator model in supersonic flow," in *EPJ Web of Conferences*, 2013, vol. 45, p. 1099.

[8]   R. S. Fry, "A Century of Ramjet Propulsion Technology Evolution," *J. Propuls. Power*, 2008.

[9]   M. T. Akpolat, "Scramjet Motorları İçin Deney Tasarımı Metodlarını Kullanarak Kavramsal Tasarım Yönteminin Geliştirilmesi (in Turkish)," Erciyes University, 2014.

[10]   M. Conner, "X-43A (Hyper-X)," 2016. [Online]. Available: https://www.nasa.gov/centers/armstrong/history/experimental_aircraft/X-43A.html. [Accessed: 15-May-2019].

[11] J. Hank, J. Murphy, and R. Mutzman, "The X-51A Scramjet Engine Flight Demonstration Program," 2012.

[12] D. Haudrich and L. Brase, *Flutter and Divergence Assessment of the HyFly Missile*. 2009.

[13] S. Walker, M. Tang, S. Morris, and C. Mamplata, *Falcon HTV-3X - A Reusable Hypersonic Test Bed*. 2008.

[14] "Hyper Sonic Technology Demonstrator Vehicle," *Full Afterburner*, 2017. [Online]. Available: http://fullafterburner.weebly.com/next-gen-weapons/hyper-sonic-technology-demonstrator-vehicle. [Accessed: 15-Jul-2019].

[15] P. Toro *et al.*, *Brazilian 14-X Hypersonic Aerospace Vehicle Project*. 2012.

[16] F. Falempin and L. Serre, "French flight test program LEA status," MBDA LE PLESSIS ROBINSON (FRANCE), 2010.

[17] W. H. Heiser and D. T. Pratt, *Hypersonic airbreathing propulsion*. Aiaa, 1994.

[18] J. D. Anderson, *Hypersonic and high temperature gas dynamics*. 2000.

[19] L. H. Quan, N. P. Hung, L. D. Quang, and V. N. Long, "Analysis and Design of a Scramjet Engine Inlet Operating from Mach 5 to Mach 10," *Int. l J. Mech. Eng. Appl.*, vol. 4, pp. 11–23, 2016.

[20] R. P. Bajpai, U. Chandrasekhar, and A. R. Arankalle, *Innovative Design, Analysis and Development Practices in Aerospace and Automotive Engineering: I-DAD 2014, February 22-24, 2014*. Springer Science & Business, 2014.

[21] A. C. Idris, "Characterization of High Speed Inlets Using Global Measurement Techniques." The University of Manchester (United Kingdom), 2014.

[22] M. K. Smart, "Scramjet inlets," QUEENSLAND UNIV BRISBANE (AUSTRALIA) CENTRE FOR HYPERSONICS, 2010.

[23] M. K. Smart, "How Much Compression Should a Scramjet Inlet Do?," *AIAA J.*, 2012.

[24] M. G. Bricalli, "Numerical study into thermal-compression scramjets," 2015.

[25] A. Antoniou and W. S. Lu, *Practical optimization: Algorithms and engineering applications*. 2007.

[26] G. A. Bekey and S. F. Masri, "Random search techniques for optimization of nonlinear systems with many parameters," *Math. Comput. Simul.*, vol. 25, no. 3, pp. 210–213, 1983.

[27] M. K. Smart, "Optimization of two-dimensional scramjet inlets," *J. Aircr.*, vol. 36, no. 2, pp. 430–433, 1999.

[28] H. Ogawa and R. R. Boyce, "Physical insight into scramjet inlet behavior via multi-objective design optimization," *AIAA J.*, vol. 50, no. 8, pp. 1773–1783, 2012.

[29] N. Acharya, S. Sharma, L. Silwal, and S. Bhattrai, "Design and Numerical Analysis of Mixed Compression Inlet of a Shcramjet Engine," 2016.

[30] N. O. P. Raj and K. Venkatasubbaiah, "A new approach for the design of hypersonic scramjet inlets," *Phys. Fluids*, vol. 24, no. 8, p. 86103, 2012.

[31]   H. L. Kline, F. Palacios, T. D. Economon, and J. J. Alonso, "Adjoint-based optimization of a hypersonic inlet," in *22nd AIAA Computational Fluid Dynamics Conference*, 2015, p. 3060.

[32]   H. L. Kline, T. D. Economon, and J. J. Alonso, "Mulit-objective optimization of a hypersonic inlet using generalized outflow boundary conditions in the continuous adjoint method," in *54th AIAA Aerospace Sciences Meeting*, 2016, p. 912.

[33]   H. L. Kline, "The Continuous Adjoint Method for Multi-Fidelity Hypersonic Inlet Design," STANFORD UNIVERSITY, 2017.

[34]   G. Carrier, D. Knight, K. Rasheed, and X. Montazel, "Multi-criteria design optimization of two-dimensional supersonic inlet," in *39th Aerospace Sciences Meeting and Exhibit*, 2001, p. 1064.

[35]   G. Yang and A. Da Ronch, *Aerodynamic Shape Optimisation of Benchmark Problems Using SU2*. 2018.

[36]   J. E. Bardina, P. G. Huang, and T. J. Coakley, "Turbulence modeling validation, testing, and development," 1997.

[37]   J. R. Edwards and S. Chandra, "Comparison of eddy viscosity-transport turbulence models for three-dimensional, shock-separated flowfields," *AIAA J.*, vol. 34, no. 4, pp. 756–763, 1996.

[38]   T. D. Economon, F. Palacios, S. R. Copeland, T. W. Lukaczyk, and J. J. Alonso, "SU2: An open-source suite for multiphysics simulation and design," *Aiaa J.*, vol. 54, no. 3, pp. 828–846, 2015.

[39]   A. C. Duffy, "An introduction to gradient computation by the discrete adjoint method," *tech. rep.*, 2009.

[40] S. Nadarajah and A. Jameson, "A comparison of the continuous and discrete adjoint approach to automatic aerodynamic optimization," in *38th Aerospace Sciences Meeting and Exhibit*, 2000, p. 667.

[41] C. A. Mader, J. R. RA Martins, J. J. Alonso, and E. Van Der Weide, "ADjoint: An approach for the rapid development of discrete adjoint solvers," *AIAA J.*, vol. 46, no. 4, pp. 863–873, 2008.

[42] N. R. Gauger, A. Walther, C. Moldenhauer, and M. Widhalm, "Automatic differentiation of an entire design chain for aerodynamic shape optimization," in *New Results in Numerical and Experimental Fluid Mechanics VI*, Springer, 2007, pp. 454–461.

[43] A. C. Idris, M. R. Saad, H. Zare-Behtash, and K. Kontis, "Luminescent measurement systems for the investigation of a scramjet inlet-isolator," *Sensors (Switzerland)*, 2014.

[44] J. Häberle, "Untersuchungen zum externen und internen Strömungsfeld eines Scramjet Triebwerkseinlaufs bei unterschiedlichen Betriebspunkten," 2009.